CHEMICAL REVIEWS

pubs.acs.org/CR

Review

Physical and Chemical Factors Influencing the Printability of Hydrogel-based Extrusion Bioinks

Sang Cheon Lee, Gregory Gillispie, Peter Prim, and Sang Jin Lee*

Cite This: *Chem. Rev.* 2020, 120, 10834–10886

Read Online

ACCESS | Metrics & More | Article Recommendations

ABSTRACT: Bioprinting researchers agree that "printability" is a key characteristic for bioink development, but neither the meaning of the term nor the best way to experimentally measure it has been established. Furthermore, little is known with respect to the underlying mechanisms which determine a bioink's printability. A thorough understanding of these mechanisms is key to the intentional design of new bioinks. For the purposes of this review, the domain of printability is defined as the bioink requirements which are unique to bioprinting and occur during the printing process. Within this domain, the different aspects of printability and the factors which influence them are reviewed. The extrudability, filament classification, shape fidelity, and printing accuracy of bioinks are examined in detail with respect to their rheological properties, chemical structure, and printing parameters. These relationships are discussed and areas where further research is needed, are identified. This review serves to aid the bioink development process, which will continue to play a major role in the successes and failures of bioprinting, tissue engineering, and regenerative medicine going forward.

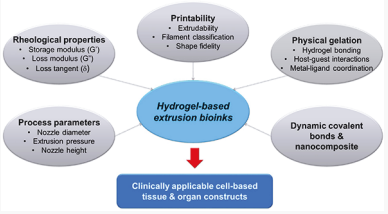

CONTENTS

Special Issue: 3D Printing for Biomaterials

Received: January 9, 2020
Published: August 20, 2020

Downloaded via WAKE FOREST UNIV on October 20, 2020 at 17:40:23 (UTC).
See https://pubs.acs.org/sharingguidelines for options on how to legitimately share published articles.

ACS Publications

© 2020 American Chemical Society

https://dx.doi.org/10.1021/acs.chemrev.0c00015
Chem. Rev. 2020, 120, 10834–10886

1. INTRODUCTION

The ability to bioengineer the various tissues or organs of the human body is a highly sought-after goal within modern research and medicine.[1,2] Tissue engineering strategies utilize cells, signaling molecules, and biomaterials to generate a final, tissue-like product.[3−5] While considerable success and improvements over time have been shown utilizing these strategies, the demand for personalized, large-scale, implantable tissue constructs continuously increased. A key piece to this future is the manufacturing processes that will be utilized. The manufacturing process determines the materials available for use, the architectures which can be created, and the time and cost which goes into the final product.

Additive manufacturing (also known as 3D printing) is causing a dramatic shift in the way society's products are made. It has also garnered significant interest within tissue engineering strategies. Anatomical structures are often abnormal, complex, and highly variable between patients and disease progressions, advantaging the flexibility of additive manufacturing relative to more traditional techniques such as machining and molding.[6] There are many different types of additive manufacturing that have been adapted by the tissue engineering field for use with biomaterials and cells, referred to as "bioprinting." The most common of these are extrusion-based bioprinting.[6−9] Extrusion-based bioprinting can easily incorporate multiple material types, a strategy which is imperative if any regional differences in biomaterials, cell types, or signaling molecules are desired.[10−12]

To ensure successful extrusion-based bioprinting, first and foremost are the materials which are a formulation of cells suitable for processing by an automated biofabrication technology that may also contain biologically active components and biomaterials.[13] These materials, known as bioinks, have a number of difficult requirements they must fulfill.[14,15] First, they must be biocompatible and nontoxic to cells and not promote host immune responses if implanted. Cells must be suspended directly in the material which requires both a thin enough material to mix the cells homogeneously and a thick enough material to maintain that distribution and prevent settling of the cells. Cell encapsulation also necessitates bioinks to be primarily composed of water, and for this reason, hydrogels are used.[16] Bioinks must provide bioactivity/cell attachment sites to allow for cell survival, attachment, and proliferation. They must have appropriate mechanical properties, preferably matching that of the tissue application both in terms of driving cell behavior and to withstand mechanical forces during handling and implantation.[17] Appropriate swelling and degradation characteristics are also necessary. Nutrients such as glucose and oxygen must be able to diffuse through the material to allow for cell survival in the deepest portions of the construct.[18] Lastly, bioinks should also serve to direct cellular behavior through the naturally derived polymers, proteins, and binding sites that are found in the ECM of the target tissue.[19,20] These requirements are common to most tissue engineering applications. For the bioprinting process, bioinks should fulfill the three basic requirements: relatively higher viscosity to maintain cell suspension homogeneously and to provide initial structural integrity, strong shear-thinning behavior to minimize shear stress-driven cell damage during the printing process, and rapid cross-linking process after printing.[12,21,22] In this review, we focus on physical and chemical factors impacting the printability of hydrogel-based bioinks specific to the 3D bioprinting process. In particular, we outline the underlying mechanisms which can affect different aspects of printability and present novel hydrogels with dynamic cross-linked networks (physical interactions and dynamic covalent bonds), which can be utilized for cell-based microextrusion bioprinting.

2. PRINTABILITY

There are many requirements of bioinks which are specific to the bioprinting process. These requirements capture the different aspects of bioinks "printability." In the broadest sense, printability refers simply to the ability to be printed. For the purposes of this review, the following definition will be considered:

"The ability of a material, when subjected to a certain set of *printing conditions*, to be printed in a way which results in *printing outcomes* which are desirable for a given application."

The first aspect of printability a bioink must overcome is extrusion from a micrometer-scale nozzle tip. This ability is sometimes referred to as a bioink's "extrudability." If too much force is used to extrude the material, cells will be permanently damaged via shear stress. Additionally, print times will be longer as higher flow rates cannot be achieved as easily.[23] As a result, if a bioink requires too high of an extrusion force, it cannot be used. After extrusion, a bioink must also be deposited in a predictable manner. Researchers have used a filament classification system to describe the different types of filaments which bioinks can form. Bioinks that form droplets at their tips will spread dramatically and stick to themselves. Continuous filaments are desired and these filaments can either be uniform (smooth) or nonuniform (bumpy, curvy). Smooth filament deposition is easily controlled by the bioprinter, but nonuniform filaments may deviate from the printing path and have variable cross sections across their length.[24] Following bioink deposition, the desired shape must be maintained as multiple layers are deposited on top of it. This "shape fidelity" of bioinks limits the ultimate size and shapes a bioink is able to structurally accomplish.[25,26] Lastly, different printing conditions (nozzle size, print speed, etc.) may be required depending on the application, further constraining the system as a whole. The similarity of a printed construct to the desired dimensions, as influenced by the printing conditions, can be referred to as "print accuracy." The term printability has been used to describe each of these requirements individually.[22,27−29] However, a bioink is not able to be bioprinted if it fails in any of these areas. Therefore, this review will consider each of these factors as singular aspects of printability.

2.1. Consideration on Bioink Development

With all the constraints and requirements placed upon bioinks, it should come as no surprise that the available bioinks remain a major limitation of bioprinting. Researchers would benefit tremendously from both improvements upon current bioinks and an expanded bioink palette.[5] A number of hydrogels and hydrogel combinations have been proposed in the literature; however, each has significant room for improvement in at least one area and sometimes multiple areas.[11] Contributing to this difficulty, many of the requirements placed on a bioink are in direct opposition. In many cases, bioinks which hold their shape particularly well upon deposition, also require the most pressure

https://dx.doi.org/10.1021/acs.chemrev.0c00015
Chem. Rev. 2020, 120, 10834−10886

Table 1. Representative Printability Measurements[a]

type	measurement	limitation/ condition	ref
	Extrudability		
binary classification	bioinks "unprintable" if flow could not be achieved at a maximum acceptable pressure	nozzle detachment	31
	bioinks "unextrudable" if flow could not be achieved at a maximum acceptable pressure	380 kPa	32
	bioinks "unprintable" if a flow rate of 0.3 mL/h could not be achieved by their system	unspecified	33
pressure under given conditions	pressure generated by plunger displacement at a constant speed	0.2 mm/s plunger speed	34
	pressure required to achieve a given amount of material deposition per construct	100 mg construct	21
	pressure required to achieve a minimum acceptable flow rate (lower bound) and pressure required to achieve a maximum acceptable flow rate (upper bound)	varied with nozzle size	35
	minimum pressure required to achieve consistent flow	unspecified	36
theoretical shear stress	proportion of nozzle diameter to extrusion pressure	n/a	37
	Filament Classification		
submerged	swelling, equivalent diameter, stretched, rough surface, overdeposited, compressed, discontinuous		38
filament drop test	droplet, filament		39
	droplet, smooth filament, overgelled filament		40
qualitative deposition	straight, curvy		41
	regular, irregular		32,33
quantitative deposition	uniformity ratio (filament perimeter normalized by length)		21
	Pr (pore perimeter normalized by pore area)		40
	standard deviation of filament heights and widths		42
	Shape Fidelity		
qualitative	cross hatch, anatomical shapes		38,41,43−63
filament spreading (single layer)	filament width		31,33,34,36,42,46,61,64−70
	filament height		33,42,61,69
	spreading ratio (filament width divided by nozzle diameter)		67
	aspect ratio (filament height divided by width)		71
	Pr (pore perimeter normalized by pore area)		40
height maintenance	critical height (maximum achievable height)		71
	height of cylindrical structure		72
	height of 5-layer tubular structure		21
filament collapse	angle of deflection of unsupported filament		73
	pore area below an unsupported filament		41
	Printing Accuracy		
filament dimensions	observation of broken filaments		31,45,56,65,66
	filament width		31−33,36,37,41,42,46,61,62,64,69,74,75
	filament height		33,42,61,69
	micro-CT		76,77
pore dimensions	pore area		36,41,62,70,78−83
filament merging	minimum distance required between filaments without merging		84
	overlap distance of a filament printed at an acute angle		62

https://dx.doi.org/10.1021/acs.chemrev.0c00015
Chem. Rev. 2020, 120, 10834−10886

Table 1. continued

type	measurement	limitation/ condition	ref
	Printing Accuracy		
	length of fused segment between adjacent filaments with increasing distance between filaments		73
	Others		
construct size	weight of construct		21
cell mixing	whether cells could be mixed with pipet		47
homogeneity	variability of extrusion force over time		34,58

[a]Reproduced with permission from ref 30. Copyright 2020 IOP Publishing.

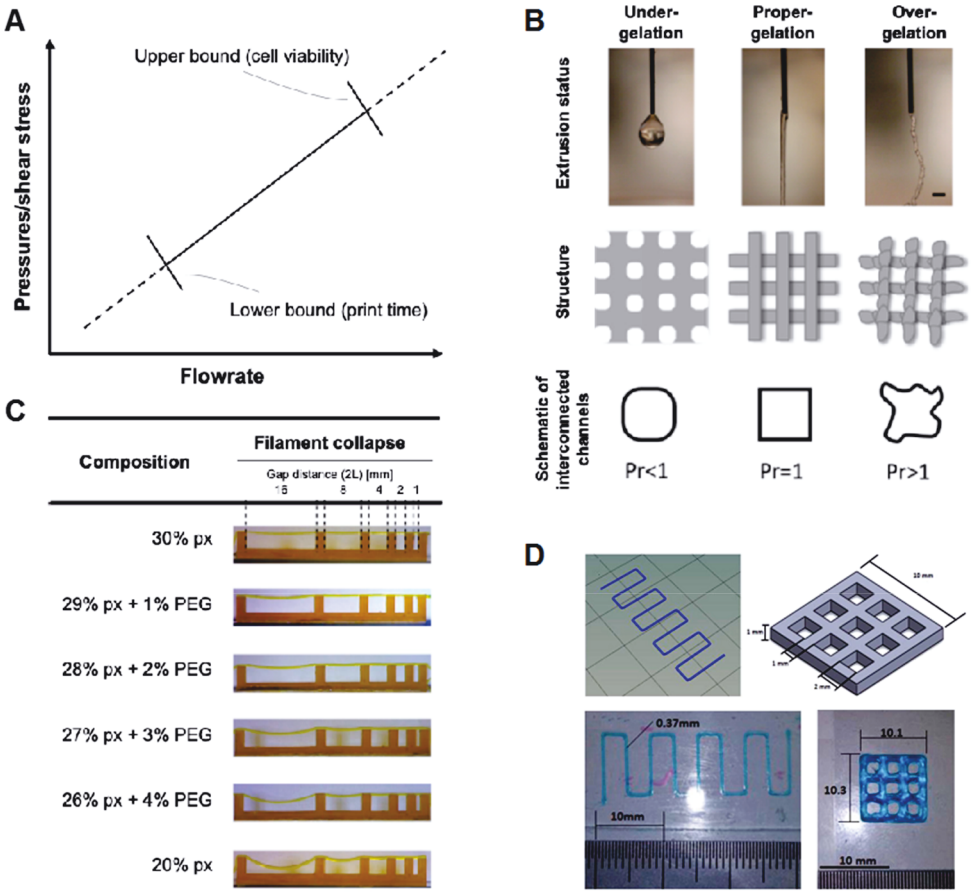

Figure 1. Different aspects of printability. (A) Extrudability can be defined at any point along with the pressure−flow rate relationship. Notably, a minimum flow rate is required to achieve reasonable print times and maximum extrusion force is limited to achieve reasonable cell viability after extrusion. (B) Filament classification has been used to describe the types of filaments which a bioink can form. This example measure from Ouyang et al. shows how the phenomenon can both be observed qualitatively and measured quantitatively. Reproduced with permission from ref 40. Copyright 2017 IOP Publishing Ltd. (C) Shape fidelity refers to the ability of a bioink to maintain its structure upon deposition. The example here from Ribeiro et al. tests a bioink's ability to form lateral pores. Reproduced with permission from ref 73. Copyright 2017 IOP Publishing Ltd. (D) Printing accuracy refers to the similarity of the printed structure to the original design as influenced by the printing conditions. This example from Giuseppe et al. uses zigzag and cross-hatch structures to compare dimensions. Reproduced with permission from ref 36. Copyright 2017 Elsevier Ltd.

to extrude.[5] This trade-off can be partially circumvented by various strategies including rapid postprinting cross-linking or gelation, the use of support baths, and bioinks which demonstrate particularly high degrees of shear-thinning. Additionally, while great strides are frequently made on the bioactivity and tissue-specific potential of bioinks, these bioinks typically are not well suited for bioprinting and vice versa. For example, Pluronic F127 offers excellent printability for extrusion bioprinting, but it is limited by its biological properties. Meanwhile, decellularized extracellular matrix (dECM) has been converted for use as a bioink due to its high, tissue-specific biological activity but forms a very weak gel which cannot hold its shape on its own when bioprinted which must be compensated for with complementary strategies.[25]

Bioink development is a growing field with the main objective of overcoming these various limitations. With respect to printability, bioink development itself is limited by its understanding of the underlying mechanisms which impact printability.[14] The factors which influence printability are numerous, complex, and interrelated.[16] Many relationships between printing conditions, material properties, and printability have been identified. However, many of these findings

https://dx.doi.org/10.1021/acs.chemrev.0c00015
Chem. Rev. 2020, 120, 10834−10886

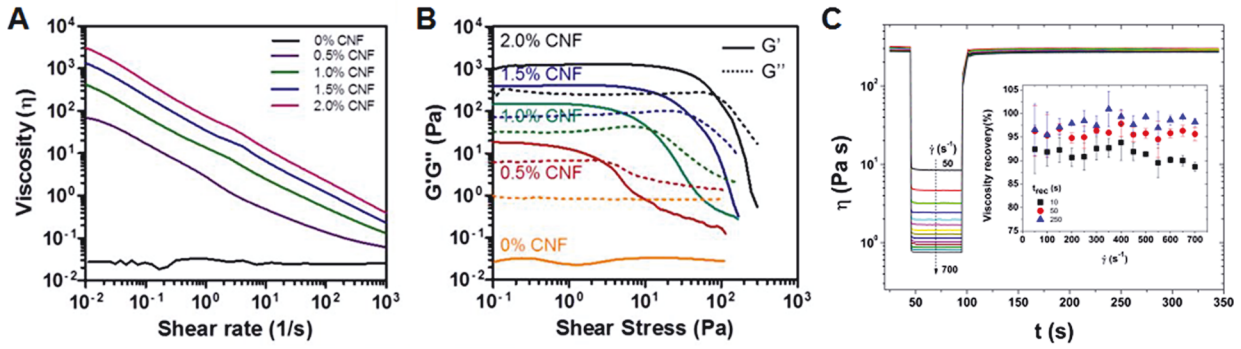

Figure 2. Common rheological measures associated with bioink printability. (A) Shear-thinning behavior of bioinks (log scale) with viscosity decreasing as shear rate increases. Reproduced with permission from ref 100. Copyright 2017 BioResources. (B) Viscoelastic and yielding behavior of bioinks. G' and G'' can be averaged from the linear viscoelastic region, while yield stress can be defined at the crossover point between G' and G''. Reproduced with permission from ref 100. Copyright 2017 BioResources. (C) Recovery behavior of a bioink using different shear rates to model the extrusion phase. Reproduced with permission from ref 103. Copyright 2018 Springer-Verlag London Ltd.

have been ambiguous or even conflicting and many more relationships remain unstudied. During the bioink development process, this knowledge is used to design, optimize, and improve a bioink.[17] Where it lacks, researchers must work using trial and error and move forward using less than ideal outcomes. The purpose of this review will be to examine these various relationships in an attempt to promote a better understanding and more holistic view of printability and the factors which influence it, in turn improving the bioink development process and therefore the bioinks available for use in bioprinting.

2.2. Measures of Printability

A clear understanding of the measures used to quantify printability is required in order to investigate the factors which influence printability. This topic is covered briefly in this section, but we refer the reader to a recent review by Gillispie et al.[30] for a more in-depth discussion. Not all requirements placed upon a bioink, those nonspecific to the printing process, should be considered within the realm of printability. With this in mind, the different measures of extrudability, filament type, shape fidelity, and printing accuracy are considered. Table 1 lists the representative measurements for printability.

Extrudability refers simply to how easily a bioink can be extruded through a small diameter nozzle, effecting total processing time and cell viability (Figure 1A). Cell viability during the bioprinting process has been linked to the pressure experienced by the cells in the syringe, the shear stresses experienced by the cells in the nozzle, and the amount of time cells spend in the syringe.[23,31,40,41,85−88] Because of this, researchers sometimes indirectly quantify the extrudability of their system by live/dead assay immediately following the bioprinting process.[23,34,69,85,87−90] Others have used extrusion pressure as the measure of extrudability. This can be either the pressure required to achieve a specified flow rate,[21,34,36,37,91] whether or not a given pressure was able to achieve flow,[31,33,71,92] or the minimum pressure which will cause flow[91,93] in their system. More sophisticated measures of a bioink's extrudability involve rheological measures such as the shear rate−viscosity relationship and power law constants and will be covered in a later section.

Filament type can easily be determined qualitatively. Several researchers conduct this test by extruding the bioink into the air rather than on a substrate and classify the shape of the extruded material as either droplet or filament (Figure 1B).[35,39−41] Bioinks that form filaments can be further classified by whether that filament is smooth or uniform.[40] Nonuniform filaments are can be more easily identified after deposition as some other researchers have observed.[33,41,92] However, the most robust measures of filament type are quantitative. After deposition, various dimensions can be made from the filaments, including the perimeter of square pores relative to perfect squares,[40] the perimeter of single filaments relative to a straight line,[21] and the variability of filament widths.[42]

The shape fidelity of a bioink is most frequently measured as the width and/or height of a single filament (Figure 1C). While easily to evaluate, this measure is highly prone to influence by the quantity of material deposited and interactions with the surface substrate. Additionally, it does not capture the full multilayer, spatial behavior required of bioinks. Among measures which do, the *Pr* value developed by Ouyang et al. is an attractive measure. Although it only evaluates two printed layers, it also has the benefit of being able to detect nonuniform filaments and controlling for material deposition by normalizing the perimeter to the area of the pore.[40] Gao et al. quantified shape fidelity as the height of a five-layer tubular structure. Bioinks with poor shape fidelity sagged under the weight of multiple layers, resulting in a decreased height measurement[21] Lastly, Ribeiro et al. measured the angle of the collapse of an unsupported filament printed between pillars of varying distances apart. Bioinks with poor shape fidelity have larger deflection angles as they cannot span the gaps as well.[73]

Printing accuracy has been measured in a variety of ways. Some of these measures are very similar to those for shape fidelity (Figure 1D). The key distinction is that print accuracy measurements compare a common bioink under different printing conditions, whereas shape fidelity measures compare different bioinks under common printing conditions. Most commonly, filament height, width, and pore size are used to assess printing accuracy. These are simple and important measures that can help ensure similarity between the designed structure and final structure, but they also test the accuracy of the printing system in the least strenuous fashion. Microcomputed tomography (μCT) measurements have been used to compare entire constructs to the design computer-aided design (CAD). This provides a much more robust test but is difficult to conduct and requires expensive imaging equipment and software.[76,77] Weight/volume of the final construct may also be used to confirm the desired amount of material deposition.[21] Several researchers have also identified unintentional filament merging

https://dx.doi.org/10.1021/acs.chemrev.0c00015
Chem. Rev. 2020, 120, 10834−10886

as an aspect of print accuracy. A particularly robust measure of this phenomenon involves printing a zigzag pattern with the distance between lines increasing. The outcome measure is the "fused segment length" between two parallel filaments.[73] Ultimately, more measures of printing accuracy are needed to capture additional phenomena such as filament discontinuity, turn accuracy, errors in flow initiation and stoppage, and others.

3. RELATIONSHIPS BETWEEN PRINTING OUTCOMES AND RHEOLOGICAL PROPERTIES

Rheology is the branch of physics that studies the flow of matter. It has proven to be extremely useful for bioink development and there are several rheological tests that are applicable to bioprinting. Most hydrogels demonstrate non-Newtonian behavior.[94] In a Newtonian fluid, the shear rate−shear-strain relationship is linear with viscosity remaining constant across strain rates. Hydrogels, on the other hand, are typically shear-thinning, meaning their viscosity decreases as shear rate increases.[95,96] The result is beneficial for the purposes of flow. As shear rate increases, the apparent viscosity of the material decreases, allowing flow to occur with lower pressure differentials and lower shear stresses on the material, and importantly cells, than would have occurred otherwise. This property is often measured via frequency sweeps, where the material is tested at a constant strain across a range of frequencies or shear rates (Figure 2A).[95,96] Also important is the thixotropy of a material. Once a strain rate is applied, thixotropic materials will show a decrease in apparent viscosity over time. This change in viscosity in turn impacts the bioink's flow with respect to time. Thixotropy is sometimes confused with shear-thinning as both properties result in decreased viscosity, but shear-thinning occurs with an increase in strain rate while thixotropy occurs over time at a given strain rate.[94] Materials may also be shear-thickening (opposite of shear-thinning) and rheopectic (opposite of thixotropic), but these are highly undesirable for bioprinting.

Hydrogel materials also demonstrate viscoelastic properties, meaning their behavior is determined both by viscous and elastic components. The elastic component is measured by the storage modulus, denoted by G', and refers to energy which is stored in a material when deformation is applied. The viscous component is measured as the loss modulus, denoted G'', and refers to energy which is lost when deformation is applied to the material.[95,96] The loss tangent, or tan δ, is the ratio of loss modulus (G'') to storage modulus (G'). The tan δ represents the relative contribution of viscous and elastic components to the material, with materials with values lower than 1 having a higher elastic contribution and materials with values higher than 1 having a higher viscous contribution. Typically, these properties are measured within the linear viscoelastic region (LVR) via strain or stress sweeps.[95,96] Frequency is held constant, and either stress or strain is increased, with storage modulus, loss modulus, and tan δ averaged throughout the LVR, where they remain relatively constant (Figure 2B).

Yield stress has been used to describe the initiation of flow and can be defined in multiple ways. Most commonly, a strain or stress sweep is used to gradually increase the stress on the material. As the material begins to flow, the storage modulus will drop dramatically. If dramatic and immediate enough, the stress at this drop off can be defined as the yield stress.[97] For bioinks where this decrease is more gradual, the stress at which the storage modus intersects with the loss modulus (i.e., where the tan δ is greater than 1 and the viscous properties begin to dominate the material's behavior) is considered the yield stress (Figure 2B).[33,73,98−100] Others have looked at both static and dynamic yield stress, defining static yield stress as the minimum required to initiate flow and dynamic yield stress as the minimum required to maintain flow.[93] While most researchers stick to this concept during bioink development, the measurement and application of yield stress as a rheological measure is less straightforward than these measures may imply.[101,102]

Finally, rheology has been used to measure the ability of hydrogels to recover from extrusion. Recovery tests are conducted in three steps. Initially, a very low shear rate is applied to the material, modeling pre-extrusion conditions. This is followed by a high shear rate intended to model extrusion. Finally, the material is returned to the initial shear rate, modeling postextrusion conditions (Figure 2C). Recovery is typically defined as the end viscosity represented as a percentage of the initial viscosity. Recovery increases over time after the high shear rate is removed, so recovery must be expressed at a certain time (i.e., 10 s, 60 s) after the high shear rate has been removed. Compared to other measures, recovery tests model the bioprinting process most closely. However, there is also the least amount of standardization between methods. Recovery can be measured by time to recovery[99] or percentage recovered.[33,98,103] The recovered parameter can be viscosity[99,103] or G'.[33,98] This can be measured across single[98,99,103] or multiple[33] cycles, and the extrusion phase can be modeled via shear rate,[99,103] strain,[33] or stress.[98]

3.1. Extrudability

Among different aspects of printability, the relationships between rheological properties and extrudability are the most well understood. Direct measures of extrudability, such as experimentally derived pressure-flow rate curves, are rarely conducted except to validate a rheological model. As such, most researchers typically present rheological characterizations as a proxy for extrudability. The main rheological measure of extrudability is the viscosity, with higher viscosity resulting in lower extrudability. Because of the non-Newtonian behavior of bioinks, viscosity must be measured across a wide range of shear rates with the upper end preferably being in the range of that experienced by the bioink during extrusion. Many factors can influence a bioink's viscosity such as temperature, time, solvent, preparation methods, and many more. Hydrogel composition and concentration have been examined most frequently. The addition of material has been demonstrated to result in higher viscosity and therefore lower extrudability in many bioinks, including chitosan, gelatin, alginate, Pluronic F127, κ-carrageenan, laponite, poly(2-hydroxyethyl methacrylate) (PHEMA), methylcellulose, xanthan, and others.[33,35,54,63,87,89,97,104]

Plotting several bioinks on the same viscosity vs shear rate graph can be sufficient for comparison within a single experiment. However, for cross-study comparisons and further modeling, it is helpful to model this behavior using the power-law relationship. By rheologically testing a bioink over a range of shear rates ($\dot{\gamma}$) ,the resulting data can be fitted to a power-law equation,

$$\tau = K\dot{\gamma}^n$$

$$\tau = \eta\dot{\gamma}$$

$$\eta = K\dot{\gamma}^{n-1}$$

https://dx.doi.org/10.1021/acs.chemrev.0c00015
Chem. Rev. 2020, 120, 10834−10886

where τ is the shear stress and η is the viscosity as measured by the rheometer, K is the consistency index, and n is the flow index or power-law index. These two shear-thinning constants are very useful in modeling flow behaviors. K is related to the bioink's viscosity and is sometimes referred to as the "apparent" or "zero shear" viscosity.[86,105] The degree to which a bioink is shear thinning can be inferred by the value of n, with values closer to 0 demonstrating more shear-thinning and values closer to 1 demonstrating more Newtonian behavior. Both of these values can be useful in comparing the extrudability of bioinks.[35,86,87,89,91,105,106] For example, Nadgorny et al. developed a novel benzaldehyde-functionalized PHEMA with ethylenediamine (EDA) bioink and used these properties as proxies for extrudability to help optimize for the concentrations of PHEMA and EDA.[97]

Using these constants and the nozzle dimensions, the bioprinting system can be modeled in even further detail via the Hagen−Poiseuille equation. The pressure−flow rate relationship can be derived to predict the flow rate at a given pressure or pressure required to achieve a given flow rate.[86,89,91,103,107,108] Dávila et al. have applied this concept to the development of an alginate-laponite bioink with a highly desirable viscosity profile.[103] Additionally, the shear rate and shear stress profiles can be derived to determine the forces cells are experiencing along the radius of the nozzle.[35,69,89,103,106] While accurate for most purposes, these models incorrectly will predict flow to occur at very low pressures. In reality, minimum stress must first be overcome to initiate flow. By incorporating the yield stress as the determining factor for the initiation of flow, Herschel−Bulkley models can be used to model flow behavior.[93,105] For example, Smith et al. examined Pluronic bioinks with various additives to optimize for chemical and flow characteristics.[93] Furthermore, a no wall slip condition is commonly assumed when modeling bioink extrusion with these models. However, there is some evidence that neglecting wall slip will slightly underestimate the flow rate and more complex models that account for this boundary condition are more accurate.[86,105] This is all to say that the influence of rheological properties on extrudability is relatively well understood, at least in terms of the bioink's flow rate. Several researchers have additionally used the rheological properties of their bioink to predict its deposition based on the flow rate and print speed (i.e., speed ratio).[86,105,107]

The influence on cell damage is slightly less understood, although several factors have been identified. Using these models of extrusion, the shear stress experienced by the cells can be estimated, which has been directly related to their viability. Of particular note, shear stresses are highest near the wall of the nozzle, and viability is subsequently lowest in these regions.[23,85,87] Flow rate and nozzle length have been used to estimate the extrusion duration of cells in the nozzle, which was found to decrease the viability of cells.[87] Other factors that have been implicated include waiting time in the syringe[23] and extensional flow at the syringe to nozzle transition.[88] Others have found no difference in cell viability at different extrusion pressures or shear stresses.[69] Complicating the matter further, while the direction of these relationships seems likely to hold regardless, the cell types and hydrogel carriers used may influence the magnitude of these effects. Further research is needed into the different causes of cell damage during the bioprinting process, especially in relation to the rheological properties of the bioink cell carrier. Such studies would aid significantly in future bioink development.

3.2. Filament Classification

Unfortunately, very few rheological studies have been directly related to filament formation outcomes. Still, some trends can be observed when viewing the body of literature as a whole. Schuurman et al. showed that at 37 °C their gelatin methacrylate (GelMA)-only bioink formed droplets even at concentrations up to 20% w/v. The addition of 2.4% w/v hyaluronic acid (HA) resulted in smooth filaments and improved printing outcomes.[39] Paxton et al. classified the filaments of different bioinks. They looked at different concentrations of Pluronic F127, different concentrations of alginate, and different degrees of alginate cross-linking. No rheological characterizations were done on bioinks which formed droplets because they were deemed unprintable. However, both Pluronic and alginate transitioned from droplet to smooth filament formation with increasing concentration. Alginate was also able to undergo this transition by increasing its degree of cross-linking via $CaCl_2$ concentration.[35] Davila et al. added Laponite to their 1% alginate bioink and saw a transition from droplet to smooth filament between 4% and 5% Laponite, corresponding with increases in viscosity, G', and G''.[103] Habib et al. mixed 4% alginate with varying carboxymethylcellulose (CMC) concentrations and found a transition from droplet to smooth filament formation between 1% and 2% CMC.[41] Ouyang et al. showed the effect of concentration, temperature, and holding time on gelatin-alginate bioinks.[40] In their work, droplet formation at a given temperature was seen in bioinks which did not gel (defined as a crossover between G' and G'') at that temperature.

Ouyang et al. also found the formation of nonuniform filaments to occur with higher gelatin concentrations, lower temperatures, and longer holding times. As each of those factors increased gelation, the authors attributed the nonuniform filaments to "over-gelation."[40] Gao et al. related rheological measures to filament-type directly.[21] Using varying concentrations of gelatin and alginate, the researchers showed a transition from smooth to nonuniform filaments as the loss tangent decreased. The transition occurred approximately between a loss tangent of 0.25 and 0.45. However, this window was not found to be predictive when applied to other bioinks. Kiyotake et al. showed their pentanoate-functionalized hyaluronic acid hydrogel (PHA)-based bioinks to increase in viscosity and G', decrease in recovery percentage, and have higher yield stress with increasing concentration.[98] At the highest concentrations, the bioinks exhibited nonuniform filaments. They attributed this loss of uniformity to a dramatic increase in yield stress (over 1000 Pa) and poor recovery from a high shear rate (less than 85%). Conversely, Zhu et al. looked at polyion complex (PIC) hydrogels and found lower hydrogel concentrations to result in both decreased viscosity and nonuniform filaments.[92]

While it is inconclusive from the current studies how rheological properties govern the droplet to uniform filament transition, some notable deductions can be made. Transitions from droplet to smooth filament have been found by increasing hydrogel concentration, ionic cross-linking, and thermal gelation. In general, this transition represents a change in the factor which dominates the bioink behavior. At droplet formation, bioink behavior is dominated by surface tension and water molecule interactions. For filament formation, the polymer network begins to dominate behavior as hydrogel concentration and gelation increases. However, further increases in hydrogel concentration and/or gelation beyond smooth filament formation are typically required to accomplish good

https://dx.doi.org/10.1021/acs.chemrev.0c00015
Chem. Rev. 2020, 120, 10834−10886

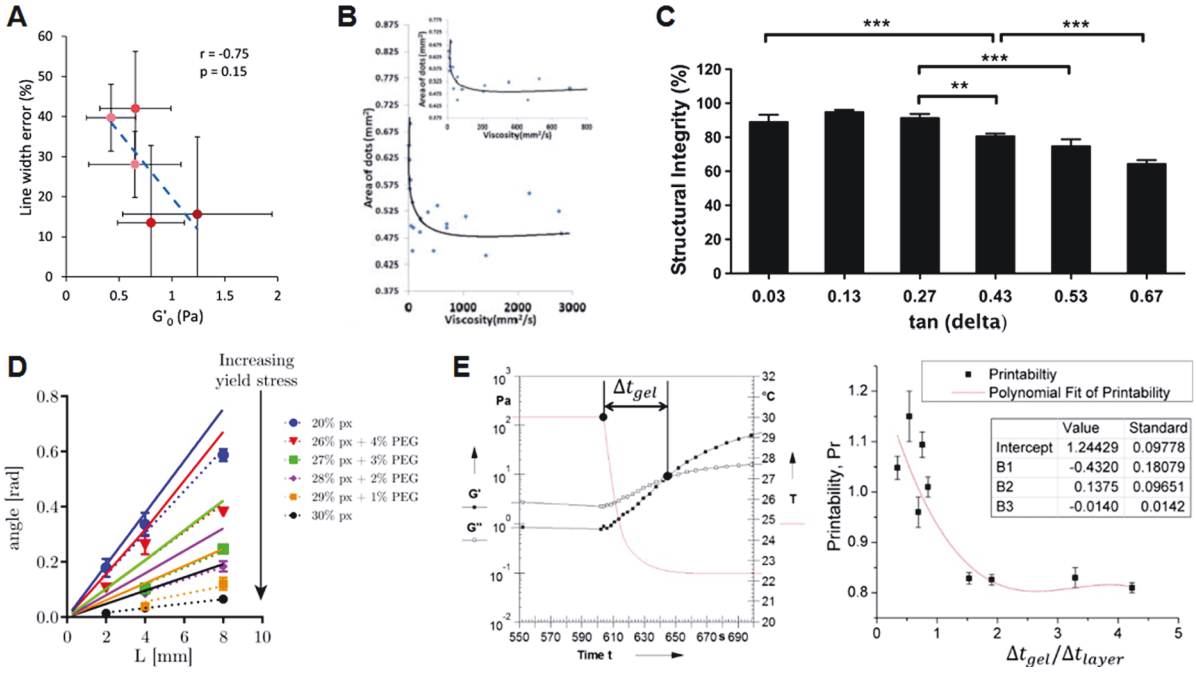

Figure 3. Identified relationships between rheology and shape fidelity. (A) Diamantides et al. related the storage modulus of their bioinks to filament width relative to nozzle size. Reproduced with permission from ref 70. Copyright 2017 IOP Publishing Ltd. (B) Jia et al. related the viscosity of their bioinks to the area covered by printed dots. Reproduced with permission from ref 110. Copyright 2014 Elsevier Ltd. (C) Gao et al. related the tan δ (loss tangent) of their bioinks to the height of a five-layer tubular structure. Reproduced with permission from ref 21. Copyright 2018 IOP Publishing Ltd. (D) Ribeiro et al. related the yield stress of their bioinks to its angle of deflection across unsupported gaps of varying distances. Reproduced with permission from ref 73. Copyright 2017 IOP Publishing Ltd. (E) Ouyang et al. related the gelation kinetics of their bioinks to the shape of horizontal pores, quantified using their *Pr* value. Reproduced with permission from ref 40. Copyright 2016 IOP Publishing Ltd.

shape fidelity.[21,40,41] All bioinks which form droplets will have poor printability, but not all bioinks which form smooth filaments will have good printability. Therefore, droplet formation is better viewed as a prescreening tool and bare minimum barrier used to quickly eliminate bioink candidates.

The underlying cause of the transition from smooth to nonuniform filaments is even less clear. The contradictory results between gelatin-based and PIC-based bioinks likely mean different mechanisms are at play in the cause of these phenomena between the two hydrogels. Furthermore, some hydrogels (such as Pluronic) do not seem to exhibit this behavior regardless of hydrogel concentration or degree of cross-linking. As a result, further research into this phenomenon is needed before any major conclusions can be drawn.

3.3. Shape Fidelity

It is also difficult to determine which rheological measurements influence shape fidelity. Very few studies have attempted to directly define this relationship. However, many studies have looked at both the rheology and shape fidelity. Most commonly, this is done while optimizing for hydrogel concentration within a bioink.[33,34,41,54,71,89,90,97−100,103,109] Hydrogel concentration influences many rheological parameters simultaneously, which is a major obstacle in studying the rheology−shape fidelity relationship. The most frequently rheological measure examined is viscosity. As hydrogel concentration increases, so does the viscosity for most materials. In these studies, a subsequent increase in shape fidelity is also typically seen.[34,41,54,89,90,97−100,109]

However, viscosity encompasses only a single portion of bioink behavior, namely, its resistance to flow. The viscoelastic properties of a bioink have also been shown to play an important role. A bioink's complex modulus (G^*) also typically increases with concentration. This increase may be due to an increase in G', G'', or, most commonly, both.[71,97,99,100,103,109] Even as both G' and G'' increase, one may come to dominate the behavior as the relative contributions (quantified as the loss tangent) change.[21] G^*, G', and G'' have all been linked to shape fidelity indirectly through bioink concentration. As the measure of elasticity, G' has received the most attention among them.[71,97,99,100,103,109]

The yielding behavior of a bioink is also frequently studied alongside changes in shape fidelity. The concept here is that as bioink's yield strength increases, it can resist greater forces before plastically deforming. As hydrogel concentration increases, so does the amount of stress required to initiate flow. This increase has been linked to shape fidelity in several studies.[71,97−100] Rutz et al. additionally reported on the strain at the yield point, which decreased with increasing concentration and shape fidelity, and G' at the yield point, which increased with hydrogel concentration and shape fidelity.[71] Additionally, this relationship does not necessarily hold when adding a new hydrogel to the bioink, as Wilson et al. found the addition of laponite to their κ-carrageenan (κCA) bioink to dramatically decrease the yield stress while simultaneously improving its shape fidelity.[33]

Lastly, the recovery behavior of a bioink has also been linked indirectly to shape fidelity via hydrogel concentration. Wilson et al. attributed the improved fidelity of their laponite supplemented bioink (despite its decrease in yield stress and G') to its enhanced recovery behavior (93−99% recovery of initial G' vs 69% for the κCA only bioinks).[33] Also looking at laponite, Peak et al. found a decrease in recovery time corresponded to an improved shape fidelity for their PEG-based bioinks.[99]

https://dx.doi.org/10.1021/acs.chemrev.0c00015
Chem. Rev. 2020, 120, 10834−10886

Table 2. Influence of Various Printing Parameters on Printing Outcomes

process parameter	process parameter values	range of resulting printability measure	direction[a]	materials
	Line Width			
nozzle diameter	210 μm (27 G), 260 μm (25 G), 514 μm (21 G)[111]	220.72−3215.85 μm	↑	24.5% Pluronic F127
	30 G, 27 G, 25 G[37]	270−9170 μm	↑	7% alginate + 8% gelatin
	100 μm (32 G), 150 μm (30 G), 230 μm (27 G), 300 μm (25 G), 400 μm (2 3G)[36]	170−570 μm	↑	7% alginate + 8% gelatin
extrusion pressure	100, 200, 300 kPa[111]	220.72−3215.85 μm	↑	24.5% Pluronic F127
	100, 150, 200, 250 kPa[37]	270−9170 μm	↑	7% alginate + 8% gelatin
	4, 41, 55, 69, 83, 103 kPa (5, 6, 8, 10, 12, 15 psi)[41]	∼450−1750 μm	↑	4% alginate + CMC
	69, 83, 97, 110, 138 kPa (10, 12, 14, 16, 20 psi)[114]	∼480−1260 μm	↑	4% alginate + CMC + montmorillonite
	40, 60, 80 kPa[61]	∼450−4300 μm	↑	dECM (porcine skin)
feed rate	4−9 mm/s[112]	∼550−1130 μm	↓	2.5% alginate + 8% gelatin
	10, 20, 30 mm/s[111]	220.72−3215.85 μm	↓	24.5% Pluronic F127
	1, 2, 3, 4, 5, 6 mm/s[37]	270−9170 μm	↓	7% alginate + 8% gelatin
	4, 5, 6, 7, 8, 9, 10 mm/s[41]	∼450−1350 μm	↓	4% alginate + CMC
	0.8, 2.1, 3.3 mm/s[61]	∼450−4300 μm	↓	dECM (porcine skin)
nozzle height	0.1, 0.2, 0.3, 0.4, 0.5, 0.6, 0.7, 0.8, 0.9, 1.0, 1.1 mm[112]	∼960−1270 μm	↑	2.5% alginate + 8% gelatin
	0.4, 0.7, 0.9, 1.1, 1.3, 1.5 mm[41]	∼570−1270 μm	↑	4% alginate + CMC
	300, 400, 500 μm[42]	∼420−450 μm		4% CNF
	300, 400, 500 μm[42]	∼720 μm		Ink 6040
line pitch	1, 2, 3, 4, 5 mm[112]	∼680−860 μm	↓	2.5% alginate + 8% gelatin
	Line Height			
extrusion pressure	40, 60, 80 kPa[61]	∼250−2250 μm	↑	dECM (porcine skin)
feed rate	5, 10, 20 mm/s[42]	∼280−460 μm	↓	4% CNF
	Pore Size (1 − Filament Diffusion Rate)			
nozzle diameter	100 μm (32G), 150 μm (30G), 230 μm (27G), 300 μm (25G), 400 μm (23G)[36]	77−99%	↓	7% alginate + 8% gelatin
line pitch	1, 2, 3, 4, 5 mm[112]	∼80−96%	↑	2.5% alginate + 8% gelatin
	1, 2, 3, 4, 5, 6 mm[41]	0−90%	↑	4% alginate + CMC
	1, 2, 3, 4, 5, 6 mm[114]	0−95%	↑	4% alginate + CMC + montmorillonite
	2, 4, 6, 8, 10 mm[113]	0−93.75%	↑	collagen/PPy-*b*-PCL
	Filament Collapse			
line pitch	1, 2, 3, 4, 5, 6 mm[41]	0−100%	↑	4% alginate + CMC
	1, 2, 3, 4, 5, 6 mm[114]	0−100%	↑	4% alginate + CMC + montmorillonite
	2, 4, 8, 16 mm[73]	0.02−0.58 [rad]	↑	Poloxamer + PEG

[a]Direction of the relationship between printability and printing condition.

Conversely, Kiyotake et al. saw a decrease in recovery percentage with increasing shape fidelity for a pentanoate-functionalized HA-based bioink.[98]

Several studies have attempted directly relate rheological measures to shape fidelity. Diamantides et al. compared several rheological measures to the shape fidelity of their collagen-based bioinks, including G' pre and post UV cross-linking, cross-linking rate, and time required to cross-link. They found that, under their range of testing conditions, G' prior to cross-linking was the best predictor of shape fidelity (Figure 3A).[70] Jia et al. related the shape fidelity of alginate hydrogels to their viscosity. By varying the alginate concentration and oxidation percentage, they found that higher viscosities resulted in better shape fidelity (Figure 3B).[110] Smith et al. investigated four different additives at two concentrations each by incorporating them into their methacrylated Pluronic bioink. Shape fidelity was assessed by the filament diameter upon deposition relative to that of the nozzle diameter. The authors related this measure to their bioink's dynamic yield stress, with high yield stress correlating to high shape fidelity. However, the researchers did not control for flow rate, and it is unclear whether the changes in filament diameter were a result of decreased shape fidelity or simply different volumes of bioink being deposited.[93]

Results from Gao et al. directly relate loss tangent to shape fidelity by measuring the height of a five-layer tubular structure. The height of the structure was inversely related to the loss

https://dx.doi.org/10.1021/acs.chemrev.0c00015
Chem. Rev. 2020, 120, 10834−10886

tangent (G'/G'') and loss modulus (G'') of their gelatin-alginate bioinks (Figure 3C).[21] Ribeiro et al. developed a theoretical model for their measure of shape fidelity. They printed Pluronic-PEG bioinks across pillars of varying distances apart, leaving the bioink unsupported between pillars. The following equation was derived to predict the angle of deflection (θ) of the unsupported filament:

$$\theta = \sin^{-1}\left(\frac{\rho g L}{\sigma_{\text{yield}}}\right)$$

where p is the bioink density, g is the gravitational acceleration, L is half the length between pillars, and σ_{yield} is the yield stress of the bioink as measured on a rheometer. Their results showed a strong negative correlation between yield stress and deflection angle. The model slightly overestimated the angle of deflection but showed similar trends as the experimental data across different bioinks and gap distances (Figure 3D).[73] Ouyang et al. showed, using thermosensitive alginate-gelatin bioinks, that gelation time impacted printability. Bioinks which did not gel as quickly did not maintain their shape as well, especially if the gelation time was longer than the time it took to print each layer (Figure 3E).[40]

To summarize, bioink shape fidelity has been positively correlated to hydrogel concentration, thermal cross-linking, viscosity, G', yield stress, and recovery abilities and negatively correlated with G'' and loss tangent. A major limitation in studying this relationship is the difficulty of isolating individual parameters. It seems likely at this point in time that each of these factors may play a role in bioink shape fidelity. More complex models of bioink behavior, such as via finite element analysis,[42] may be needed to predict printing outcomes.

4. RELATIONSHIPS BETWEEN PRINTING OUTCOMES AND PROCESS PARAMETERS

Some measures of printability are influenced by the printing process. These measures of printability include: line width, corner resolution, corner regularity, pore size, and filament horizontal holding.[35,70,111] Measures of printability are controlled by varying sets of process parameters. These measures of printability have been assessed visually, either qualitatively or quantitatively. Qualitative assessments have been performed by eye and judgment.[41,112] Quantitative assessments involve a photograph from either a camera[36,41,113,114] or microscope[41,61,114] followed by image analysis with software such as ImageJ.[36,37,41,42,61,114]

4.1. Consideration on Process Parameters

The most examined measure of printability is the line width. Line width increases with increasing nozzle diameter, extrusion pressure, and nozzle height. Line width also increases with decreasing feedrate and line pitch. These relationships have been demonstrated over limited independent variable ranges and result in limited dependent variable ranges (Table 2). Some independent variable ranges overlap. Differences can be attributed to differences in materials (as different hydrogels were tested in each study), which vary in rheological and material properties, and by differences in other process parameters when isolating correlation among parameters of interest.

Line height can be controlled by extrusion pressure, feedrate, nozzle height, or recovery time. The only report of an extrusion pressure influence on line height employed an overdeposition methodology, whereby the flow rate resulted in an equal or excessive filament height as compared to the layer height. These researchers reported line heights of 1−9 times the layer height.[61] Conversely, most printing methodologies constrain the flow rate such that the resulting filament deposition is equal to the layer height. Extrusion pressure, flow rate, and feed rate are freely adjusted within a range that results in filaments equal to the layer height. If extrusion pressure, flow rate, and feed rate yield ideal within-layer printability, but the between-layer printability is unacceptable, nozzle height is then adjusted to match. At no time can the resulting filament height be continuously less than the layer height, as this will result in a cumulative increase in nozzle height and print failure. It may be advantageous for the resulting deposition height to be slightly greater than the nozzle position so as to create interference and better adhesion between layers.

When hydrogel filaments of different orientations overlap (often reported at 90° angles), filaments merge at the point of contact, and surface tension can draw out sharp contact angles.[41,112] The degree of filament diffusion has been correlated with line pitch, in which filament diffusion increases with decreasing pitch. Large line pitch minimizes filament diffusion, but there will always be some small amount which occurs. If pores are too small, filament diffusion can be so severe that the initial pore disappears. Similarly, Ribeiro et al. have developed a filament fusion test which shows how changes in the distance between filaments affect the fusion between filaments. As the line pitch of their cross-hatch design increased, the length of the fused section between filaments decreased.[73]

As a process parameter, line pitch is user-controlled and determined prior to printing. Therefore, the influence of line pitch on printability is necessary to understand. Line pitch has been shown to influence the filaments deposited on subsequent layers, with greater distances between printed filaments on the supporting layer resulting in higher filament collapse on the supporting layer.[41,73,114,115] For a given material, some increased line pitch results in 100% filament collapse, and all greater line pitches have complete collapse. For example, a line pitch of 2 mm was achieved with alginate before complete collapse, and the addition of CMC achieved 3 mm at a low concentration and at least 6 mm at higher concentrations.[41] The addition of montmorillonite to alginate decreased the line pitch at which complete collapse occurred, from 3 mm down to 2 mm, which was likely due to the increased weight of the montmorillonite filament without an appreciable increase in yield strength.[114] The usage of the filament collapse test has suggested that varying degrees of filament sag are permissible, but so far, acceptable and unacceptable ranges have not been identified or discussed.

Corner resolution describes the sharpness of a corner. Current measures of corner resolution are qualitative, being described as being either sharp or curved/rounded. Nozzle height effects corner resolution: increasing nozzle height reduces corner resolution, shifting the deposition shape from sharp to curved.[41,112] Corner regularity has been used to describe the degree of overdeposition at a corner. As corner angle decreases below a right angle, extrudate increasing overlaps. For sharp corners of small angles measures, extrudate overlaps considerably and causes the corner to bulge. To prevent the buildup of material in sharp angle corners, the rate of material deposition and be decreased or feedrate can be increased.[112]

https://dx.doi.org/10.1021/acs.chemrev.0c00015
Chem. Rev. 2020, 120, 10834−10886

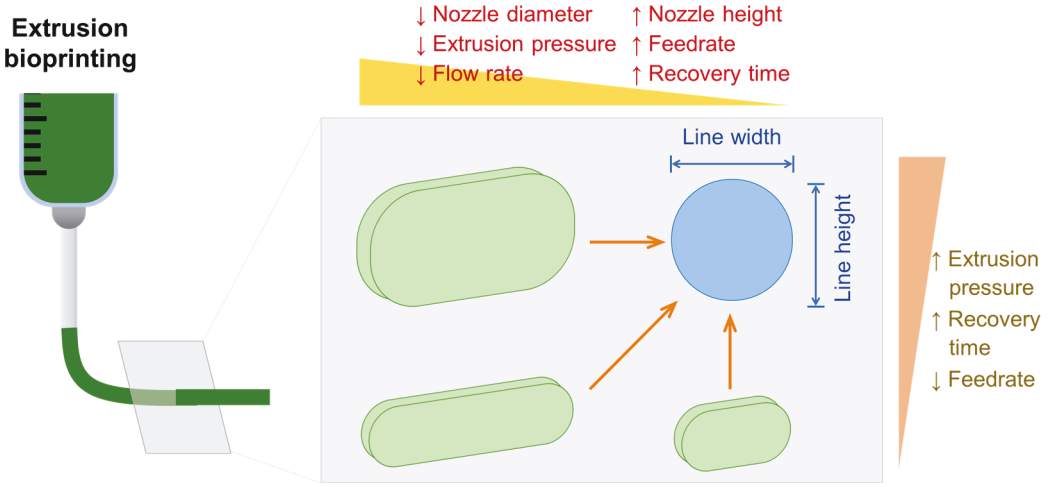

Figure 4. Relationships among printability measures and process parameters to control line width and line height (cross-sectional geometry).

4.2. Improving Printability by Process Parameters

The main researched printability measures effected by process parameters include line width and line height (Figure 4). This distinction is from quantitative-only assessments in the reporting literature; qualitative assessments were not included in Figure 4. However, we have summarized their findings qualitatively because factors such as differing materials account for significant differences in results. Regardless of the difference in material properties as they play out in different extrusion printing systems, the trends are universal.

Process parameters have a role in printability. In general, accuracy is improved by reducing line width and increasing line height. Most materials and printing conditions result in filaments that are too wide and that sag over their cross-sectional area (reducing line height). The combined effect is a reduction in pore area (between printed lines). Changes which reduce line width and increase line height will increase pore area, improving printability. Some of the influential process parameters affect more than one printability measure. Recovery time effects both line width and line height. Increasing recovery time decreases line width and increases line height. Fortunately, in the case of recovery time, a single change in this one parameter will improve printability in two different measures (line width and line height). Extrusion pressure and feed rate, however, cause divergences in line width and line height. Increasing feed rate (or decreasing extrusion pressure) decreases line width (an improvement) but decreases line height (a detriment). There is only one report of recovery time affecting filament height as a measure of printability, and this report only investigated alginate and graphene oxide doped alginate.[89]

While some research has identified the connection between flow rate and line width, none has identified a connection between flow rate and line height. Because flow rate is directly proportional to extrusion pressure, the relationship between flow rate and line height can be similar to the one between extrusion pressure and line height. A future study should examine this relationship and use several different materials to show the scope of applicability.

5. CHEMICAL STRATEGIES: PHYSICAL INTERACTIONS

Hydrogels are generally fabricated through cross-linked networks formed by physical interactions or chemical bonds.[116,117] Physically cross-linked hydrogels are characterized by the network being held together with weak noncovalent interactions, including hydrogen-bonding, hydrophobic interaction, ionic interaction, host−guest interaction, metal−ligand interaction, and $\pi-\pi$ stacking interaction.[118−120] These reversible interactions allow most physical hydrogels to exhibit good printability due to dynamic rheological properties, which are advantageous for microextrusion-based printing processes.[121] In this section, we focus on (i) hydrogen bonding, (ii) host−guest interactions, and (iii) metal−ligand coordination that have been mostly employed in the recent emerging shear-thinning and self-healing hydrogels due to their versatility and flexibility in chemistry, allowing diverse new design approaches. For a detailed discussion of other classes of physical interactions, such as ionic, hydrophobic, and $\pi-\pi$ interactions, we refer the reader to various excellent recent reviews describing design strategies for shear-thinning and/or self-healing physical hydrogel formation.[117,121−125]

5.1. Hydrogen Bonding

Hydrogen bonds are noncovalent dynamic interactions in which a hydrogen atom attached to electronegative atoms, such as oxygen, nitrogen, and fluorine, forms a partial intermolecular bonding interaction with other vicinal electronegative atoms.[126] Hydrogen bonding exhibited a relatively weak bond strength between 0.25 to 15 kcal/mol,[126] which is several times weaker than covalent bonds and ionic interactions. However, when low molecular weight compounds or polymers are designed to facilitate multiple hydrogen bonding, the overall association force between their structures is greatly improved,[127,128] which enables hydrogen bonds to serve as useful interactions to build up diverse supramolecular hydrogels. To date, various classes of moieties have been employed to develop dynamic hydrogels with shear-thinning or stimuli-responsive properties. Some examples of these moieties are an adenine/thymine base pair,[129] ureidopyrimidinone (UPy),[130,131] 6-aminocaproic acid,[132] and diaminotriazine,[133] and phenolic compounds,[134,135] including gallol or catechol groups. Among physical hydrogels formed by these moieties, we focus on recent reports on shear-thinning dynamic hydrogels constructed via hydrogen bonding interactions based on phenolic compounds and UPy self-complementary dimerization.

5.1.1. Phenolic Compound-Based Interaction. Shin et al. reported on rapid spontaneous gelation of gallol-conjugated hyaluronic acid (HA-Ga) in the presence of a gallol-rich cross-

https://dx.doi.org/10.1021/acs.chemrev.0c00015
Chem. Rev. 2020, 120, 10834−10886

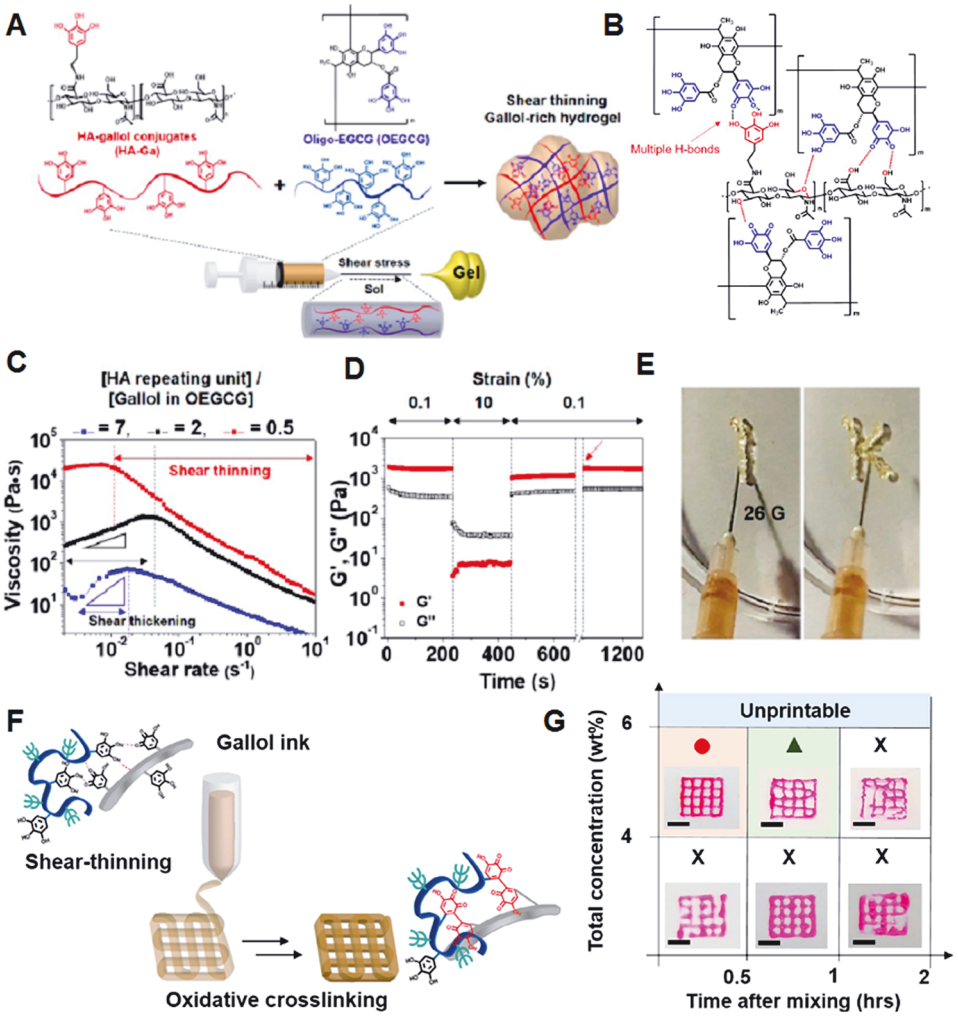

Figure 5. (A) Schematic illustration for preparing gallol-rich, shear-thinning hydrogels of HA-Ga/OEGCG. (B) The proposed multiple hydrogen bond formation (red dashed line) between the gallol-to-gallol moieties and gallol-to-HA backbone. (C) Changes in viscosity as a function of shear rates for HA-Ga/OEGCG hydrogels with the [HA unit]/[gallol in OEGCG] ratio of 7 (blue), 2 (black), or 0.5 (red). (D) The recovery measurement of G' displaying the hydrogel structure under alternating strain from 0.1% to 10% back down to 0.1%. (E) A photograph showing the injectability of the HA-Ga/OEGCG hydrogel (the ratio = 0.5) using a 26 G needle (inner diameter = 0.26 mm). Reproduced with permission from ref 136. Copyright 2017 American Chemical Society. (F) Schematic illustration of the 3D printing where the gallol ECM hydrogel ink transitions from a shear-thinning hydrogel during printing to one with mechanical stabilization via oxidation after the printing. (G) Printability of the gallol ECM ink with various concentrations (4, 6 wt %) and injectability as a function of the time after gel formation (0.5, 1, 2 h). Scale bars of 4 mm. Reproduced with permission from ref 138. Copyright 2019 Elsevier.

linker, oligo-epigallocatechin gallate (OEGCG) (Figure 5A).[136] The main driving force for hydrogel formation is multiple gallol-to-gallol and gallol-to-HA hydrogen bonding interactions (Figure 5B). Rheological studies showed that the storage modulus (G') and the loss modulus (G'') were dependent on the [D-glucuronic acid-D-*N*-acetylglucosamine]/[gallol in OEGCG] stoichiometric ratio. At a ratio of 2, the G' value was 341.6 ± 53.6 Pa at 1 Hz, whereas, at a ratio of 0.5, the hydrogels showed a G' value of 1390.5 ± 128.0 Pa. The gallol-involved cross-linking was reversible, and thus this hydrogel exhibited shear-thinning behavior (Figure 5C). Under alternating strain, G' and G'' were recovered to 92% and 80% of their initial values (Figure 5D), and G' almost recovered to its initial value after 540 s of the fraction (red arrow). This hydrogel was able to be injected with a 26 G needle (Figure 5E).

Gallol-containing compounds, such as tannic acid, have been widely explored for use in supramolecular hydrogels through a combination of hydrogen bonding and metal-coordination interactions.[134,137] In this case, the addition of Fe^{3+} ions to the tannic acid-bound polymer chains was essential to form the cross-linked network via chelation. In contrast, for HA-Ga/OEGCG hydrogels, the addition of metal ions was not needed because the polymer-bound gallol moieties provided multiple hydrogen bonds that were strong enough to form the gel. Recently, Shin and Burdick et al. designed a gallol-derived extracellular matrix (ECM)-mimetic adhesive bioink exhibiting temporal shear-thinning properties. This bioink formed a gel by noncovalent hydrogen bonding interactions between polymer-bound gallol moieties and peptide linkages in the protein backbones.[138] The main components for hydrogel formation were gallol-modified HA (HA-Ga) and gelatin-gallol (GEL-Ga). They further studied the stabilization of the hydrogel structure by examining the covalent cross-linking process between gallol aromatic rings through a spontaneous auto-oxidation process (Figure 5F). Gallol groups are known to undergo auto-oxidation to form hydroquinone accompanied by covalent cross-linking

https://dx.doi.org/10.1021/acs.chemrev.0c00015
Chem. Rev. 2020, 120, 10834−10886

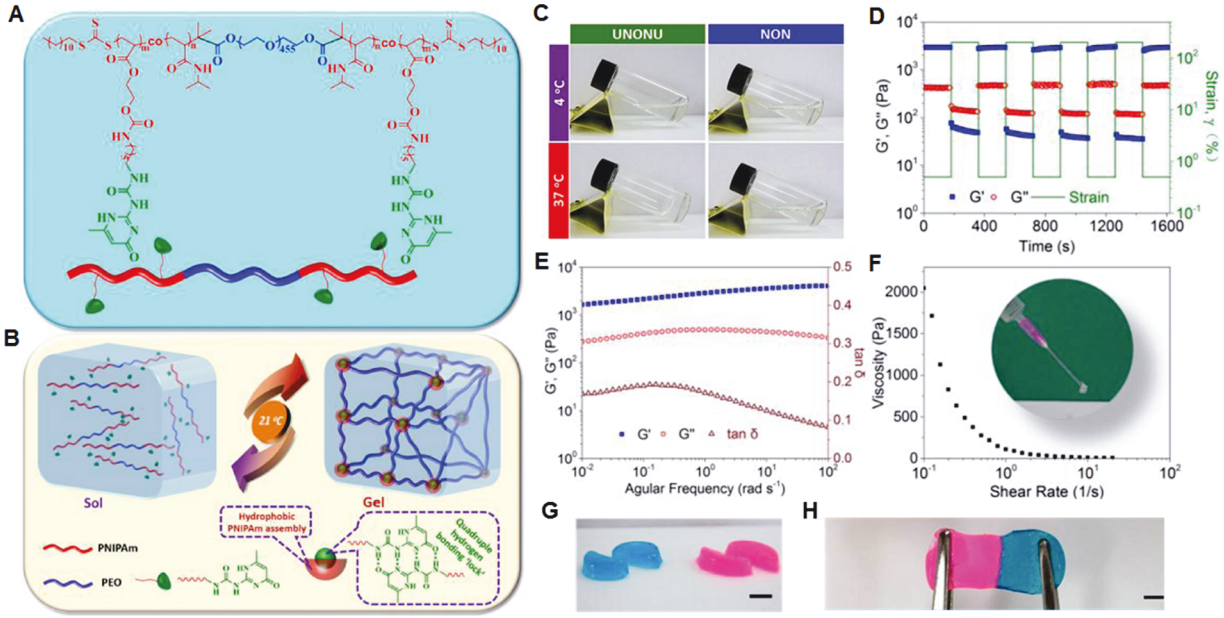

Figure 6. (A) Chemical structure of the ABA triblock copolymer. (B) Schematics of the reversible sol−gel transition of the prepared hydrogel under temperature switch. (C) Gelation test of UNONU and NON polymer solutions under cold (4 °C) and warm (37 °C) conditions via simple tilting. (D) Dynamic strain amplitude cyclic test (γ = 0.5% and 200%) of the hydrogel at 37 °C showing rapid self-healing behavior. (E) Frequency-dependent (at a strain of 1%) oscillatory shear rheology of the hydrogel. (F) Viscosity measurement of the hydrogel (inset: injection test of the hydrogel at room temperature). (G) Hydrogels were cut into equal halves by a razor blade. (H) The self-healed hydrogels can also withstand stretching, scale bars: 1 cm. Reproduced with permission from ref 141. Copyright 2017 American Chemical Society.

over several hours (~120 min).[139] The printability of this bioink, evaluated by the shape fidelity of the printed filaments, was dependent on the concentration of the gallol ECM hydrogel and time after mixing (Figure 5G). A weight ratio of 1:2 (HA-Ga:GEL-Ga), a concentration of 6 wt %, and a mixing time of 0.5 h resulted in stable filament formation.

A novel injectable hydrogel was prepared through self-assembly of an ABA triblock copolymer comprising catechol-functionalized oligomeric PEG methacrylate (A block) and poly([2-(methacryloyloxy)-ethyl] trimethylammonium iodide) (PMETA) (B block).[140] The aqueous solution of the block copolymer exhibited thermosensitive reversible sol−gel transition behavior. At 37 °C, the solution formed hydrogels with shear-thinning and self-healing characteristics, whereas the gel became a sol at 4 °C. The main driving force for hydrogel formation was the hydrogen bonding and aromatic interactions between catechol groups. This work demonstrates that the catechol moieties, similar to gallol moieties, can also act as cross-linkers to form dynamic physical networks.

5.1.2. Ureidopyrimidinone Self-complementary Dimerization. Self-complementary quadruple hydrogen bonding interactions can be used to develop dynamic supramolecular hydrogels. Using a reversible addition−fragmentation chain-transfer (RAFT) polymerization route, Zhang et al. synthesized a water-soluble ABA triblock copolymer (termed UNONU) consisting of a middle poly(ethylene oxide) block (A) and terminal poly(*N*-isopropylacrylamide) (PNIPAm) block incorporated with Upy moieties (Figure 6A).[141] The UPy moieties in the PNIPAM blocks can form self-complementary dimers via quadruple hydrogen bonding interactions[142,143] and have been widely employed to produce diverse supramolecular hydrogels.[130,131,144−146] The UNONU has the lower critical solution temperature (LCST) of 21 °C due to the thermosensitive UPy-conjugated PNIPAM block, which induced the formation of assembled micelles/clusters. UPy moieties in the PNIPAM core domains strongly hold the polymer chains, thereby forming hydrogel cross-linked 3D networks (Figure 6B). The UNONU copolymer showed a temperature-responsive sol−gel transition, whereas the copolymer (NON) without incorporated UPy did not form a gel even at 37 °C (Figure 6C). This observation clearly supports the key role of UPy self-complementary dimerization in hydrogel formation. UNONU copolymer hydrogels exhibit rapid self-healing properties after mechanical disruption (Figure 6D). Rheological studies show that G' is dominant across the whole frequency range (Figure 6E) and that the supramolecular hydrogel is soft but highly elastic ($\tan\delta < 0.2$). The viscosity of the hydrogel decreases with increasing shear rate, indicating that the hydrogel can be injected through the extrusion process (Figure 6F). When two individual hydrogel pieces are in contact, rapid healing is observed. Furthermore, the adhered interface withstands stretching (Figure 6G,H).

UPy moieties have also been introduced to gelatin-based hydrogel. Zhang et al. prepared UPy-conjugated gelatin-based (Upy-gelatin) hydrogels cross-linked by UPy self-complementary dimerization.[147] The hydrogels formed from a Upy-gelatin solution of 10 wt % at 25 °C showed a storage modulus of 1000 Pa, which was ascribed to the ordered arrangement of gelatin chains and the quadruple hydrogen bonding between UPy moieties. The hydrogels exhibited a shear-thinning behavior and an excellent self-healing property at 25 °C. They demonstrated that the gelling property and mechanical strength could be further improved by adding Fe^{3+} ions to the solution of Upy-gelatin due to coordination interaction between carboxylate (COO^-) groups of gelatin and the Fe^{3+} ions.

5.2. Host−Guest Interactions

Two main classes of macrocyclic compounds, cyclodextrins (CDs) and cucurbit[n]urils (CB[n]s), serve as hosts to provide the cavity space for complexation with diverse guest

https://dx.doi.org/10.1021/acs.chemrev.0c00015
Chem. Rev. 2020, 120, 10834−10886

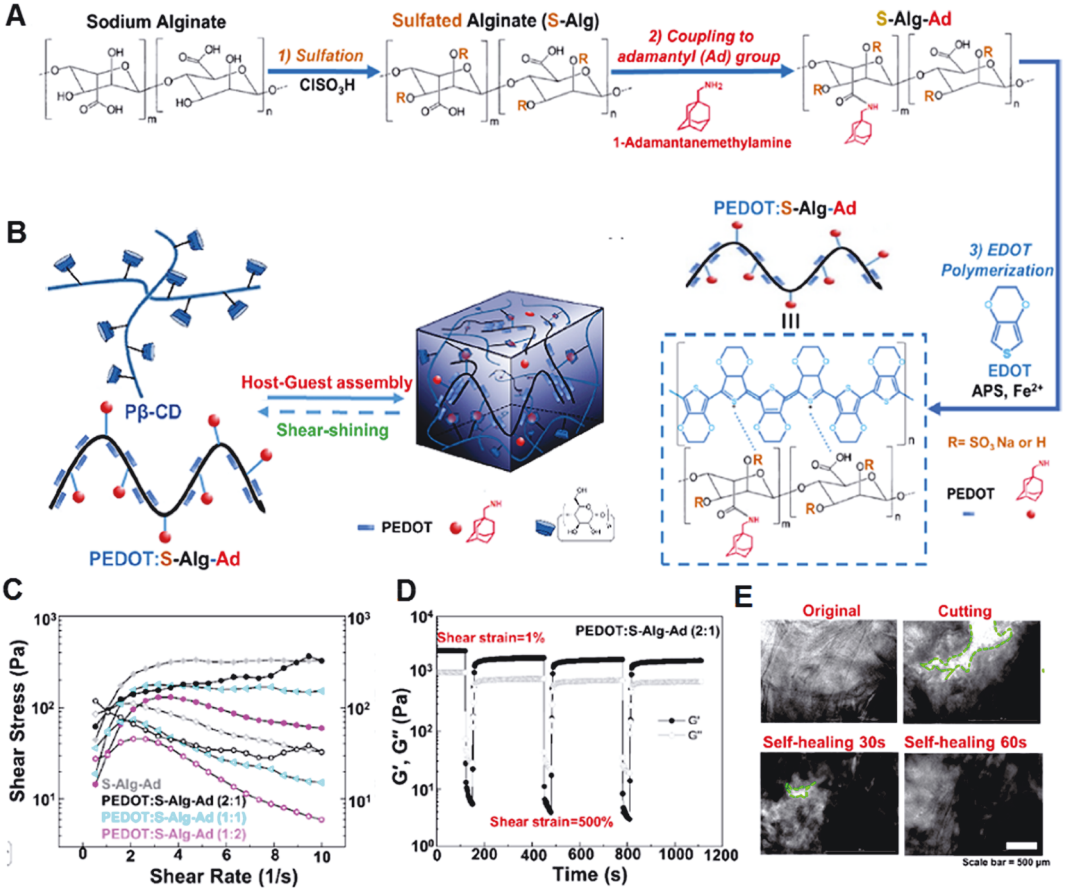

Figure 7. (A) Scheme of the synthesis of PEDOT:S-Alg-Ad polymers. (B) Schematic of dynamic cross-link formation utilizing host−guest complexation. (C) Continuous flow experiments showing the shear stress (closed symbols) and viscosity (open symbols) of different host−guest conductive hydrogels. (D) Self-healing property of the conductive hydrogel when the alternate step strain switched from 1 to 500%. (E) Bright-field images of the self-healing process of PEDOT:S-Alg-Ad (2:1)/Pβ-CD hydrogels. Reproduced with permission from ref 157. Copyright 2019 American Chemical Society.

compounds.[148,149] These host compound-based supramolecular interactions have been utilized to produce the various dynamic hydrogels.

5.2.1. Cyclodextrin-Mediated Supramolecular Interaction. CDs are a family of cyclic oligosaccharides consisting of macrocyclic glucose subunits connected through α-1,4-glycosidic linkages. CDs have a hydrophobic interior cavity with a hydrophilic exterior.[148] The main members of CDs are α-CD, β-CD, and γ-CD, which are composed of six, seven, and eight D-glucose units, respectively. The height of all these CDs is the same (7.8 Å), whereas the minimum diameters (4.4−7.4 Å) and the volumes (174−427 Å^3) of the cavities are dependent on the number of D-glucose units.[148,150] In the aqueous phase, CDs possess a cavity allowing the guests to form inclusion complexes through hydrophobic and van der Waals interactions.[148,151] To date, various design approaches of CD-based host−guest interactions have been demonstrated to generate shear-thinning and/or self-healable supramolecular hydrogels.[152−156] Most of these systems have cross-linked networks formed from the interaction between CD-conjugated polymers and their respective guests.

Xu et al. developed a self-assembled conductive hydrogel formed through the β-CD-adamantane (Ad) host−guest interaction.[157] An electroconductive polymer (PEDOT:S-Alg-Ad) was synthesized by oxidative polymerization of 3,4-ethylenedioxythiophene (EDOT) in the presence of adamantyl-modified sulfated alginate (S-Alg-Ad) (Figure 7A). The PEDOT:S-Alg-Ad polymer formed the hydrogel via host−guest recognition between adamantane moieties in S-Alg-Ad and CDs in poly-β-cyclodextrin (Pβ-CD) (Figure 7B). In a rheological examination, the viscosity of hydrogels decreases with increasing shear rate, indicating that they exhibited shear-thinning behavior (Figure 7C), which could be modulated by the hydrogel composition. This property allows this hydrogel to readily encapsulate cells and to be injected to form 3D constructs. Also, this hydrogel can be rapidly recovered through multiple cycles ($G' > G''$) when the applied strain is removed (Figure 7D). The hydrogel exhibited excellent self-healing properties. When the two separated pieces of the hydrogel were in close contact, the gap rapidly disappeared, undergoing complete self-healing within 60 s (Figure 7E). The physical cross-links in the interfaces between two individual pieces could be reconstructed through host−guest interactions. The mechanical stability of the hydrogels could be improved by the additional $\pi-\pi$ stacking and the sulfate anion−π interactions.[158] Moreover, this conductive PEDOT:S-Alg-Ad/Pβ-CD hydrogel matrices support the survival, proliferation, and differentiation of encapsulated myoblasts due to the well-established PEDOT properties,[159−161] thereby dramatically promoting myotube-like structure formation. These injectable conductive hydrogel matrices can be used as bioinks to produce 3D tissue constructs that electrically control cellular behavior.[162,163]

https://dx.doi.org/10.1021/acs.chemrev.0c00015
Chem. Rev. 2020, 120, 10834−10886

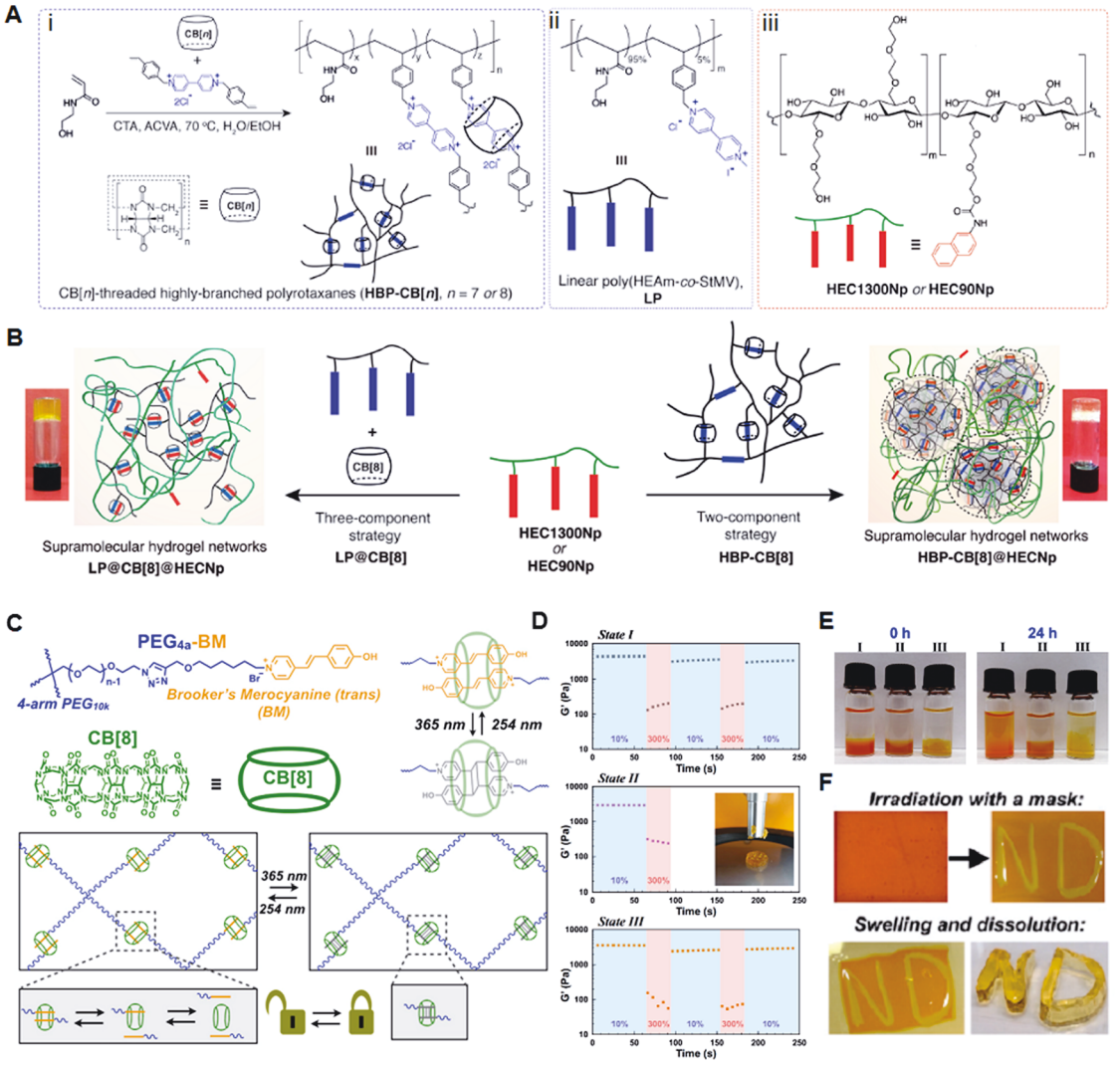

Figure 8. (A) Schematic illustration of (i) synthesis of the highly branched CB[n]-threaded polyrotaxane (HBP-CB[n]) via a semibatch RAFT polymerization in the presence of CB[n] (CTA, chain transfer agent (benzyltrithiocarbonyl propionic acid), and ACVA: 4,4′-azobis(4-cyanovaleric acid)), (ii) chemical structures of its linear analogue (LP), and (iii) naphthyl-functionalized hydroxyethyl cellulose (HECNp). (B) Formation of hydrogel networks through a two-component strategy from HBP-CB[8] polyrotaxane (HBP-CB[8]@HECNp) or a three-component strategy from its linear analogue (LP@CB[8]@HECNp). Inset: inverted vial tests for the hydrogel networks. Reproduced with permission from ref 178. Copyright 2018 Wiley-VCH. (C) Light-controlled supramolecular hydrogels. (D) Step-strain rheology alternating between 10% staring and 300% strain for physically cross-linked hydrogels (state I), chemically cross-linked hydrogels (state II), or hydrogels with cross-links reversed by exposure to 254 nm irradiation (state III). (E) Hydrogel swelling and dissipation determined by bathing preformed hydrogels in water and hydrogel stability through vial inversion. (F) Hydrogels were patterned by irradiation with 365 nm light using a mask, and the remaining supramolecular network was dissolved in water to leave a patterned covalent hydrogel. Reproduced with permission from ref 187. Copyright 2019 The Royal Society of Chemistry.

Noncovalent host−guest interaction between cationic peptide amphiphiles (PAs) bearing either β-CD or adamantane (Ad) groups can be induced to form self-assembling hydrogels. To date, a variety of PA fibrous assemblies have been designed for diverse functional hydrogels. Most PA hydrogels are based on noncovalent interactions, such as hydrogen bonding and van der Waals interactions between β-sheet structures.[164−167] Redondo-Gómez et al. developed PA self-assembled hydrogels.[168] Two PA-conjugates that participated in hydrogel formation were β-CD-PA (host) and Ad-PA (guest). These host−guest PAs are composed of a hydrophobic palmitoyl tail (C_{16}), an oligopeptide sequence (V_3A_3) that induces the β-sheet formation, an ionic trilysine region for further hydrogelation (K_3), a triglycine spacer (G_3), and a 1,2,3-triazole linker near the C-terminus of the PAs to incorporate β-CD or Ad moieties. This dynamic host−guest interaction induced the formation of a hydrogel with PA nanofiber structures comprising β-CD-PA and Ad-PA nanofibers. This PA hydrogel exhibited shear-thinning and self-healing properties. When undergoing strain changes from large (100%) to small (0.1%), the hydrogels underwent a reversible gel−sol transition, and their G' and G'' values rapidly recovered up to 90%. This peptide-based supramolecular approach may generate a new class of hydrogels with modulated rheological and mechanical properties, which may be achieved not only by manipulating functional groups in nanofiber surfaces but also by controlling various parameters, such as the concentration and composition of each host−guest PA species.

Wang et al. developed an injectable, host−guest assembled hydrogel between CD-conjugated branched polyethylenimine (CD-PEI) and Ad-conjugated 8-arm PEG (Ad-PEG) for local siRNA delivery.[169] CD-PEI was synthesized by the reaction of PEI with tosylated β-CD and had ~25 CD units per PEI. For the

https://dx.doi.org/10.1021/acs.chemrev.0c00015
Chem. Rev. 2020, 120, 10834−10886

preparation of Ad-PEG, thiolated adamantane was reacted with 8-arm PEG-maleimide through a Michael addition reaction. At a concentration of 20 wt %, CD-PEI and Ad-PEG, with an equimolar ratio of CD and Ad, formed the supramolecular hydrogels through CD-Ad host−guest interactions. The hydrogel showed typical viscoelastic behavior and G' increased as the frequency increased. The hydrogel also exhibited shear-thinning behavior and rapid self-healing. Under oscillatory strain (250% and 0.5%), the storage modulus at high strain decreased ∼40% and was rapidly recovered within 1 s when returned to low-amplitude strain. The use of cationic PEI as a main polymeric component enables the loading of anionic siRNA into the hydrogel matrix through electrostatic interactions.[170,171] This work is an excellent example suggesting that host−guest recognition-based printable hydrogels can be tailored by selecting relevant chemical structures for specific applications.

5.2.2. Cucurbit[n]uril-Mediated Supramolecular Interaction. CB[n]s are macrocyclic compounds consisting of glycoluril monomers linked by methylene bridges, where n is the number of glycoluril units.[172] The most frequently used CB[n]s are CB[6], CB[7], and CB[8], synthesized from six, seven, or eight glycoluril monomers, respectively.[150] These CB[n] compounds have the same height of 9.1 Å, while their cavity diameters range from 5.8 to 8.8 Å and the interior volumes are in the range of 164−479 Å.[3150,173] CB[n] compounds have a hydrophobic internal cavity bordered by polar carbonyl groups at the cavity entrance. Similar to CD-based recognition, CB[n]-based host−guest interactions have also been employed to produce dynamic supramolecular hydrogels.[174−177] Tan et al. developed a supramolecular hydrogel prepared through dynamic host−guest interactions using a highly branched CB[8]-threaded polyrotaxane (HBP-CB[8]) and a linear naphthyl-functionalized hydroxyethyl cellulose (HECNp) (Figure 8A,B) based on a two-component strategy (HBP-CB[8]@HECNp).[178] HBP-CB[8], which acts as a key building material, contains mechanically locked CB[8] host molecules in its branched polymer backbone through inclusion complexation with viologen derivatives.[179] To demonstrate the superiority of this branched architecture in controlling the viscoelastic response, thermal stability/reversibility, and self-healing activity of the hydrogels, a control hydrogel with linear analogues was also prepared using a three-component strategy (LP@CB[8]@HECNp). The HBP-CB[8]@HEC1300 Np hydrogels not only exhibited much higher modulus (G' and G'') values than the LP@CB[8]@HEC1300 Np hydrogels but also exhibited a higher viscosity at low shear rates (≈2000 Pa·s at 0.1 s^{-1}), which was more dependent on the shear rate. The higher viscosity and magnitude of the moduli for the HBP-CB[8]@HEC1300 Np hydrogels could be ascribed to the more entangled and intertwined network structures compared to the linear polymer-based LP@CB[8]@HEC1300 Np hydrogel structures. Both the HBP-CB[8]@HEC1300 Np and LP@CB[8]@HEC1300 Np hydrogels exhibited shear-thinning behavior. The HBP-CB[8]@HEC1300 Np hydrogel showed rapid self-healing performance due to fast CB[8] host−guest association kinetics. The branched architecture of the CB[8]-threaded polyrotaxane motifs employed in this work affords modulation of the dynamics of the supramolecular hydrogel networks, which is probably not expected using the linear architecture-based networks.

Yu et al. demonstrated the microbead-based formation of supramolecular polymer networks assembled from HBP-CB[8] and HEC-Np, based on CB[8]-mediated host−guest interaction.[180] Using a microfluidic device, they developed microbeads with a complementary complex consisting of host HBP-CB[8] and guest HEC-Np. The moldable self-healing supramolecular hydrogels were fabricated by annealing the microparticles at 65 °C for 30 min. The resulting hydrogels were self-standing and exhibited self-healing properties due to the dynamic nature of the CB[8]-based host−guest interaction. This microdroplet-based injectable system can be extended for the generation of core−shell microbeads that not only impart dual functions in two domains but also load various bioactive agents in the core region for multifunctional hydrogel bioinks with desirable printability. Zou et al. described a supramolecular hydrogel in which cross-linked host−guest networks can be optically switched between physical and chemical cross-linking states.

Recently, CB[8]-catalyzed [2 + 2] photodimerization of trans-Brooker's merocyanine (BM) was observed between two BM guests encapsulated into the cavity of the CB[8] host.[181] This unique catalytic activity of CB[8] has afforded the synthesis of supramolecular polymers through the CB[8] host-mediated photodimerization of BM moieties.[182,183] Zou et al. extended the research scope to a host−guest supramolecular system with light-mediated reversibility of the photodimer, which is typically found for photoinduced [2 + 2] dimerization.[184−186] Figure 8C illustrates that PEG4a-BM and CB[8] form inclusion complex networks, which were reversibly switched between a dynamic and static state under light irradiation with different wavelengths. In the dynamic physical network state, a moldable and self-supporting hydrogel was prepared due to dynamic host−guest interactions. Upon irradiation at 365 nm, the hydrogel became a solid-like material with high elasticity owing to the [2 + 2] dimerization-induced chemical cross-linking. Subsequent irradiation at 254 nm confirmed the reversibility of the network by returning the system to its initial physical gel state. Step-strain alternating experiments between 10% and 300% strain indicate that the physical gel underwent self-healing behavior under several cycles (Figure 8D, state I). In contrast, the chemically cross-linked hydrogels did not show dynamic recovery behavior, and the hydrogel was mechanically destroyed at high strain (Figure 8D, state II). The dynamic self-healing property could be recovered by irradiating into the hydrogel in state II at 254 nm. Notably, the chemical hydrogel in state II not only maintained the original gel dimensions without significant swelling but was also printed with a high shape fidelity and mechanical stability (Figure 8D,E). The hydrogel with physical host−guest interactions exhibited shear thinning behavior, which can be desirable in bioinks for extrusion-based 3D printing applications (Figure 8F). In addition, the additional post-treatment with light after printing resulted in mechanically robust 3D constructs with high resistance to stress relaxation.

5.3. Metal−Ligand Coordination

Coordination interactions between organic ligands and metallic ions have been widely employed as reversible cross-links to generate dynamic supramolecular hydrogels.[188−190] To date, a diverse selection of metal−ligand pairs has produced various classes of hydrogels with modulated rheological and mechanical properties. In this section, we highlight the recent design strategies for dynamic hydrogels based on several metal-chelating cross-linking approaches in which the organic chelating ligands of interest include bisphosphonate (BP), carboxylate, catechol, and histidine.

https://dx.doi.org/10.1021/acs.chemrev.0c00015
Chem. Rev. 2020, 120, 10834−10886

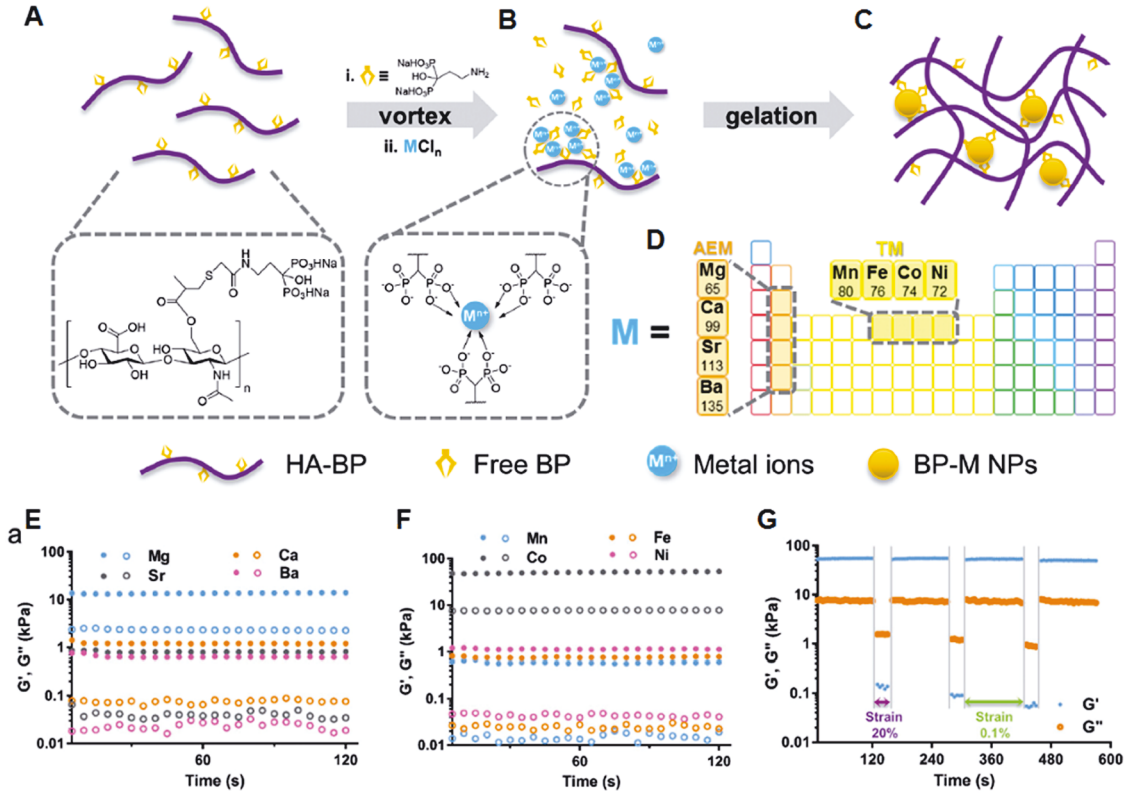

Figure 9. (A) Schematic illustration and molecular structure of bisphosphonate-modified hyaluronic acid (HA-BP). (B) Efficient in situ self-assembly of BP-M NPs surrounding grafted BP groups of HA-BP macromers via BP-M coordination. (C) Hydrogel networks are stabilized by the BP-M NPs. (D) Representative elements (AEM and TM) and diameters of corresponding divalent cations (numbers under the name of elements; unit, pm) used for hydrogel fabrication. (E,F) Representative oscillatory rheological analysis results of the nanocomposite hydrogels prepared with a series of AEM ions and TM ions, respectively. All hydrogels were prepared with identical concentrations of ions, free BP, and HA-BP. (G) Rheological data for the HA-BP-M nanocomposite hydrogels under alternating high (20%) and low shear (0.1%). Reproduced with permission from ref 190. Copyright 2019 Wiley-VCH.

5.3.1. Bisphosphonates. BPs, with two phosphonate groups ($PO(OH)_2$) covalently linked to a central carbon atom, have served as an organic ligand that exhibits an excellent binding affinity for diverse multivalent metallic cations such as calcium (Ca^{2+}) and magnesium ions (Mg^{2+}).[191−195] Some recent studies have shown that water-soluble polymers bearing conjugated BP moieties can form supramolecular dynamic hydrogels in the presence of metallic cations and metal-based inorganic particles.[196−198] The BP-based metal−ligand interaction has been extensively pursued as one of the main driving forces to produce dynamic cross-links in shear-thinning self-healing hydrogels. Shi et al. reported on a supramolecular hydrogel through the metal−ligand coordination between BP-conjugated hyaluronic acid (HA-BP) and Ca^{2+} ions.[199] HA-BP was synthesized based on a thiol−ene photoaddition reaction between thiolated HA and acrylamide-functionalized BP.[197,200] Immediate hydrogel formation, through a coordination interaction between ionized BP and Ca^{2+} ions, was observed when HA-BP was mixed with Ca^{2+} ions in water. The hydrogels showed the shear-thinning and rapid self-healing characteristics, which could be attributed to the reversible dynamic nature of the BP-Ca^{2+} coordinated cross-links. The G' value recovered immediately when the strain decreased from a high value (400%) to a low value (1%). This dynamic property of the hydrogel was supported by the self-healing behavior in which two pieces of hydrogels could be joined together. When extruded through a printer nozzle on the glass surface, the HA-BP/Ca^{2+} hydrogel formed self-standing 3D structures, indicating its potential as a bioink with good printability. Similarly, Zhang et al. demonstrated BP-Mg^{2+} coordination-induced hydrogel network formation.[141] When acrylated BP (Ac-BP) and Mg^{2+} ions were mixed with HA-BP in the aqueous phase, assembled Ac-BP-Mg nanoparticles (Ac-BP-Mg-NPs) were formed, which acted as a cross-linker to stably hold the networks of HA polymer chains. This in situ cross-linking process resulted in hydrogel formation in 20 min. Because of the reversibility of the BP-Mg^{2+} multivalent cross-links, the hydrogel exhibited both excellent injectability and self-healing properties. This characteristic was supported by the almost instantaneously recovered G' value of the hydrogels upon switching from high (100% or 200%) to low shear strain (1%). In addition, the Ac-BP present in the hydrogel network can be used for postphotopolymerization of acrylate groups, thereby resulting in the formation of chemical cross-links. This dynamic hydrogel possessing the potential for post-treatment may offer a benefit in providing robust and stable 3D constructs through 3D printing processes.

Recently, researchers reported on a series of HA-based supramolecular hydrogels that were also stabilized by in situ formed NPs and were assembled through interactions between the BP ligand and various divalent metal ions (M).[190] The self-assembled HA-BP-M hydrogels were formed by the simple mixing of HA-BP, free BP, and various metallic ions under aqueous conditions (Figure 9A−D). The divalent cations of various alkaline earth metals (AEMs) or transition metals (TMs) were coordinated to multiple BP ligands to form BP-M NP cross-links for establishing dynamic hydrogel networks.

https://dx.doi.org/10.1021/acs.chemrev.0c00015
Chem. Rev. 2020, 120, 10834−10886

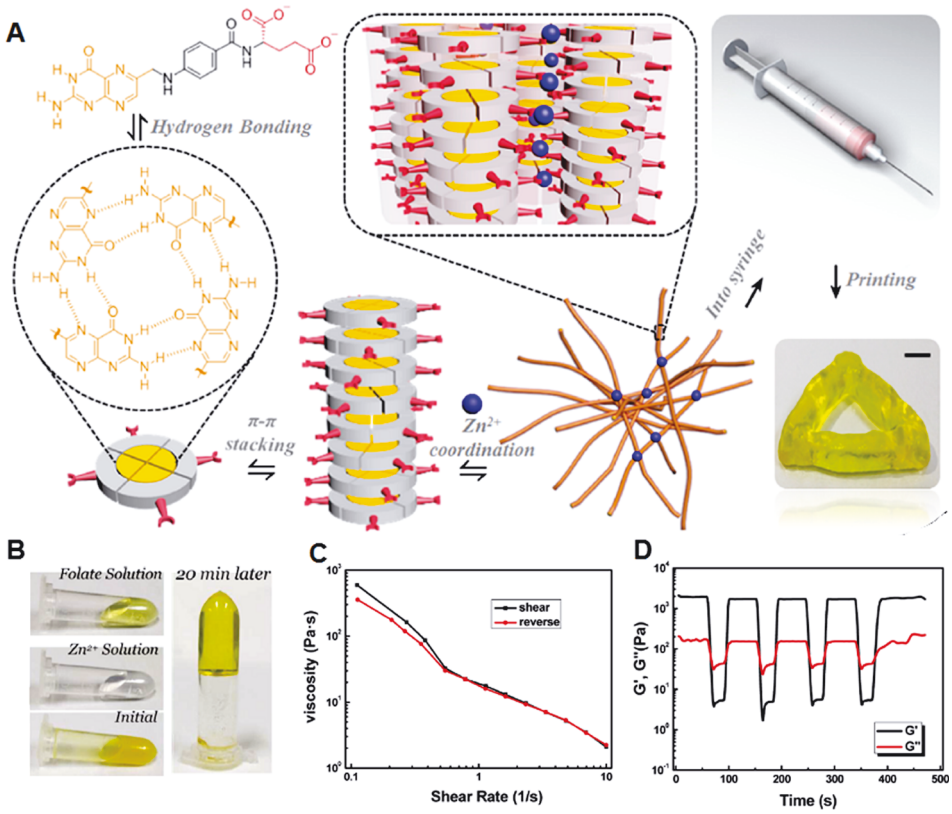

Figure 10. (A) Illustration of the hierarchical self-assembly process during gelation and the Printed hollow triangle structure. (B) Gelation in the folate/Zn^{2+} system. (C) Viscosity of folate/Zn^{2+} hydrogel at an increased shear rate followed by reverse shear rate decrease in continuous flow experiments. (D) Continuous step-stain measurements, which were carried out in steps of 50 and 0.5% oscillatory strain for four cycles (Hydrogels used in (C) and (D) were [folate] = 15 mM, folate/Zn^{2+} = 1/1.8). Reproduced with permission from ref 207. Copyright 2018 American Chemical Society.

Interestingly, the G' and G'' values were dependent on the diameter of the NP cross-links (Figure 9E,F). The moduli of the hydrogels decreased from the Mg^{2+} system to the Ba^{2+} system as the size of the BP-M NPs increased. For the TM-based NPs, the HA-BP-Co hydrogels, cross-liked with the smallest NPs, showed the largest G' and G'' values. For the HA-BP-M hydrogels, at a high shear strain, G' decreased dramatically to a level below that of G'', revealing a shear-thinning behavior of the hydrogels. The excellent recovery ability was also observed using oscillatory strain experiments (Figure 9G). This work provides a useful strategy for controlling the dynamics of metal−ligand coordinated hydrogels. Considering their printability as bioinks, the rheological and mechanical properties of these hydrogels may be easily optimized depending on the class of metallic ions.

5.3.2. Carboxylates. Coordination between carboxylates and metal ions has also been diversely considered to prepare dynamic physical hydrogels.[201−205] Zhang et al. reported on a key role for the coordination of ferric ions (Fe^{3+}) and carboxylates in the gelation of UPy-functionalized gelatin.[147] The formation of shear-thinning hydrogels was dominated by the Fe^{3+}-carboxylate coordination, and the quadruple hydrogen bonds formed by each UPy moiety improved the mechanical strength and self-healing ability by providing additional physical cross-linking. Shao et al. developed physically cross-linked networks of poly(acrylic acid) (PAA)-based nanocomposite hydrogels through hydrogen bonding and dual metal-carboxylate coordination interactions.[206] The Fe^{3+} ions and oxidized cellulose nanofibrils (CNFs) with carboxylates mainly acted as cross-linkers to produce the shear-thinning and self-healing poly(acrylic acid) (PAA)-based hydrogels. The Fe^{3+} ions formed three types of metal−ligand coordination bonds in PAA−PAA, PAA-CNF, and CNF-CNF. As the Fe^{3+} concentration increased, the dynamic moduli and the stiffness of the physical hydrogels increased due to the synergetic relaxation of multiple coordination bonds.

Liu et al. described metal−ligand coordination-triggered hierarchical folate/zinc supramolecular hydrogels.[207] The folate molecules were found to form tetramers with a planar structure through intermolecular hydrogen bonding, and the subsequent $\pi-\pi$ stacking interactions between tetramers formed the supramolecular fibrous structures (Figure 10A). This assembly behavior of folate is based on the liquid crystal-inducing pterin ring structure.[208−210] The addition of Zn^{2+} ions induced the cross-linking of stacked tetramers to build the fibrillar structure through carboxylate−Zn^{2+} interactions, resulting in the hydrogel formation. The hydrogels were formed by simple mixing of aqueous solutions of folate and Zn^{2+} ions in an alkaline pH range (pH > 10) (Figure 10B). The G' value was largely dependent on the molar ratio of folate/Zn^{2+} and was increased by approximately 5 orders of magnitude (from 10 to 10^6 Pa) when the ratio increased from 1.7 to 2.0. This result showed that the increased density of cross-linkers greatly improved the mechanical properties of the hydrogel. The multiple long-range interactions between Zn^{2+} and the hierarchical folate structures resulted in the hydrogel, showing shear thinning behavior (Figure 10C). Continuous step-stain measurements showed the excellent recovery ability of the folate/Zn^{2+} hydrogels (Figure 10D). Moreover, the hydrogel could be injected and printed,

https://dx.doi.org/10.1021/acs.chemrev.0c00015
Chem. Rev. 2020, 120, 10834−10886

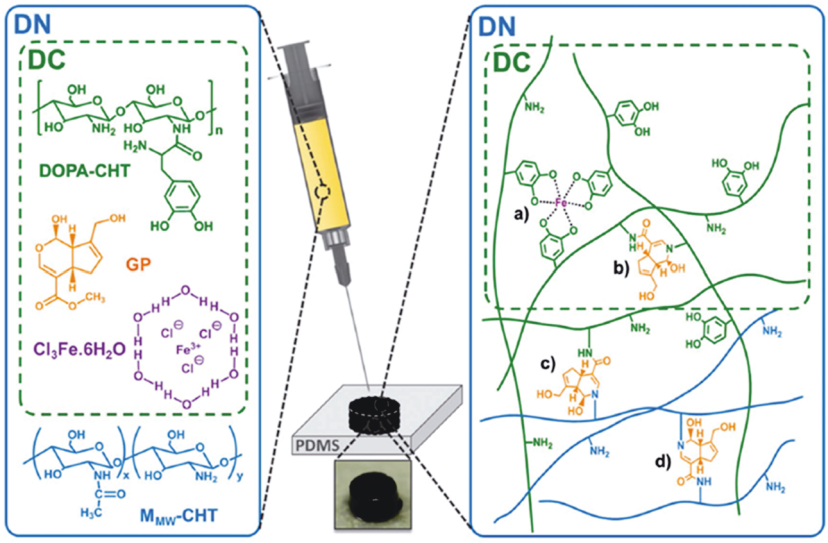

Figure 11. Schematic representation of the method developed to fabricate the DC and DN hydrogels. Besides the DOPA-CHT, GP, and Fe^{3+} ions, DN hydrogels are also composed of *M*MW-CHT. Inset: picture of the obtained hydrogels (DC and DN showed a similar appearance). Two cross-linking processes were employed to produce the hydrogels, namely a covalent cross-linking using GP and a physical cross-inking through coordination bonds in the presence of Fe^{3+} ions. Therefore, DC hydrogels can be composed of bis- and tris-complexes Fe:DOPA-CHT (a) or/and covalent bonds between two DOPA-CHT chains (b). Additionally, DN hydrogel can also establish covalent bonds between a chain of DOPA-CHT and a chain of M_{MW}-CHT (c) or/and between two chains of *M*MW-CHT (d). Reproduced with permission from ref.[227] Copyright 2017 Wiley-VCH.

into various self-supporting 3D structures with good shape fidelity.

5.3.3. Catechols. Catechol−metal coordination bonds have generated a variety of dynamic hydrogels with self-healing properties.[211−215] Among various catechol−metal combinations, catechol−Fe^{3+} complexes have been the primary focus in the development of supramolecular hydrogel because a vast number of studies elucidated their formation and dynamics through intensive research on the cuticle of mussel byssal threads, whose hardness and extensibility are largely dependent on catechol−Fe^{3+} coordination bonds.[216−221] Hence, catechol−Fe^{3+} complexes have been an important choice as reversible cross-links to produce diverse classes of dynamic polymeric networks.[211,222−225] Li et al. prepared a dynamic hydrogel by incorporating iron oxide (Fe_3O_4) nanoparticles into a catechol-modified 4-arm PEG matrix through cross-linking by reversible catechol−Fe^{3+} coordination bonds on Fe_3O_4 nanoparticle surfaces.[226] The presence of Fe_3O_4 nanoparticles resulted in dynamic rheological and mechanical behaviors, which are normally observed with supramolecular physical hydrogels. The catechol−Fe^{3+} coordination on the nanoparticle surfaces provides a solid-like reversible injectable hydrogel behavior.

Azevedo et al. developed chitosan-based double-network (DN) or doubly cross-linked (DC) hydrogels formed from noncovalent catechol−Fe^{3+} coordination interactions and chemical bonds (Figure 11).[227] The main concept of this work is similar to that of mussel-inspired doubly cross-linked tissue adhesives, as reported by Fan and co-workers.[228] They used 3,4-dihydroxyphenylalanine (DOPA)-conjugated chitosan (DOPA-CHT) as the main building block for hydrogel formation. The DOPA groups bearing catechol groups act as cross-linking points for network formation through catechol−Fe^{3+} coordination bonds.[229] The dynamic nature of catechol−Fe^{3+} coordination bonds provided the hydrogel with a self-healing ability, which can allow the hydrogel to rapidly recover its initial mechanical properties. The additional chemical cross-linking by genipin mechanically improved the stiffness of the hydrogels. These hydrogels could be formed using a one-pot injection system. A dynamic oscillatory rheology study indicates the good self-healing ability of the hydrogels. In terms of printability, this property needs to be addressed to optimize the injection time period of the hydrogel precursors in a mixed state. An injection speed that is too fast may result in dispersion on the printed surfaces without forming 3D constructs with shape fidelity, while an injection speed which is too slow may induce poor injectability due to premature chemical cross-link formation.

Liu et al. developed self-healing hydrogels with doubly cross-linked networks and demonstrated the improvement of mechanical strength of wheat gluten hydrogels by in situ catechol−Fe^{3+} coordination.[230] Gluten molecules formed the first cross-linked network through their intermolecular physical interactions and the second network was formed through coordination interactions between Fe^{3+} and proanthocyanidins (PACs). PACs, a group of polyphenol compounds, acted as catechol-rich polymers and can form metal−catechol coordination complexes with various metal ions.[223,231] UV−vis spectroscopic analyses showed that bis- and tris-catechol−Fe^{3+} complexes were identified in hydrogel matrices. Oscillatory strain experiments demonstrated that the hydrogels exhibited good self-healing properties. Dynamic shear rheology experiments showed that the hydrogels exhibited stronger mechanical properties at the optimized condition for hydrogel preparation (0.5 mM Fe^{3+} and 2 mM PACs (pH 6.0) than those obtained at other conditions. Similar to DOPA, PACs can also be conjugated to polymer chains to produce catechol−Fe^{3+}-cross-linked networks of various dynamic hydrogels.

5.3.4. Histidine. Histidine (His)−metal coordination is one of the key interactions in mechanically stiffening natural materials, such as sandworm jaws and mussel byssus.[232,233] For example, it was reported that the presence of dynamic His−Zn^{2+} coordination bonds was significantly involved in the dynamic course of mussel byssal threads, in which His−Zn^{2+} bonds were broken during thread yield and are recovered

https://dx.doi.org/10.1021/acs.chemrev.0c00015
Chem. Rev. 2020, 120, 10834−10886

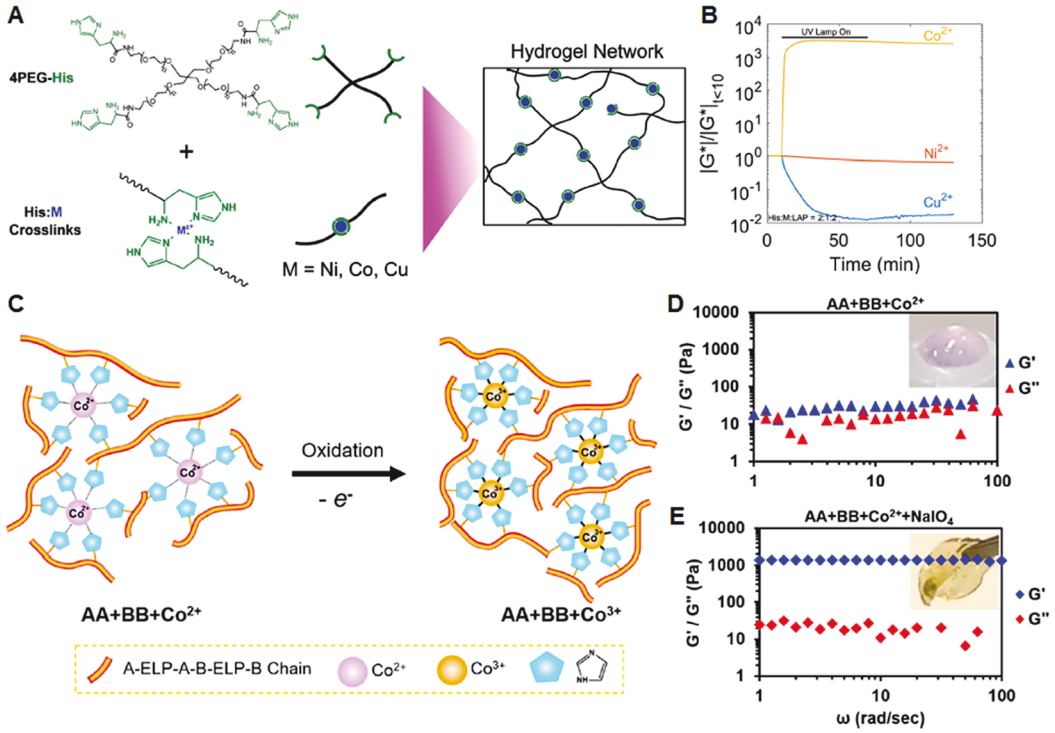

Figure 12. (A) 4-Arm PEG−His forms hydrogel networks with Ni^{2+}, Cu^{2+}, or Co^{2+} ions based on His−M^{2+} coordination complexes formation. (B) Viscoelastic properties of PEG−His-M^{2+} hydrogels controlled by longwave low-intensity UV irradiation (365 nm). Reproduced with permission from ref 241. Copyright 2017 The Royal Society of Chemistry. (C) Schematic showing the protein network assembled by SpyTag/SpyCatcher chemistry and Co/His6-tag coordination. AA, SpyTag-ELP-SpyTag; BB, SpyCatcher-ELP-SpyCatcher; ELP, elastin-like polypeptide. (D, E) Dynamic frequency sweep tests on the products of AA + BB + Co^{2+} and AA + BB + Co^{2+} + $NaIO_4$ with a fixed strain of 5%. The concentration of Co^{2+} is 3 mM. The insets show the products of AA + BB + Co^{2+} in the absence and presence of $NaIO_4$. Reproduced with permission from ref 239. Copyright 2019 American Chemical Society.

immediately upon thread relaxation.[234,235] These His−metal coordination bonds have been employed as reversible cross-links to produce diverse self-healing hydrogels.[236−238] The rheological and mechanical properties could be modulated by using different transition metal ions[237] or in situ control of the metal oxidation state.[239,240] Grindy et al. demonstrated that His formed complexes with transition metal ions (such as Ni^{2+}, Cu^{2+}, and Co^{2+}), which were cross-linked with the His-conjugated 4-arm PEG chains to produce supramolecular hydrogels (Figure 12A).[241] The viscoelastic properties of the hydrogels were controlled under ultraviolet (UV) irradiation in the presence of photoinitiator, LAP (lithium phenyl-2,4,6-trimethylbenzoyl-phosphinate). His−Cu^{2+}-coordinated hydrogels lost their initial rigidity, whereas the increased stiffness was found for His−Co^{2+}-complexed hydrogels (Figure 12B). For His−Ni^{2+} cross-linked hydrogels, the initial viscoelastic properties were maintained. These results indicate that the His−metal ion complexes exhibited different reactivities for the radicals generated by phototriggered dissociation of LAP. Enke et al. demonstrated that the type of counterion of the zinc salt tuned the mechanical and self-healing properties of His−Zn^{2+}-based hydrogels.[242] Using a RAFT polymerization technique, a His-bearing acrylamide/acrylate copolymer was synthesized and complexed with Zn^{2+} ions, which were ionized from $ZnCl_2$ and $Zn(OAc)_2$. When using $Zn(OAc)_2$ for hydrogel preparation, the stoichiometry of the His:Zn^{2+} was found to have one more His than when using $ZnCl_2$. From the chelation of more His moieties to Zn^{2+} ions, the presence of acetate counteranions produced hydrogels with improved moduli and hardness compared to that with chloride counterions.

Recently, Kou et al. developed recombinant protein-based hydrogels based on His−cobalt coordination interactions.[239] Two His6-tagged telechelic proteins (His6-SpyTag-ELP-RGD-ELP-SpyTag (AA) and His6-SpyCatcher-ELP-RGD-ELP-SpyCatcher (BB)) were synthesized in *Escherichia coli*.[243] His6-tags in the proteins acted as cross-linkers through chelation to Co^{2+} ions (Figure 12C). The resulting hydrogel lacked stiffness, showing a very low G' value (~20 Pa), close to that of G'' (Figure 12D). Interestingly, the oxidation of Co^{2+} into Co^{3+} by $NaIO_4$ rapidly resulted in the formation of an elastic solid with a greatly improved G' value of ~1.4 kPa (Figure 12E). Wegner et al. also reported that 4-arm His-modified PEG could be cross-linked with cobalt ions, and the in situ transition of the oxidation state of cobalt ions from Co^{2+} to Co^{3+} switched the gel state from a viscoelastic liquid to a highly elastic solid.[240] Taken together, the rheological and mechanical properties of His-metal coordination-based hydrogels can be tailored to develop novel bioinks with attractive printability for 3D bioprinting.

6. CHEMICAL STRATEGIES: DYNAMIC COVALENT BONDS

While physically cross-linkable hydrogels have many advantages for microextrusion bioprinting, the mechanical stability of the printed hydrogel-based constructs is usually low, and this weak resistance to deformation frequently requires post-treatment for stabilizing 3D tissue constructs. In contrast, chemical hydrogels cross-linked with a permanent covalent bond are mechanically stronger, but the network is irreversible once the cross-links are formed.[117] This nondynamic characteristics of chemical networks limit their applications as bioinks for 3D bioprinting.

https://dx.doi.org/10.1021/acs.chemrev.0c00015
Chem. Rev. 2020, 120, 10834−10886

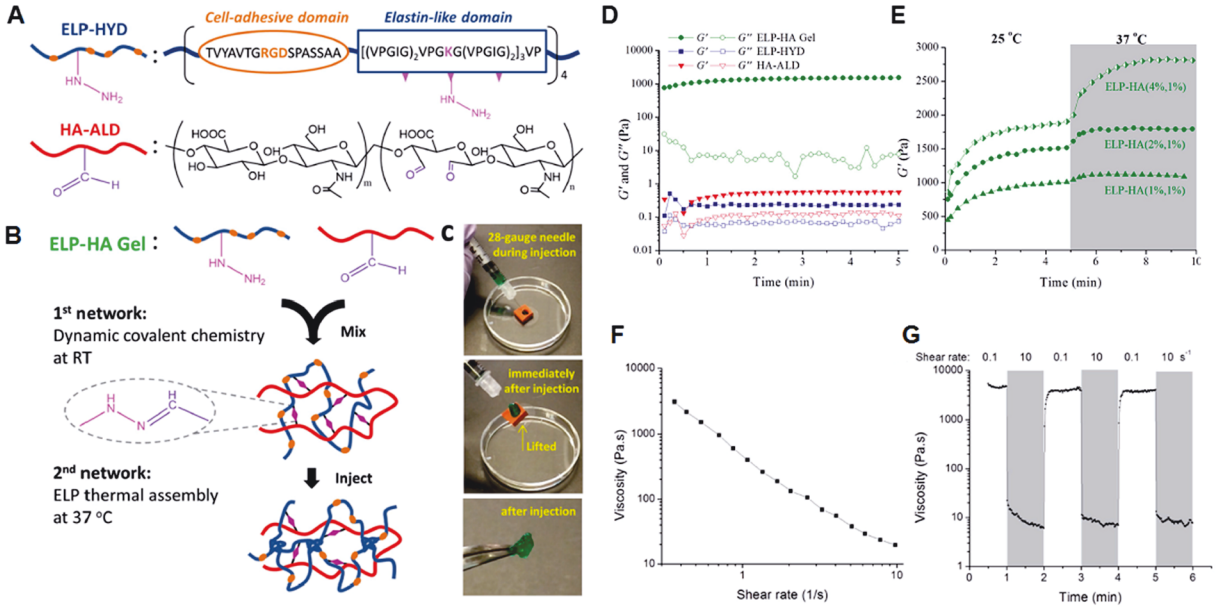

Figure 13. (A) ELP-HA is composed of hydrazine-modified elastin-like protein (ELP−HYD) and aldehyde-modified hyaluronic acid (HA−ALD). (B) Schematic of ELP−HA hydrogel formation. (C) Photographs demonstrating the injectability and rapid self-healing of ELP−HA hydrogels. (D) Oscillatory time sweep of ELP−HYD (4 wt %) and HA−ALD (2 wt %) before mixing and after mixing to form the ELP−HA (2, 1 wt %) hydrogel. Storage modulus (G') shown with filled symbols and loss modulus (G'') shown with empty symbols; tested at 25 °C. (E) Oscillatory time sweep of ELP−HA hydrogels for 5 min at 25 °C and 5 min at 37 °C. (F) ELP−HA hydrogel viscosity as a function of shear rate at 37 °C under continuous flow. (G) Shear-thinning and self-healing behavior of ELP−HA hydrogel under alternating shear rates of 0.1 and 10 s^{-1} at 37 °C. Reproduced with permission from ref 282. Copyright 2017 Wiley-VCH.

Current fabrication approaches of 3D tissue constructs via chemical gelation are normally based on the extrusion of mixed solutions containing two-component complementary reactive polymeric species or light/temperature-mediated polymerizable compounds.[244−250] Because the chemical networks form during the extrusion mixing state, it is critical to consider the various factors that affect the gelation behavior, including the homogeneity in the mixed solution as well as the mixing rate.[125] Excessively rapid cross-linking results in the clotting of the nozzles, whereas excessively late cross-linking induces spreading after extrusion and thus cannot produce self-standing 3D constructs.

Therefore, dynamic covalent bonds have attracted great attention in the generation of novel classes of hydrogels.[117,251] Dynamic covalent bonds are exceptional chemical bonds and are in a constant equilibrium state between bonded and dissociated states.[122] It is noteworthy that these bonds combine the strength of chemical bonds with the reversible properties of physical interactions, which can display the dynamic rheological behavior.[252] Chemistries for network formation through dynamic covalent bonds involve the formation of imine, hydrazone, oxime, disulfide, and boronic ester bonds, as well as Diels−Alder cycloaddition.[253,254] Hydrogels cross-linked with these dynamic bonds have advantages over those with permanent covalent cross-links in terms of fabrication of cell-laden 3D constructs because the dynamic rearrangement of these bonds allows cells to readily move and spread into the hydrogel structure.

Aiming toward new design approaches for the dynamic hydrogels, diverse chemical strategies have been suggested based on supramolecular assembly, macromolecular chemistry, colloidal nanoparticle-incorporated composite approaches, and so on.[119,255,256] A number of studies have afforded vast information on the structure−property relationship that determines the rheological properties of dynamic hydrogels. Thus, the diversity of design approaches may offer new insight into ideal bioinks with tunable rheological properties. In addition, newly developed design strategies may break down the limited scope of conventional hydrogels and may pave the way for the design of ideal bioinks for 3D bioprinting applications. In this review, we focus on dynamic hydrogels that exhibit their inherent properties at physiological pH and temperature. Hence, dynamic covalent bond-based dynamic hydrogels for which exchange reactions are activated by external stimuli, such as pH or UV light, are not discussed in this section. Examples of these dynamic covalent bonds include phenylboronate-salicylhydroxamate bonds,[257] phenylboronate-catechol bonds,[258] and reshuffling reactions of trithiocarbonate units.[259]

6.1. Imine Bonds

The formation of a Schiff base commonly occurs through a reaction between a primary amine and an aldehyde to produce an imine linkage under mild physiological conditions. The imine bonds can be reversibly hydrolyzed to return to the starting aldehyde and amine reactants;[260] they are in equilibrium, showing the dynamics between the bonded and dissociated states. This dynamic nature of the imine bonds has been used to produce a number of injectable and self-healing hydrogels.[261−264] For imine-based hydrogels, two different polymeric species with a primary amine or aldehyde are reacted in an aqueous phase. For example, a combination of amine-bearing chitosan and dibenzaldehyde-functionalized PEG (DF-PEG) with terminal benzaldehyde groups have been frequently selected to produce imine-based dynamic hydrogels.[264−266] Wang et al. reported on a dynamic hydrogel based on glycol chitosan (GC) and DF-PEG as a cross-linker.[267] The simple mixing of aqueous solutions of GC and DF-PEG resulted in hydrogel formation within 1 min. The hydrogels could be

https://dx.doi.org/10.1021/acs.chemrev.0c00015
Chem. Rev. 2020, 120, 10834−10886

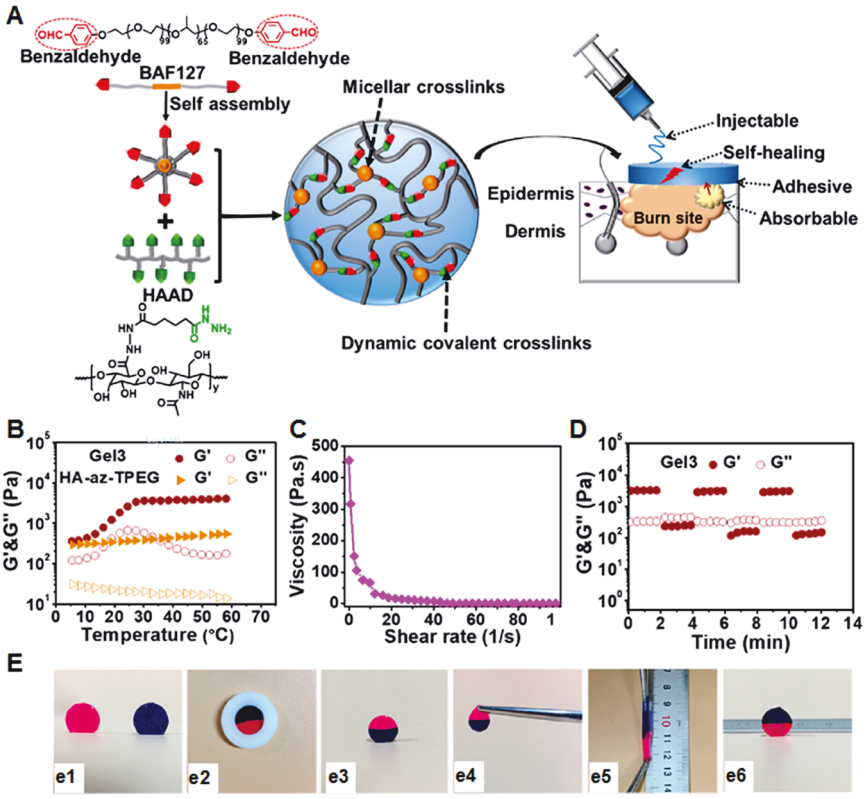

Figure 14. (A) Double cross-linked HA-az-F127 hydrogel. (b) Rheological results on (A) time sweep tests. (B) Temperature sweep tests in the temperature range of 4−60 °C at a frequency of 1 Hz, (G3 is the hydrogel with solid content of 15 wt % and the ratio of 5:5 (hydrazine to aldehyde)). (C) Viscosity as a function of shear rate. (D) G' and G'' of Gel3 from the continuous step strain measurements (1% → 300% → 1%) under 1 Hz. (E) Photographs of self-healing process: (e1) as-formed hydrogel, (e2) two halves of the hydrogel in PTFE mold, (e3, e4) self-healed hydrogel after 30 min, (e5) stretching with forceps; and (e6) recovered shape. Reproduced with permission from ref 285. Copyright 2018 American Chemical Society.

injected through a syringe needle (shear-thinning behavior) and had self-healing properties, which were ascribed to the dynamic equilibrium of the imine bonds between the bound and unbound state.[268−270] This hydrogel system showed tunable mechanical properties by varying the composition of GC and the DF-PEG cross-linker which modulated the cell proliferation behavior. They also suggested the versatile utility of this hydrogel by showing its potential as an injectable depot for cancer chemotherapy.[271,272] Xie et al. demonstrated excellent self-healing properties of the GC/DF-PEG hydrogels via a continuous step strain (from 1% to 300% and then 300% to 1%) evaluation.[273] At a higher dynamic strain of 300%, the G' value decreased from 1.2 kPa to 15 Pa due to the dissociation of dynamic imine linkages.[263] The G' value was rapidly recovered to its initial level as the strain changed from 300% to 1%. Qu et al. reported that the hydrogel formed from *N*-carboxyethyl chitosan (CEC) and DF-PEG showed injectable and self-healing characteristics.[274] Zhao et al. developed another class of injectable self-healing hydrogels by reacting quaternized chitosan-*g*-polyaniline with benzaldehyde-functionalized PEG-*co*-poly(glycerol sebacate) under physiological conditions.[275] The incorporation of electroactive polyaniline segments enabled the hydrogel to exhibit not only wound healing activity but also antioxidant activity. Generally, imine-based hydrogels have normally been built on the simple mixing of aldehyde-functionalized polymers and primary amine-bearing polymers. Control of the rheological behavior is mainly dependent on the composition of each polymer, whereas there is a lack of novel chemical strategies for the fabrication of imine-based hydrogels.

6.2. Hydrazone Bonds

Imine bonds are known to be susceptible to hydrolysis, which may be recognized as a weakness in terms of maintaining in vivo structural and mechanical stability of hydrogels.[254] Hydrazone bonds, as a close relative to imine bonds, are formed by reactions between aldehyde and hydrazide and show improved hydrolytic stability compared to that of imines. Hydrazone formation is based on a "click reaction"[276] and has been extensively pursued to form diverse hydrogels with dynamic cross-linked networks.[277−281] Wang et al. demonstrated injectable hydrogels that undergo a first network formation through hydrazone bond formation by the reaction between hydrazine-modified elastin-like protein (ELP-HYD) and aldehyde-modified HA (HA-ALD) (Figure 13A,B).[282] Upon heating to physiological temperature (37 °C), thermoresponsive phase segregation of ELP served as an additional physical cross-linking, which reinforced the network structure. The G' value of the ELP-HA hydrogel becomes approximately 1000 Pa less than 10 s after the mixing of ELP-HYD and HA-ALD (Figure 13D). The hydrogels from ELP-HYD with a larger portion of ELP domains showed a higher increase in the storage modulus (Figure 13E). The injectability and self-healing properties after injection through a 28 G needle were supported by the shear-thinning property of the ELP-HA hydrogels at physiological temperature (Figure 13C,F). Because of the reformation ability of dynamic covalent hydrazone bonds, the hydrogel networks exhibited rapid and reversible recovery behavior, which was shown by alternating the shear rate between 0.1 and 10 s^{-1} (Figure 13G). The ELP-HA hydrogels may meet the requirements of a bioink with good

https://dx.doi.org/10.1021/acs.chemrev.0c00015
Chem. Rev. 2020, 120, 10834−10886

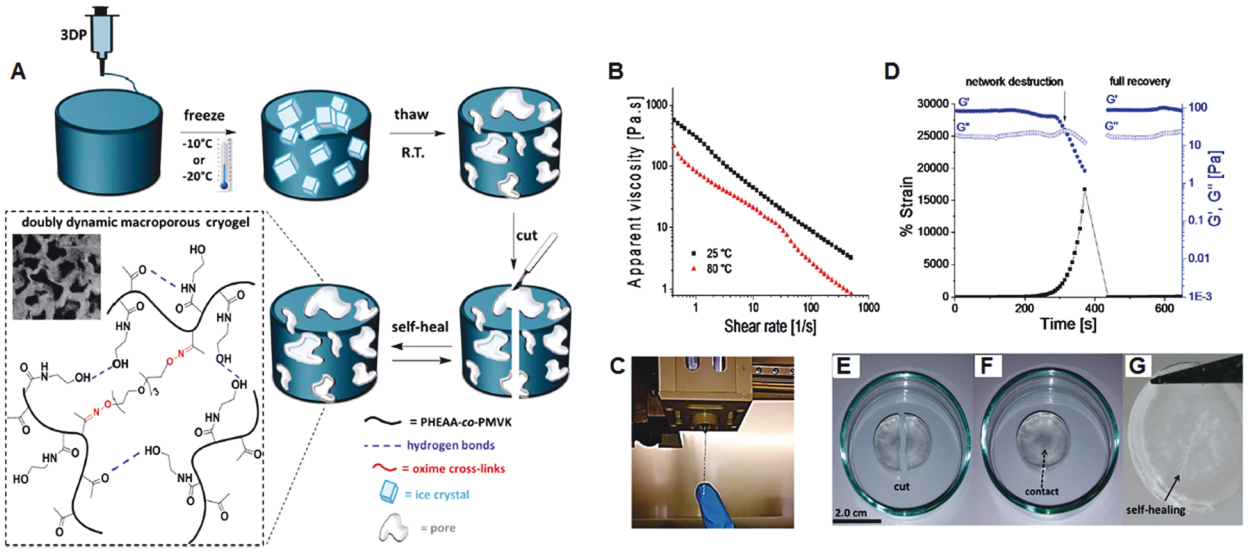

Figure 15. (A) Schematic of the methodology used to form 3D-printable, doubly dynamic self-healing cryogels. The inset demonstrates the chemical structure of the cryogels and their macroporous morphology. (B) Apparent viscosity curves of oxime-based hydrogels 25 °C (black squares) and 80 °C (red triangles). The gel exhibits shear thinning behavior, suitable for 3D printing. (C) A stable, shape-retaining extruded filament of oxime-based hydrogels. (D) Self-healing rheology of oxime-based hydrogels. (E) 3D-printed oxime-based hydrogel scaffold after three cryogelation cycles at −10 °C and induction of macroscopic cuts (a representative cryogel is demonstrated). (F) The damaged halves of the scaffold were brought into contact, to facilitate the healing process. (G) The damaged scaffold recovered from the cut and could be lifted as a single self-supporting unit after ∼3 h. Reproduced from the licensed article, ref 294, of a Creative Commons Attribution 3.0 Unported License.

printability. Their rheological properties can be further modulated by adjusting the degree of cross-linking formed from the dynamic covalent hydrazone bonds.

Wang and Burdick et al. also developed an injectable hydrogel cross-linked through dynamic covalent hydrazone bonds and estimated its applicability as a bioink for 3D bioprinting.[283] Upon mixing aqueous solutions of HA−hydrazide and HA−ALD, hydrogels that are resistant to flow were formed through hydrazone-based network formation. Contrary to physical cross-links that often undergo hydrogel relaxation over time (several minutes or hours),[153,284] the cross-links formed by dynamic covalent bonds normally have higher strength. In addition, the equilibrium of hydrazone strongly favors the bound state.[280] The hydrogel showed shear-thinning ability similar to that of previously reported hydrazone bond-based hydrogels[282] and could be ejected through a 27G × 1/2 in. syringe. Shear oscillatory rheometry studies showed that rapid self-recovery behavior, indicating the self-healing ability of the hydrogels. Additional photostiffening using thiol−ene-based interpenetrating networks, which was obtained by incorporating HA−norbornene and tetrathiol cross-linkers, increased the modulus of the hydrogel constructs up to ∼300%. Li et al. reported on a dynamic hydrogel (HA-az-F127 hydrogel) formed by the reaction between hydrazide-modified HA (HAAD) and benzaldehyde-functionalized F127 triblock copolymer (BAF127) micelles.[285] The BAD127 copolymer underwent thermoresponsive self-assembly to form core−shell type micelles, surface benzaldehyde groups of which could react with hydrazide moieties in the HA backbones to form dynamic acylhydrazone bonds (Figure 14A). The micellization of BAF127 is a key factor contributing to improving the mechanical strength of the HA-az-F127 hydrogel because HA-az-TPEG (the four-armed PEG with benzaldehyde terminals), which lacks the micelle-forming ability, shows lower strength (Figure 14B). The micellization of BAF127 resulted in the injectable dynamic hydrogel exhibiting shear-thinning properties (Figure 14C), and the oscillatory strain change shows that Gel3 exhibited rapid recovery and excellent self-healing properties. This reflects that the dynamic acylhydrazone covalent linkages dynamically underwent switching between the uncoupling and recoupling state in the hydrogel matrix (Figure 14D). When two individual half disks of the hydrogel, stained with Rhodamine B and methylene blue, were brought into contact, they combined into one piece of hydrogel with good extensibility under tensile force and showed excellent recovery ability to the original dimension after removal of the strain (Figure 14E). The researchers suggested the potential of using this acylhydrazone-based dynamic hydrogel as an injectable material for skin burn wound healing due to its tissue adhesiveness and good absorption properties.

6.3. Oxime Bonds

As another dynamic covalent bond similar to imine bonds, oxime bonds are formed through a "click reaction" between hydroxylamine/alkoxyamine and aldehyde or ketone.[276,286,287] Compared to that of imine and hydrazone bonds, the reaction equilibrium greatly favors bound oxime linkages and thus the hydrolytic stability of oxime bonds is known to be much higher.[254] Oxime bonds have also been used for the formation of reversible cross-links to prepare diverse dynamic hydrogels.[288−291] Most frequently, studied oxime-based cross-linked hydrogels are based on aldehyde-bearing oxidized HA or alginate, which are cross-linked by bifunctional alkoxyamine compounds. Baker et al. reported on cell-friendly tissue mimetic hydrogel constructs from bioorthogonal oxime bond formation between HA−aldehyde and PEG bis(oxyamine).[292] Wang et al. examined the catalytic influence of monovalent or bivalent salts on oxime reaction kinetics to obtain dynamic HA hydrogels. They found that the addition of monovalent or divalent salts to the mixed solution of HA−ALD and HA−aminooxy significantly reduced the gelling time compared to that of salt-free buffer solution.[293] Hafeez et al. prepared oxime-cross-linked

https://dx.doi.org/10.1021/acs.chemrev.0c00015
Chem. Rev. 2020, 120, 10834−10886

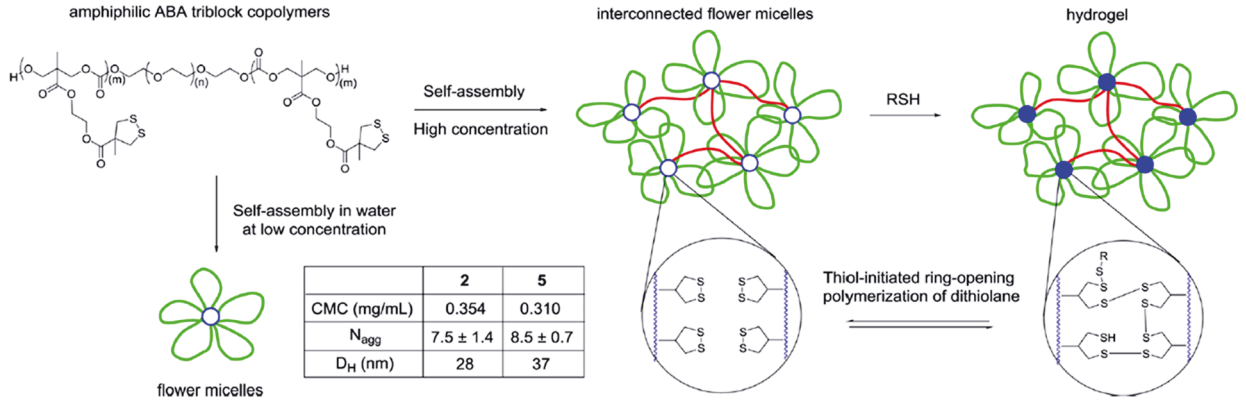

Figure 16. Proposed gelation mechanism for dithiolane-containing triblock copolymers in the presence of thiols. The physical cross-linking via the bridging PEG chains was shown in red. The chemical cross-linking via the thiol-initiated ring-opening polymerization of dithiolanes was shown in blue. CMC, critical micelle concentration; N_{agg}, aggregation number; D_H, hydrodynamic diameter. Reproduced with permission from ref 281. Copyright 2017 American Chemical Society.

injectable shear-thinning hydrogels through the reaction of aldehyde-bearing alginate with *O*,*O*′-1,3-propanediylbishydroxylamine.[290] Nadgorny et al. prepared an oxime-based hydrogel through a cross-linking reaction between poly(*n*-hydroxyethyl acrylamide-*co*-methyl vinyl ketone) (PHEAA-*co*-PMVK) and tetraethylene glycol bishydroxylamine (TEG−BHA).[294] The Schiff base reaction of bifunctional hydroxylamines in TEG−BHA with carbonyl groups in PHEAA-*co*-PMVK forms stable oxime linkages, which strongly hold the hydrogel networks (Figure 15A). The oxime-based hydrogels showed shear thinning behavior, which is suitable for 3D printing (Figure 15B). These dynamic hydrogels can be stably extruded under shear force (Figure 15C). The 3D-printed oxime-based hydrogels were treated by thermally induced phase separation (TIPS), which facilitated the formation of hydrogen bonds and oxime cross-links. The physical cross-linking through cryogelation-induced hydrogen bonding efficiently reinforced the oxime-based dynamic hydrogels. This post-treatment after 3D printing improved the mechanical strength of the printed oxime-cross-linked hydrogels by up to ∼1900%. Notably, the hydrogels exhibited an immediate recovery from destruction under high strain (Figure 15D). When two separate pieces of the hydrogels are in contact, an excellent self-healing property is observed (Figure 15E−G). Ghosh et al. reported on the synthesis of star-PEO-based hydrogels by cross-linking with oxime bonds.[295] End group-functionalized PEO_8-benzaldehyde (PEO_8−PhCHO) and PEO_8−oxyamine (PEO_8−ONH_2) were reacted to form tough hydrogel materials. The rheological and mechanical properties were proportional to the cross-linking density of the hydrogels. Although the main purpose of this work did not include studying the dynamic behavior, hydrogels that showed shear-thinning and self-healing properties could be fabricated by control of the reaction parameters, such as the cross-linking density, the unit ratio of aldehyde:oxyamine, and the mixing composition of each functional polymer for hydrogel preparation.

6.4. Disulfide Bonds

The disulfide bond is another class of dynamic covalent bonds that can generate the dynamic hydrogels with fast gelation kinetics. At neutral or alkaline pH, disulfide bonds are broken and reformed by the presence of free thiol groups, which produces dynamic and reversible hydrogel networks.[296−298] The dynamics of these hydrogels are usually dependent on thiol/disulfide exchange reactions, which are sensitive to high temperature, UV irradiation, or mechanical stress.[122] Yu et al. reported on the formation of thermosensitive dynamic hydrogels by simply mixing thiol-functionalized Pluronic F127 and dithiolane-modified PEG.[299] The thiol/disulfide exchange reaction is a key mechanism for dynamic network formation. The hydrogels as-prepared could be injected through a syringe needle and showed self-healing properties over a broad pH range from mildly acidic to alkaline conditions. The rheological properties of these hydrogels could be modulated by adjusting the mole ratio of thiol to dithiolane functional groups. Zhang et al. developed a self-healing hydrogel based on the self-assembly and gelation behavior of an ABA triblock copolymer containing a PEG middle block (B block) and terminal polycarbonate blocks (A block) with pendant 1,2-dithiolane groups.[281] This block copolymer self-assembled to form interconnected flower-type micelles that formed physically cross-linked networks. The dithiolanes in the core region of the micelles underwent thiol-initiated ring-opening polymerization to form dynamic and reversible networks (Figure 16). The rheological and mechanical properties of these dithiolane-derived hydrogels could be modulated by varying the ratio of the dithiolane moieties in the block copolymer. Oscillatory shear rheometry measurements showed that the disulfide-cross-linked hydrogels exhibited rapid and complete self-recovery behavior in contrast to the micellization-based physically cross-linked hydrogel that demonstrated poor self-recovery behavior.

It is known that the thiol−disulfide exchange reaction suffers from uncontrolled aerial oxidation of thiols to disulfides. As a thiol/disulfide exchange reaction, the exchange between Au-thiolate species and disulfide at biological pH has also been a motif for diverse injectable self-healing hydrogels.[300,301] Pérez-San Vicente et al. developed an injectable dynamic hydrogel formed from an Au-thiolate/disulfide exchange reaction.[302,303] The purpose of using Au-thiolate species is to efficiently protect the nucleophilicity of thiolates, which is required for the exchange reaction with disulfide. Dynamic hydrogels were fabricated by mixing an aqueous solution of thiol-terminated 4-arm PEG with aqueous $HAuCl_4$. The aerial oxidation of thiol groups in PEG chains at alkaline pH was not sufficient for self-standing hydrogels. The Au(I) ions induced hydrogel formation by acting as a cross-linker for thiolated PEG chains. The hydrogel showed increased mechanical properties as the frequency increased at physiological pH, which was ascribed

https://dx.doi.org/10.1021/acs.chemrev.0c00015
Chem. Rev. 2020, 120, 10834−10886

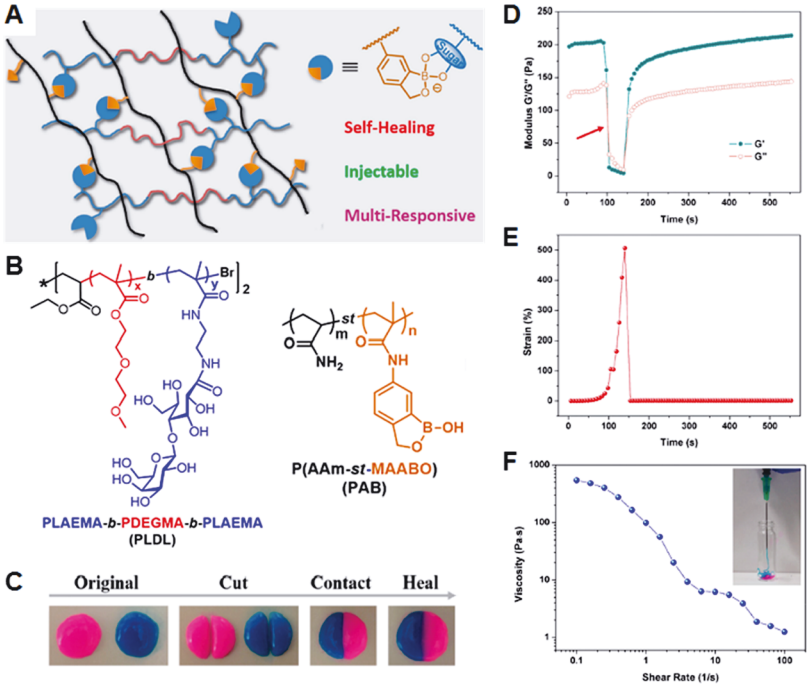

Figure 17. (A) Schematic illustration of injectable, self-healing, and multiresponsive hydrogel cross-linked by benzoxaborole−galactose complexation. (B) Chemical structures of PLDL (PLAEMA-*b*-PDEGMA-*b*-PLAEMA: poly(2-lactobioamidoethyl methacrylamide-*b*-di(ethylene glycol) methyl ether methacrylate-*b*-2-lactobioamidoethyl methacrylamide)) and PAB (P(AAm-*st*-MAABP): poly(acrylamide-*st*-5-methacrylamido-1,2-benzoxaborole)). (C) Images showing the self-healing process by reconnecting two pieces of hydrogel together. (D) Storage modulus and loss modulus value change in response to the imposed strain. (E) The corresponding strain variation: increasing first from 0.1% to 500% to break the gel and then dropping back to a small strain of 1% for gel recovery. (F) Shear-thinning property of the hydrogel. Reproduced with permission from ref 327. Copyright 2019 American Chemical Society.

to the permanent Au-thiolate/disulfide exchange.[300,301] Rheology experiments showed that this metal ion-involved disulfide-based dynamic hydrogel exhibited injectability and fast self-recovery properties. Although the disulfide bond is employed as one type of dynamic covalent bond for hydrogel network formation, its chemistry requires the presence of an alkaline pH above 8.5[304,305] or strong oxidants, such as iodine and hydrogen peroxide.[305,306] The pK_a of thiols is in the range of 8−10, and thus, basic conditions (pH > 8.5) were required to drive the reaction toward disulfide formation.[304]

Recently, Bermejo-Velasco et al. developed injectable disulfide cross-linked HA hydrogels by reducing the pK_a of the thiol group through the incorporation of an electron-withdrawing group at the β-position of thiol in cysteine or *N*-acetyl-L-cysteine.[307] Interestingly, the reduced thiol pK_a facilitated the formation of thiolate anions at physiological pH, allowing the formation of oxygen-catalyzed disulfide-cross-liked hydrogels at physiological pH within 3.5 min. This work may suggest that the chemical approach of controlling the pK_a of thiols has diverse utility in preparing various disulfide-based injectable (shear thinning) and self-healing hydrogels in a short time period at physiological pH without the need for oxidants.

6.5. Boronic Ester Bonds

The boronic ester bond is a popular dynamic covalent bond and has been used to produce diverse supramolecular assemblies and hydrogels.[308−311] This reversible bond is formed by the condensation of boronic acids with *cis*-1,2 or *cis*-1,3-diol compounds.[312,313] In particular, the reversible complexation of phenylboronic acid (PBA) (one example of arylboronic acids) and *cis*-diols has been widely employed as cross-links to form dynamic hydrogels.[314−316] Owing to having pK_a values in the range of 8−9, arylboronic acids have a limitation with respect to producing stable boronic ester-based cross-links at physiological pH.[308,309] Thus, the optimum pH for the formation of boronic esters is known to be approximately 9.0. However, it was reported that there still exist ionizable boronic acid groups (approximately 6% of the total boronate moieties) sufficient for binding to *cis*-diols at pH 7.4.[317,318] Pettignano et al. demonstrated the formation of boronic ester-based alginate hydrogels without adding external diol compounds or divalent cations, such as Ca^{2+} ions.[314] PBA-conjugated alginate formed a hydrogel under basic conditions (pH 9.0). The hydrogel showed thixotropic behavior and self-healing properties. Hong et al. also prepared identical dynamic hydrogel at physiological pH.[319] When dissolving PBA-bearing alginate (2.3 wt %) in the aqueous media (pH 7.4), the hydrogel was formed within 1 min. The dynamic rearrangement of boronic ester bonds provides hydrogels with self-healing and shear thinning properties. These works show the advantage of using a single-component gelling material over two- or three-component systems, which often suffer from inhomogeneous mixing and inconsistent, batch-dependent gelling and rheological behavior.

One recent approach that modulates the rheological and mechanical properties of boronic ester-based hydrogels involves incorporating another dynamic cross-linking motif. For example, Li et al. reported on a double dynamic network hydrogel, which was formed through two dynamic covalent bonds, borate ester, and imine bonds.[320] As a key component, the researchers synthesized multifunctional PEG (MF-PEG) with a benzaldehyde group and a PBA group at each chain terminus.[320] MF-PEG formed a doubly cross-linked network through a borate ester-forming reaction with poly(vinyl alcohol)

https://dx.doi.org/10.1021/acs.chemrev.0c00015
Chem. Rev. 2020, 120, 10834−10886

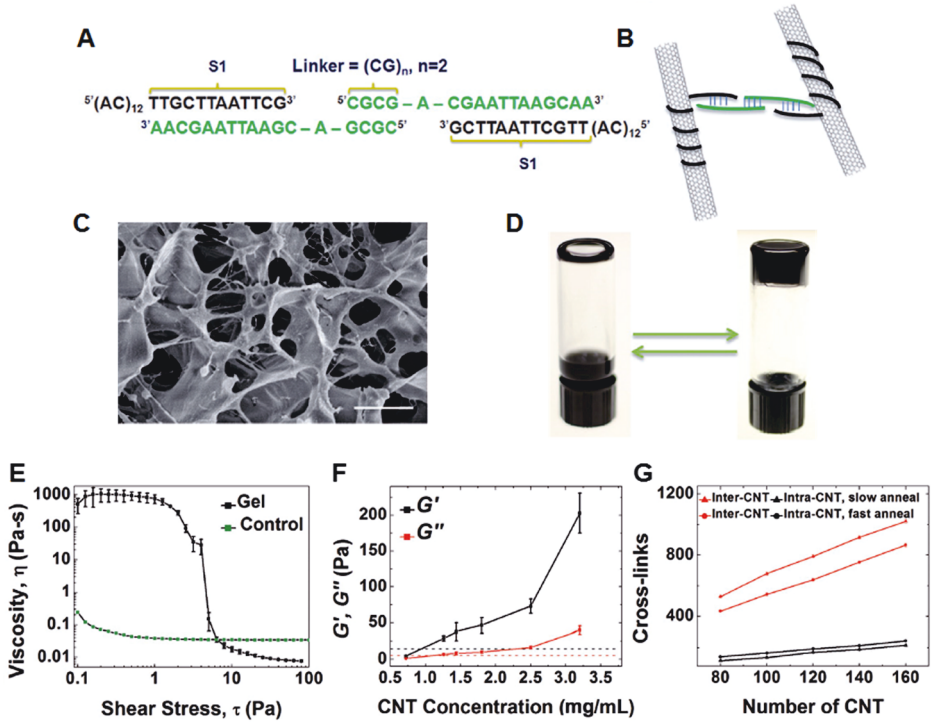

Figure 18. (A) DNA sequence $(AC)_{12}$S1 (black) is used to disperse SWCNTs. The linker DNA (green) has two regions: one complementary to S1 to hybridize with the SWCNT and one self-complementary (CG) repeat of variable length, separated by a single adenosine base. (B) Proposed structure upon gel formation, wherein $(AC)_{12}$S1 helically wraps around the SWCNT while the linker DNA forms duplexes with both S1 and other linker strands, thereby providing the cross-linking mechanism. (C) Cryo-SEM of a lyophilized SWCNT-DNA gel, showing a network of SWCNTs amid aggregated buffer salts and DNA. (D) Photographs of the inverted-vial test to demonstrate the sol−gel transition (solution on left and gel on right). (E) Viscosity versus shear stress for a typical gel, compared to an ungelled sample. (F) Storage (G') and loss (G'') moduli as a function of SWCNT concentration. Linker DNA concentration is increased in proportion to SWCNT concentration. Dashed black and red lines indicate moduli for a 5 mg mL^{-1} van der Waals gel. (G) Number of inter-SWCNT and intra-SWCNT cross-links in simulation, as a function of the number of SWCNTs for gel systems formed at slow and fast annealing rates. Reproduced with permission from ref 346. Copyright 2018 Wiley-VCH.

(PVA) and an imine-forming reaction with GC to produce a dynamic hydrogel in seconds under mild conditions (pH ≈ 7, 25 °C). Notably, the control of various parameters, such as the ratios of PVA/GC, amine/aldehyde, and diol/PBA, could modulate the rheological and mechanical behavior of the hydrogels.

As discussed above, due to the pK_a value of PBA (~8.8), efficient hydrogel formation is impeded at physiological pH. Moreover, considering in vivo use, the hydrogels may suffer from poor stability due to the dissociation of boronic ester bonds at physiological pH. For this reason, PBA analogues with pK_a values close to physiological pH have been employed to endow hydrogels with feasible stability under physiological conditions.[312,321] Benzoxaborole is a cyclic analogue of PBA with a pK_a value lower than physiological pH (~7.2) and forms stable five-membered boronate rings through complexation with *cis*-diols.[322,323] Benzoxaborole has been a preferred choice for forming diverse dynamic injectable and self-healing hydrogels applicable in physiological conditions.[324,325] Chen et al. developed a self-healing hydrogel using benzoxaborole-catechol dynamic covalent chemistry.[326] They synthesized two kinds of phosphorylcholine-containing copolymers, which have pendent benzoxaborole and catechol groups, respectively. Upon mixing aqueous solutions of these copolymers (PBS at pH 7.4), the hydrogel formed quickly within 30 s, which was attributed to the pK_a value of benzoxaborole (~7.2), being close to physiological pH.[312] The hydrogel exhibited high stability even after 24 h immersion in PBS solutions, indicating that the equilibrium favored the complexed tetrahedral boronates at physiological pH. The hydrogel showed rheological behavior typically observed for dynamic hydrogels, exhibiting shear-thinning and self-healing characteristics. Compared to PBA-based dynamic chemistry, the use of benzoxaborole-bearing polymers for complexation with *cis*-1,2 or *cis*-1,3-diol compounds may allow the production of hydrogel bioinks with excellent shape fidelity and mechanical stability. Chen et al. designed a dynamic hydrogel exhibiting shear-thinning and self-healing characteristics based on a thermosensitive copolymer with pendent galactose groups (PLDL) and a benzoxaborole-containing copolymer (PAB) (Figure 17).[327] Dynamic benzoxaborole−galactose complexation is a driving phenomenon for reversible network formation in a hydrogel matrix. Rheological analyses showed that the mechanical properties could be controlled by varying the galactose/benzoxaborole molar ratio. The hydrogels exhibited excellent self-healing ability, which could be explained by the dynamic nature of the boronic ester bonds. Step-strain experiments demonstrated that the rapid recovery of the hydrogel network. The viscosity of the hydrogel decreased with increasing shear rate, indicating a shear-thinning property desirable for injectable bioinks in 3D printing applications. The same research groups further identified the parameters that control the mechanical properties of similar benzoxaborole−galactose complex-based dynamic hydrogels.[328] By controlling the sugar content, the cross-linking density in the hydrogel was modulated, which tuned the mechanical strength of the hydrogels. The G' value could be controlled in the range of

https://dx.doi.org/10.1021/acs.chemrev.0c00015
Chem. Rev. 2020, 120, 10834−10886

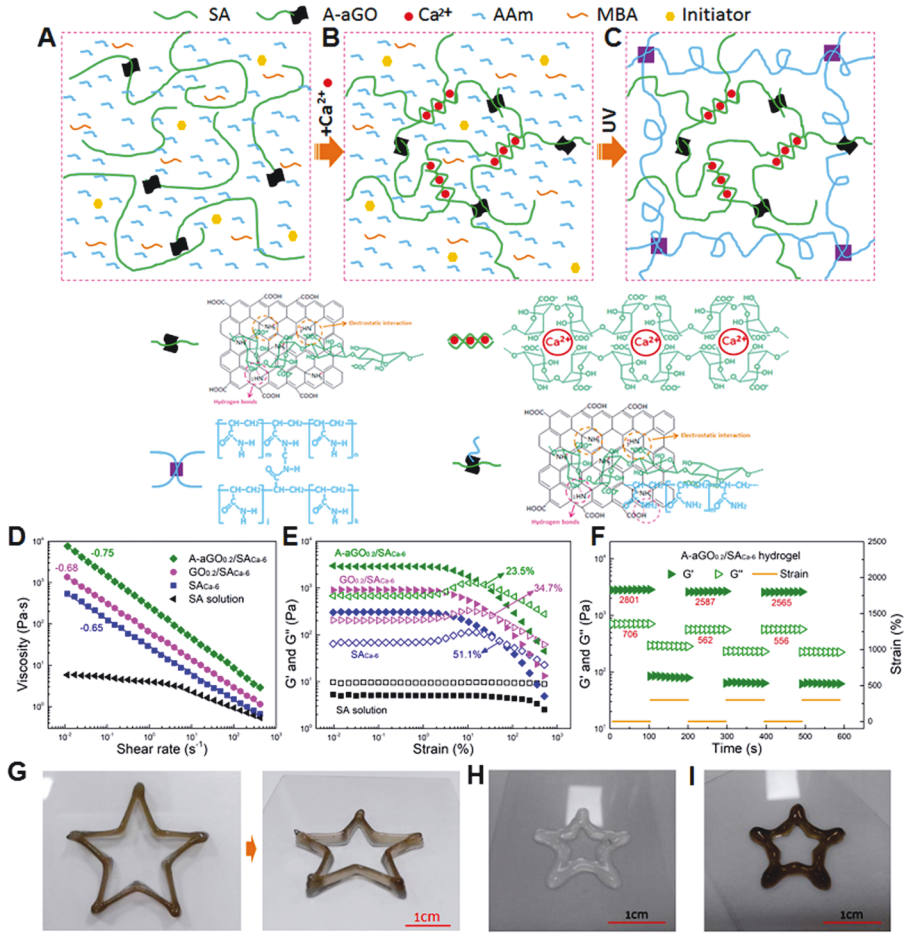

Figure 19. (A−C) Schematic diagrams for fabrication of the A-aGO/SA/PAAm nanocomposite hydrogel: (A) Homogeneous aqueous solution of SA, A-aGO, acrylamide (AAm), *N*,*N*′-methylene bis(acrylamide) (MBA), and photoinitiator. (B) Ca^{2+} ions inducing ionic association of SA chains. (C) UV exposure resulting in the final A-aGO/SA/PAAm nanocomposite hydrogel. (D) Apparent viscosity as a function of shear rate for the A-a$GO_{0.2}$/$SA_{Ca\text{-}6}$ and $SAC_{a\text{-}6}$ hydrogels as well as the SA solution without Ca^{2+} ions. (E) Storage modulus G' and loss modulus G'' as a function of oscillation strain at an angular frequency of 1 Hz for the A-a$GO_{0.2}$/$SAC_{a\text{-}6}$ and $SAC_{a\text{-}6}$ hydrogels as well as the SA solution without Ca^{2+} ions. (F) Changes of G' and G'' with time at alternant oscillation strains of 2% and 300% and at an angular frequency of 1 Hz for the A-a$GO_{0.2}$/$SA_{Ca\text{-}6}$ hydrogel, where the red numbers represent the average modulus at the oscillation strain of 2%. (G) Hollow pentagon printed from the A-a$GO_{0.2}$/$SAC_{a\text{-}6}$/AAm hydrogel bioinks (15 layers) viewed from the top and side. 3D printed hollow pentagon patterns from (H) the $SA_{Ca\text{-}6}$/AAm hydrogel and (I) the $GO_{0.2}$/$SAC_{a\text{-}6}$/AAm hydrogel inks, respectively. Reproduced with permission from ref 352. Copyright 2017 American Chemical Society.

261.2 Pa (20% sugar at pH 7.4) ∼ 2638.1 Pa (80% sugar at pH 9.4), suggesting a potential for designing bioinks with tailored mechanical properties optimized for 3D bioprinting.

7. CHEMICAL STRATEGIES: NANOCOMPOSITE HYDROGELS

Another category of significant emphasis is nanocomposite hydrogels, which are fabricated by incorporating nanomaterials into polymeric materials. This hybrid strategy using nanomaterials is innovative in generating multifunctional hydrogels with diverse functionalities.[255,329,330] The latest studies show that most of these nanocomposite hydrogels exhibit shear-thinning rheological properties.[256] The main modulator of this rheological property involves dynamic interactions of various physical bonds between the surface of nanomaterials and the hydrogels. Recently, various nanomaterials, including calcium carbon nanotubes (CNTs),[331−333] graphene oxide (GO) nanosheets,[334,335] calcium carbonate, Laponites,[336,337] silica nanoparticles, and gold and silver nanoparticles,[338−340] are employed in either unmodified or modified state. The rational combination of these nanomaterials with native or functionally modified polymers may also provide a deep understanding regarding a wide variety of choices in combinations of chemical species for 3D printable hydrogel bioinks. Herein, we provide a critical review of the design approaches of the most recent hydrogel systems in terms of their applicability in 3D bioprinting. Although the surface chemistry of some polymeric nanoparticles, including polymer latexes and micelles,[329] and cellulose nanocrystals,[341,342] has also been investigated for the formation of nanocomposite hydrogels, most chemical strategies have focused on the surface of inorganic nanomaterials due to the convenience and diversity in functionalization for developing nanocomposite hydrogels that exhibit shear-thinning and self-healing properties. In this section, we provide a detailed discussion on the role of inorganic nanomaterials exploitable for the novel design of printable bioinks for 3D bioprinting.

7.1. Nanocarbon-Based Hydrogels

Carbon nanotubes (CNTs) and graphene oxide (GO) nanosheets have been incorporated into physically cross-linkable hydrogels and have provided superior properties compared to those of the native hydrogels.[343−345] The addition of nanocarbon has modulated the rheological and mechanical character-

https://dx.doi.org/10.1021/acs.chemrev.0c00015
Chem. Rev. 2020, 120, 10834−10886

istics of the nanocomposite hydrogels through a diverse single or multiple interactions between nanocarbon and organic low molecular weight compounds or polymers, which are displayed by $\pi-\pi$, hydrogen bonding, electrostatic, and van der Waals interactions, among others.[332,334,345]

7.1.1. Carbon Nanotubes. Mansukhani et al. demonstrated single-walled carbon nanotube (SWCNT)-based nanocomposite hydrogels based on optimized deoxyribonucleic acid (DNA) linker chemistry.[346] They employed DNA base pairing as the cross-linking interaction in the formation of 3D networks in the nanocomposite hydrogels. The linker DNA strands consist of two regions: one is complementary to the SWCNT-adsorbed DNA (sequence S1), and the other is (CG) repeats of variable length (Figure 18A). A single adenosine (A) base is inserted between these two regions to enhance the flexibility of the linker strand.[347] For hydrogel formation, SWCNTs were dispersed in an aqueous solution of single-stranded DNA containing 12 adenosine cytosine (AC) repeats attached to S1. Because of the self-complementary feature of the CG region, a DNA cross-linked network of SWCNTs was produced through duplex formation between the SWCNT-bound linker DNA strands (Figure 18B). An SEM image shows that the lyophilized SWCNT/DNA hydrogel has a porous structure typically observed for supramolecular hydrogels (Figure 18C). This CNT-based hydrogel shows the sol−gel transition (Figure 18D). A shear stress sweep showed that the viscosity of SWCNT/DNA hydrogels was 900 Pa s at 1.8 mg/mL. When a noncomplementary linker was used, the mixed dispersion of SWCNT/DNA did not form hydrogels, indicating that the duplex linker was a key interaction for network formation. The addition of SWCNTs produced nanocomposite hydrogels with shear-thinning properties (Figure 18E). The G' value of the hydrogels could be controlled by the SWCNT concentration. A G' value of 200 Pa was measured at an SWCNT concentration of 3.2 mg/mL (Figure 18F), and the total number of inter-SWCNT cross-links can be modulated as a function of the SWCNT concentration (Figure 18G). Moreover, the SWCNT/DNA hydrogels underwent near-infrared (NIR)-controlled thermoreversible gelation behavior, which can be displayed by the photothermal property of the SWCNTs.[348,349] Under NIR irradiation, the viscosity of the hydrogels significantly decreased, whereas recovery to the original gel state was observed upon cessation of NIR irradiation. This work is an excellent example of using the unique complementary interaction of DNA to produce SWCNT-based shear-thinning injectable hydrogels.

Rehman et al. described CNT-incorporated poly(acryloyl-6-amino caproic acid) (PAACA)-based nanocomposite hydrogels.[350] They used oxidized CNTs to form cross-links with PAACA chains through hydrogen bonding interactions between amide and carboxyl groups in PAACA side chains and oxidized CNTs. These CNT/PAACA hydrogels could be prepared without any organic cross-linkers. They exhibited self-healing recovery behavior. The presence of CNTs in hydrogel matrices increased the gel strength from 60 kPa (PAACA hydrogels) to 320 kPa (CNT/PAACA hydrogels). The higher the CNT amount, the stronger strength the hydrogel exhibited. Liao et al. developed the functionalized SWCNT-containing dynamic hydrogels with reliable self-healing capability and string adhesiveness.[351] The hybrid network of these hydrogels were formed by dynamic supramolecular cross-linking among functional SWCNTs, PVA, and polydopamine (PDA), where hydrogen-bonding and $\pi-\pi$ stacking interactions were involved. The dynamic cross-links could be easily ruptured and reformed, imparting self-healing abilities to these hydrogels. The hydrogels exhibited rapid self-healing properties within 2 s and high self-healing efficiency of 99%.

7.1.2. Graphene-Based Nanomaterials. Like CNTs, graphene oxide (GO) has been introduced to improve the mechanical and rheological properties of the hydrogel-based bioinks for 3D bioprinting. Liu et al. reported on the fabrication of a 3D printable and mechanically robust hydrogel based on alginate and GO nanosheets.[352] They focused on the key role of the alginate-functionalized GO (A-aGO) in modulating the mechanical and rheological properties of A-aGO/SA hydrogels. For the synthesis of A-aGO, GO dispersed in alginate-containing water was first aminated using the Bucherer reaction, which partially converts phenolic oxygens on the GO to primary amines ($-NH_2$).[353,354] The aminated aGO formed A-aGO with anionic alginate through both electrostatic and hydrogen-bonding interactions (Figure 19A−C). The A-aGO/SA physical hydrogel was fabricated by adding Ca^{2+} ions to the A-aGO/SA solution. A-aGO played a role as a cocross-linking species to provide a hierarchically developed hydrogel structure. Rheological studies show that the A-a$GO_{0.2}$/$SA_{Ca\text{-}6}$ (where the subscripts indicate the weight percentages of A-aGO and $CaCl_2$, based on SA) hydrogel showed a shear-thinning property from 0.01 to 500 s^{-1} (Figure 19D). It was found that, at a fixed shear rate, A-a$GO_{0.2}$/$SA_{Ca\text{-}6}$ hydrogel showed higher viscosity than that of the control groups, $GO_{0.2}$/$SA_{Ca\text{-}6}$ and $SA_{Ca\text{-}6}$ hydrogels. This result reflects the obvious enhancement effect of A-aGO. In addition, the A-a$GO_{0.2}$/$SA_{Ca\text{-}6}$ hydrogel was more sensitive to oscillation strain. The G' value rapidly decreased when the strain increased to 3% and intersected with G'' at 23.5% (Figure 19E). This finding indicates that reversible dynamic absorption and desorption of SA chains from the A-aGO surface would impart the hydrogel with shear-thinning and excellent self-healing properties (rapid recovery of the gel structure). Under alternating oscillation strain, G' and G'' recovered to 92% and 80% of their initial values (Figure 19F), showing much better reversibility in the transition from gel to the quasi-liquid state than that of the $SA_{Ca\text{-}6}$ hydrogel. To evaluate the capability for bioprinting, the A-aGO/SA hydrogel could be further chemically cross-linked using UV-mediated polymerization in the presence of acrylamide (AAm) and *N*,*N*′-methylene bis-(acrylamide) (MBA), a cross-linker. The A-aGO/SA/PAAm nanocomposite hydrogel was fabricated into various 3D structures. Because the A-aGO/SA hydrogels have good printability based on their shear-thinning and self-healing properties suitable for 3D printing, the final UV-treated constructs had excellent structural resolution with good mechanical stability. For example, the A-a$GO_{0.2}$/$SA_{Ca\text{-}6}$/PAAm hydrogel could be printed to construct hollow pentagonal structures with a self-weight supporting ability (Figure 19G). In contrast, the identical structure constructed from $SA_{Ca\text{-}6}$/AAm and $GO_{0.2}$/$SAC_{a\text{-}6}$/AAm hydrogels showed low self-standing ability and quickly collapsed (Figure 19H,I). From a bioprinting point of view, the main idea of this work is the use of an approach to aminate GO in the presence of alginate before hydrogel formation. Using this chemistry, alginate was effectively adsorbed in situ on the surface of GO nanosheets through noncovalent interactions. This prevented A-aGO from agglomerating, thereby affording excellent colloidal stability in water, reflecting that A-aGO can be dispersed at the individual nanolevel in the aqueous phase. Hence, the separately dispersed A-aGO could establish a strong cohesion through the cocross-linking interactions between alginate and the A-aGO. The A-

https://dx.doi.org/10.1021/acs.chemrev.0c00015
Chem. Rev. 2020, 120, 10834−10886

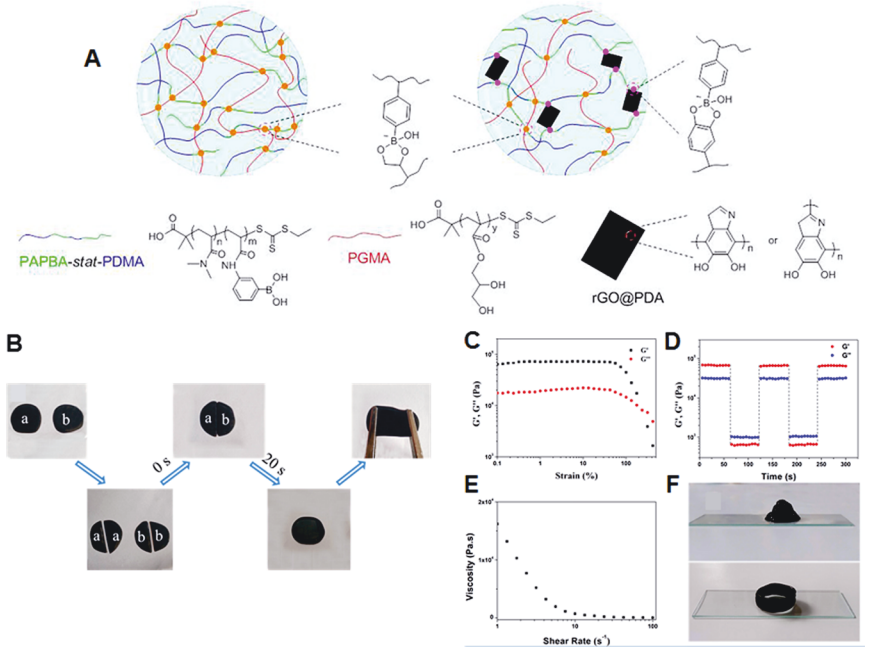

Figure 20. (A) Illustration of the synthesis of nanocomposite hydrogels. (B) Demonstration of the self-healing at room temperature. (C) Dependence of moduli on strain amplitude sweep (γ = 0.1−400%) at a fixed frequency of 1 rad/s. (D) Step-strain test at a fixed frequency of 1 rad/s (1% or 400% of strain). (E) Viscosity measurement at 1% of strain. (F) Printed cone and hollow cylinder 3D patterns. All these data were obtained using the hydrogel with the ration of PDMA-*stat*-PAPBA (wt %):PGMA (wt %):rGO@PDA (wt %):PBA/diol (molar ratio) as 5.00:2.50:0.50:1/2. Reproduced with permission from ref 335. Copyright 2019 American Chemical Society.

aGO could act as an efficient nano cross-linker for hydrogel formation and serve as a key modulating factor for the printability of A-aGO/SA gels. The rheological properties supported the significance of A-aGO/SA in controlling the printability for constructs with well-defined dimensions and morphologies. Considering the chemistry, if the degree of amination of the GO nanosheets can be controlled, the rheological and mechanical properties that determine the printability of the hydrogels may be more readily adjustable.

Khabibullin et al. reported on injectable nanofibrillar hydrogels formed by the combination of cellulose nanocrystals (CNCs) and graphene quantum dots (GQDs).[355] Amphiphilic rod-like CNCs (average length of 183 nm and diameter of 23 nm) were used as the main building block and had negatively charged surfaces due to the presence of half-ester sulfate groups (ζ-potential of −60 mV at pH 7.0).[356,357] Disk-shaped GQDs served as cross-linkers for 3D network formation with CNCs to prepare nanocomposite hydrogels. GQDs have an amphiphilic character because they exhibit hydrophobicity in their basal plane and hydrophilicity at the carboxylic acid group-containing edges.[358] The nanocomposite hydrogels were formed by simply adding GQDs into the aqueous dispersion of CNCs. When combining these two nanospecies, three types of noncovalent interactions are involved in network formation; (i) hydrogen bonding interactions between the hydroxyl groups on the CNCs and the carboxylic acid groups of GQDs, (ii) hydrophobic interactions between the hydrophobic faces of the CNCs and the GQD basal plane, and (iii) electrostatic repulsion between the half-ester sulfate groups of the CNCs and the carboxylic acid groups of GQDs. Considering the identical anionic nature of the two nanomaterials, it is interesting to observe physical gel formation. As a mechanism for hydrogel formation, it has been suggested that interspecies hydrogen bonding and hydrophobic interactions were more dominant and thus could overcome the electrostatic repulsive forces. Rheological data showed that, at >10% strain, the CNC-GQD nanofibrillar hydrogels exhibited a nonlinear viscoelastic behavior caused by the disruption of the physically cross-linked network.[359] The mechanical properties of the hydrogels could be controlled by adjusting the amount of either CNCs or GQDs. For example, at C_{CNC} = 50 mg/mL, the G' value for the gel was 266 Pa when C_{GQD} was 10 mg/mL. Meanwhile, at C_{GQD} = 5 mg/mL, G' was decreased by approximately 5-fold (54 Pa). This observation indicates that a higher concentration of GQD cross-linkers resulted in the formation of stronger networks. In addition, the higher the CNC content was, the stronger the hydrogels that were obtained. More importantly, the resulting CNC-GQD hydrogels exhibited shear-thinning behavior, which is desirable for extrusion-based 3D bioprinting applications. This viscosity-decreasing behavior under shear force was verified by observing the G' value under oscillation strain from 1 to 50% strain. For the hydrogel with G' = 80 Pa, the G' value decreased to 2 Pa upon decreasing the strain to 50% and dropped below the G'' value, reflecting gel liquification. The G' value recovered completely within 12 min at the end of each cycle. To evaluate the printability of the hydrogels, they were extruded from a syringe to form a threadlike shape with a predesigned pattern. Notably, the GQD-containing 3D hydrogel is attractive because it can exhibit photoluminescence properties. In addition, the extruded hydrogel exhibited birefringence, as visualized by polarized optical microscopy. This phenomenon is probably due to the shear-induced alignment of the CNCs during extrusion. It was suggested that the anisotropic structure of the hydrogels may mimic the anisotropic morphology of various tissues, such as cartilage and cornea, which is crucial for cell guidance, proliferation, and differentiation.

A GO-based supramolecular hydrogel can be formed by host−guest interactions between α-cyclodextrin (α-CD) and

https://dx.doi.org/10.1021/acs.chemrev.0c00015
Chem. Rev. 2020, 120, 10834−10886

PEG-functionalized GO nanosheets. Zhang et al. used pyrene-conjugated PEG (Py-PEG).[334] Py-PEG chains were tethered on both sides of GO surfaces through $\pi-\pi$ stacking interaction between GO and polyaromatic pyrene moieties of Py-PEG. The addition of α-CD into the Py-PEG-modified GO induced hydrogel formation through the formation of an inclusion complex of α-CD and PEG. This PEG/CD complexation generated a 3D network consisting of alternating layered structures of GO nanosheets and PEG/CD inclusion complexes. In this supramolecular assembly, the GO nanosheets acted as physical cross-linkers to provide the hydrogel with mechanical stability. The GO played a crucial role not only in promoting the formation of the supramolecular nanocomposite hydrogel but also in increasing the mechanical strength of the resulting hydrogel. The G' value of the GO-based hydrogel was more than 1000 Pa, and a higher G' value was observed with increasing amounts of α-CD. The $\pi-\pi$ stacking interaction between the GO cross-linkers and PEG/CD complex is a dynamic reversible interaction. Thus, the hydrogels showed shear-thinning, which is observed for many supramolecular hydrogels.[360−362]

Very recently, Huang et al. developed injectable self-healable nanocomposite hydrogels containing PDA-coated chemically reduced graphene oxide (rGO@PDA).[335] rGO@PDA of 3.3 nm thickness (with 2 nm of PDA coating) was fabricated by alkaline polymerization of dopamine on the rGO surface, and the surface of the resulting rGO@PDA contains functional catecholic diol groups. The PDA coating chemistry used in this work has been widely explored to produce novel nanomaterials with diverse surface functionalities.[363−368] It is known that the PDA coating layer has numerous catechol groups and possesses electrophilic *o*-quinones, which are further reactive toward both amine- and thiol-bearing species through Schiff base formation and/or Michael-type addition reactions.[369−372] In this work, the further chemical reaction of PDA coatings was not considered, and the catechol groups on the surface of rGO@PDA were used to form dynamic covalent networks with PBA-containing polymers in the hydrogel matrix. The nanocomposite hydrogel was fabricated by simple mixing of poly(*N*,*N*-dimethylacrylamide-*stat*-3-acrylamidophenylboronic acid) (PDMA-*stat*-PAPBA), poly(glycerol monomethacrylate) (PGMA), and rGO@PDA in an alkaline aqueous solution (pH ∼ 10). The cross-linked network formed in the hydrogel was based on boronic ester-based dynamic covalent bonds (Figure 20A). rGO@PDA was homogeneously dispersed within the hydrogel and acted as a cross-linker through boronic ester bond formation between the surface catecholic diols and PBA of PDMA-*stat*-PAPBA chains. Rheology analysis indicated that the incorporation of rGO@PDA endowed the nanocomposite hydrogels with improved mechanical strength, as evidenced by the significant increase in G' over that of the rGO@PDA-free hydrogel. Depending on the amount of rGO@PDA, the nanocomposite hydrogels exhibited G' values in the range of 40 000−60 000 Pa, which was 7−11-fold higher than those of the hydrogel without rGO@PDA. To estimate the self-healing property, the two pieces of separately prepared hydrogels (denoted as a and b) were allowed to come into contact for 20 s. An intimately merged hydrogel was formed without any boundary (Figure 20B), and the hydrogel behaved as one single and could be stretched without rupture at the interface where each hydrogel had initially come into contact. This self-healable ability could be ascribed to the reversible nature of boronic ester dynamic covalent bond-based networks. The self-healing behavior was also investigated by dynamic strain sweep (γ = 0.1% and 400%) at a fixed frequency (1 rad/s). Rheological studies showed that both G' and G'' showed a significant drop with increasing strain, and beyond ∼245% of strain, G'' became greater than G', indicating the complete destruction of the hydrogels (Figure 20C). The continuous step-strain sweeps showed that the G' value largely decreased from ∼68 000 Pa to ∼700 Pa at 400% of applied strain (Figure 20D). After the strain returned to 1.0%, G' and G'' were found to almost recover to their initial levels. This recoverability of hydrogels is typically observed in most dynamic hydrogels cross-linked with reversible interactions.[308,352] The rGO@PDA-incorporated hydrogel exhibits shear thinning behavior, making it applicable as a bioink for 3D bioprinting (Figure 20E). Figure 20F shows the successful printability of the hydrogel by demonstrating its good injectability and rapid recovery of sufficient mechanical fidelity to support the next printed layer. As described, the chemical approach using the boronic ester dynamic covalent bonds enabled dynamic interactions between rGO@PDA and the polymer network, resulting in the novel hydrogels with controllable self-healing and injectable capabilities for 3D bioprinting applications. The surface chemistry used for endowing GO with catechol functionalities appears to be very effective in generating this kind of dynamic hydrogel.

As an alternative type of chemistry that can install catechol groups on GO surfaces, poly(norepinephrine) (PNE) coating chemistry is recommended.[373,374] Norepinephrine (NE) is a small-molecule neurotransmitter possessing a catecholamine structure.[375] It is a dopamine analogue with an additional alkyl hydroxyl group.[376] PNE coatings are also formed through oxidative polymerization in alkaline solutions. A number of reports have demonstrated the advantages of PNE coating techniques over PDA coating, in terms of coating uniformity. Compared to that with PDA, the PNE coating provides a more uniform and well-defined nanolevel coating on the surfaces.[374,377,378] Hence, it is often recommended as a more preferable chemical approach for material surface coatings.[375,379,380] It is expected that the surface of the resulting PNE-coated nanomaterials may exhibit more reproducible and consistent characteristics in forming dynamic covalent bonds with the polymeric networks.

7.2. Metal Carbonate-Based Hydrogels

Biomineralization processes for fabrication of organic−inorganic composites have been explored to generate high-performance biofunctional nanoparticles and hydrogels.[381−386] As representative examples of biominerals, calcium carbonate ($CaCO_3$) and calcium phosphate (CaP), have been incorporated into various hydrogel matrices in either a nano/microparticle form or an in situ mineralized forms.[387−390] Although the incorporated biominerals effectively improve the mechanical properties, they usually exist as fillers and not as cross-linkers that can strongly hold the polymer networks. Thus, the gelling and rheological properties are mostly dependent on the matrix polymer itself.[391,392] For example, Huang et al. prepared PVA-based magnetic nanocomposite hydrogels containing nanohydroxyapatite (n-HA) and magnetic nanoparticles (Fe_2O_3).[391] Although n-HA improved the mechanical properties of the hydrogel, it did not present any effects in modulating the gelling properties, such as shapeability or injectability. This is because the network formation is due to tiny crystalline PVA regions formed by a repeated freeze−thaw process. Ren et al. reported on injectable and degradable polysaccharide-based hydrogels integrated with n-HA and $CaCO_3$ microspheres.[393] Likewise, the addition of n-HA and

https://dx.doi.org/10.1021/acs.chemrev.0c00015
Chem. Rev. 2020, 120, 10834−10886

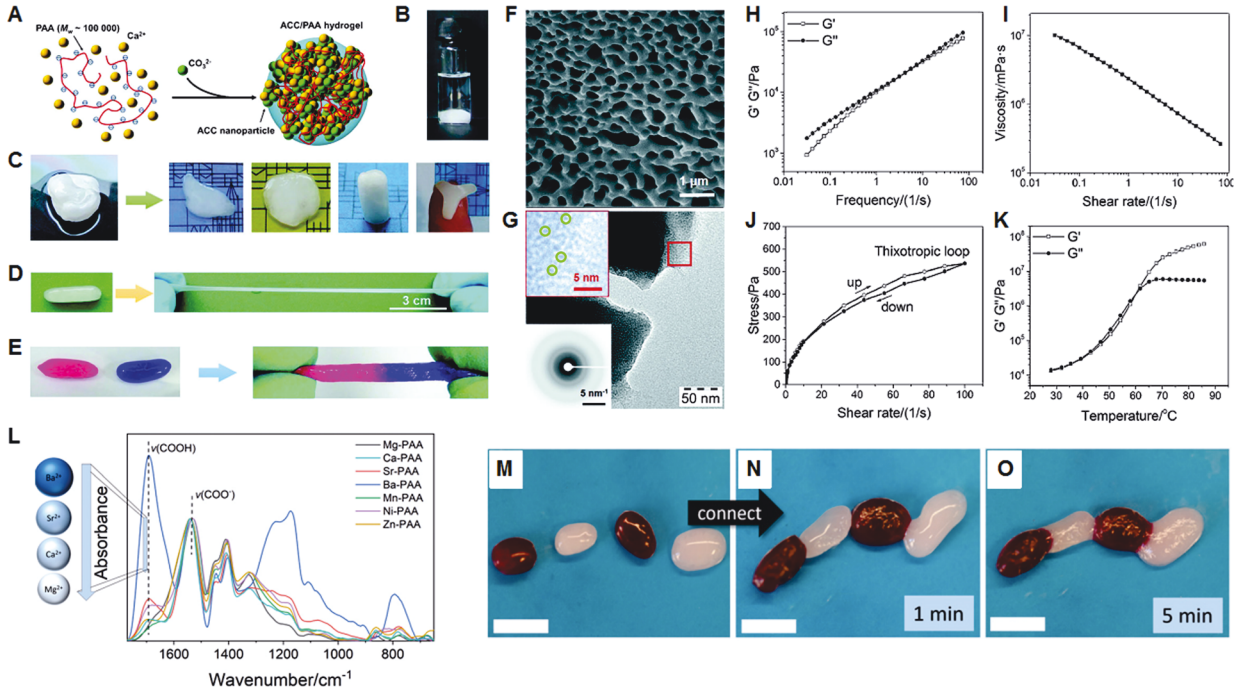

Figure 21. (A) Schematic synthesis of the ACC/PAA supramolecular hydrogel. (B) ACC/PAA hydrogel is stable in water. (C) ACC/PAA hydrogel is plastic, which can be made in different shapes. (D) ACC/PAA hydrogel is stretchable. (E) Self-adhesion of ACC/PAA hydrogel. Dye molecules (rhodamine B and methylene blue) were introduced to produce the colors. (F) SEM image of the freeze-dried ACC/PAA hydrogel. (G) TEM images of ACC/PAA dry gel. The insets are the corresponding electron diffraction pattern and an enlarged view of the area highlighted by the red square illustrating the presence of very small ACC nanoparticles (highlighted by green circles), (H–K) Rheological behavior of the ACC/PAA hydrogel. (H) Frequency dependencies of the storage (G') and loss (G'') moduli. (I) Viscosity as a function of shear rate. (J) Thixotropic loop measurement. (K) Temperature dependencies of the storage (G') and loss (G'') moduli. Reproduced with permission from ref 394. Copyright 2016 Wiley-VCH. (L) The ATR–FTIR spectra of all mineral plastics indicate the complexation between carboxylates and respective metal ions (around 1530 cm^{-1}) and the deprotonation degree of PAA (around 1700 cm^{-1}). (M) Separated $MnCO_3$/PAA hydrogels in the swollen state. The dark-red color results from the addition of Toluylene Red, and (N,O) upon connection, the gels heal themselves within minutes. Reproduced with permission from ref 397. Copyright 2018 The Royal Society of Chemistry.

$CaCO_3$ was not the main contributor in controlling the injectability of the hydrogel because the hydrogel was formed by network formation through the Schiff base reaction between amine-bearing carboxymethyl chitosan and aldehyde-functionalized oxidized alginate.

7.2.1. Calcium Carbonates. A well-defined ultrafine amorphous $CaCO_3$ (ACC)-incorporated nanocomposite hydrogel was constructed by simply mixing $CaCl_2$, Na_2CO_3, and PAA in an aqueous phase.[394,395] Very small ACC nanoparticles (~3 nm) were formed through in situ mineralization in the aqueous PAA solution. The main idea of this work is not the direct addition of ACC nanoparticles into PAA solution but rather the formation of ACC nanoparticles in the presence of PAA in water. The former approach may not provide effective interaction between the surface of ACC and PAA chains due to the limited dispersion of ACC in the PAA solution. Moreover, this simple mixing process results in the limited adsorption of PAA chains on ACC surfaces. For this reason, it is unlikely to expect strong PAA–ACC interspecies interactions. In contrast, the in situ formation of ACC was initiated by sequentially adding Ca^{2+} ions and CO_3^{2-} ions into PAA solution (Figure 21A). By this in situ mineralization route, the binding of PAA to ACC nanoparticles may occur in the following two possible ways: (i) Ca^{2+} ions bind to anionic carboxylic acid groups of PAA and then the ACC grows around the PAA chains, or (ii) ACC crystals are first formed and PAA chains are then incorporated onto the ACC surface. This mineralization behavior, in the presence of organic species, was reasonably supported by a previous report that described the in situ formation of thiol-functionalized hydroxyapatite nanoparticles.[396] This process provides a strong hybrid structure, in which the PAA chains are tightly incorporated into and/or onto the ACC nanoparticles. Thus, it is expected that the ACC nanoparticles can serve as excellent cross-linkers for PAA network formation. It is noted that PAA showed the chain-length-dependent gelling ability as well as concentration-dependent gelation behavior. If the length of PAA was too short (~2000 g/mol) or too long (~450 000 g/mol), the PAA chains cannot produce a gel structure and instead form weak precipitates in water. In contrast, for the PAA of ~100 000 g/mol, the hydrogel was stable and was not dispersed again in water (Figure 21B). This phenomenon is understood in that Ca^{2+} cross-links with PAA chains were dependent on the chain length of PAA. There may exist a critical point of the cross-links that hinders the redispersion of the formed hydrogels. Furthermore, the minimal concentration of PAA necessary to form a hydrogel was found to be approximately 0.08 M. The lower concentration resulted in precipitates of crystalline $CaCO_3$, which were formed through uncontrolled nucleation and growth. Hence, optimization of the length and concentration of PAA chains was key in fabricating the stable hydrogels. The ACC-cross-linked hydrogels were moldable into various shapes and stretchable into long fibers without any elastic recovery (Figure 21C,D). Interestingly, the hydrogel shows rapid self-healing behavior, when two separate hydrogels are linked together (Figure 21E). This behavior appears to be useful for the construction of multifunctional 3D constructs by linking

https://dx.doi.org/10.1021/acs.chemrev.0c00015
Chem. Rev. 2020, 120, 10834–10886

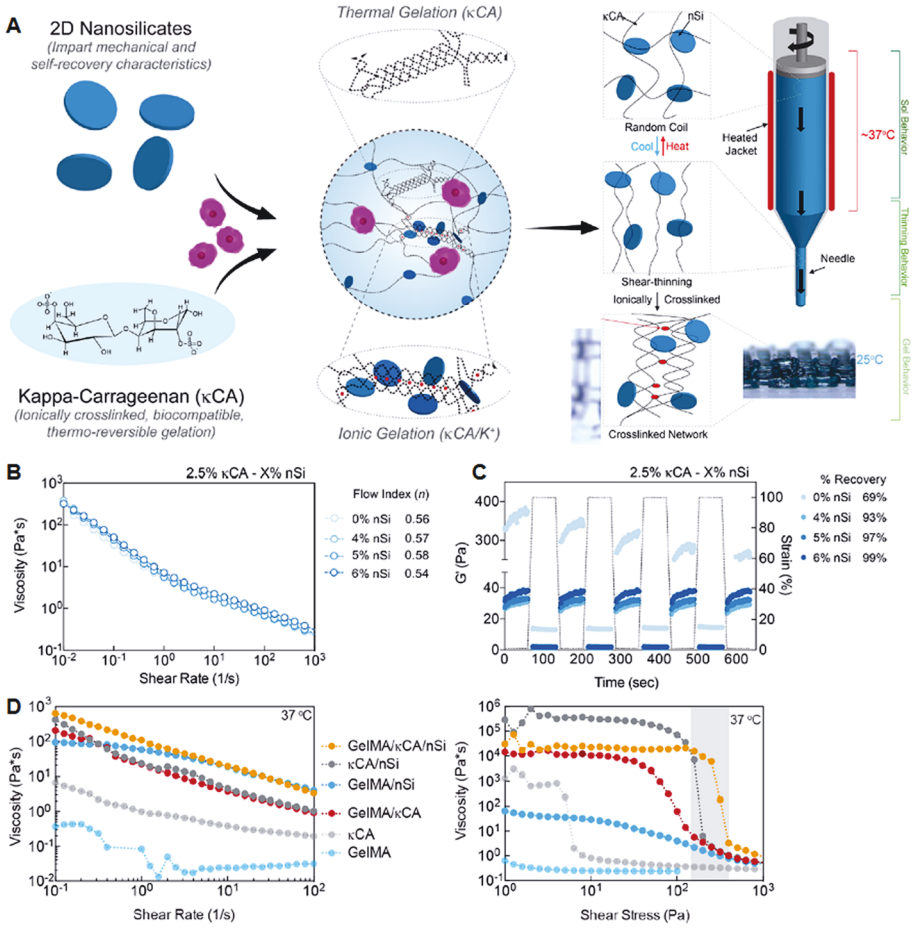

Figure 22. (A) Synthesis of thermoresponsive and shear thinning bioinks from nSi and κCA. Schematic showing the dual cross-linking process of thermoreversible gelation and ionic gelation of the κCA network. Nanosilicate-stabilized cross-linked network due to physical interactions with κCA and ions to improve the mechanical stability of 3D printed anatomical-size structures. κCA undergoes thermoreversible gelation upon heating and cooling, which results in the formation of double-helical structures that can then be ionically cross-linked with the introduction of K^+ ions to form a stable network. (B) Shear rate sweeps revealing the shear-thinning nature of κCA and κCA−nanosilicate bioinks. (C) Time sweep at 37 °C demonstrating percent recovery of bioink's storage modulus with the introduction of nSi. Reproduced with permission from ref 330. Copyright 2017 American Chemical Society. (D) The shear stress sweeps measure viscosity changes with increasing shear stress, allowing visual comparison of the yield regions of each bioink (NICE yield region shaded on graph). Shear rate sweeps illustrate the shear thinning characteristics of precross-linked gels. Reproduced with permission from ref 413. Copyright 2018 American Chemical Society.

several pieces of small hydrogel blocks with different biofunctions, such as cell-laden hydrogels (possibly different cell types) and growth factor-releasing hydrogels. ACC/PAA hydrogels were observed to have a typical hydrogel structure with porosity (Figure 21F). The TEM image shows the presence of ACC nanoparticles of 1.5−3 nm, which reflects the complex structure of ACC nanoparticles physically cross-linked with PAA (Figure 21G). The ACC/PAA hydrogels show the angular frequency-dependent viscoelastic behavior, which is normally observed for hydrogels with physical cross-links (Figure 21H). The hydrogel exhibits shear thinning behavior: with increasing shear rate, a reduction in viscosity is found (Figure 21I). Hysteresis of the shear rate sweep cycle indicates that the hydrogel is thixotropic (Figure 21J). These rheological properties provide the hydrogels with good injectability and shapeability. In a recent report, it was demonstrated that the ACC/PAA nanocomposite hydrogels had good injectability.[395] The temperature dependence indicates that G' becomes higher than G'' with increasing temperature, reflecting the formation of harder gels due to the more dynamic interaction of PAA chains on ACC nanoparticles (Figure 21K).

7.2.2. Other Alkaline Earth Metal and Transition Metal Carbonates. The PAA-based shapeable and injectable nanocomposite hydrogels could also be fabricated from the substitution of Ca^{2+} by other alkaline earth and transition metal ions (Mg^{2+}, Sr^{2+}, Ba^{2+}, Mn^{2+}, Ni^{2+}, and Zn^{2+}).[397] For hydrogel formation, it was critical to control the amount of added metal ions and the deprotonation degree of the carboxylic acid groups of PAA. ATR-FTIR analyses revealed the formation of M^{2+}-COO^- complexes upon the addition of Na_2CO_3, except for $BaCO_3$/PAA hydrogels (Figure 21L). Rheological analyses of the swollen hydrogels indicate that these metal carbonate/PAA nanocomposite hydrogels exhibited behavior analogous to that of the already reported ACC/PAA hydrogels.[394] All these physical hydrogels show viscoelastic behavior dependent on the angular frequency. All the metal carbonate/PAA hydrogels exhibited high G' and G'' values (10^3−10^5 Pa). Notably, the hydrogels exhibit shear thinning behavior. This work showed that G' and G'' values and viscosity of the hydrogels could be modulated by the choice of metal ions. These adjustable mechanical and rheological characteristics of metal carbonate/PAA hydrogels may find diverse applicability with optimized

https://dx.doi.org/10.1021/acs.chemrev.0c00015
Chem. Rev. 2020, 120, 10834−10886

printability for 3D bioprinting. In addition, similar to the ACC/PAA hydrogel, the diverse classes of metal carbonate/PAA hydrogels ($SrCO_3$/PAA, $NiCO_3$/PAA, $MnCO_3$/PAA, and $ZnCO_3$/PAA) exhibited pastelike plasticity and rapid self-healing in the swollen state. For example, $MnCO_3$/PAA hydrogels exhibited the excellent self-healing ability within minutes, which was ascribed to the dynamic physical cross-linking of the PAA chains (Figure 21M−O). Although these current studies are only based on PAA, there are many choices of COOH-containing biopolymers (poly-COOH), including hyaluronic acid, alginic acid, and carboxyl methylcellulose. Therefore, it is worth developing diverse classes of metal carbonate/poly-COOH systems in an attempt to find useful bioinks with tailored printability for the construction of specific 3D tissue constructs.

7.3. Nanoclay and Silica-Based Hydrogels

Nanoclays or silica-based nanoparticles have been broadly used as reinforcements for polymeric composites to improve mechanical, thermal, and anticorrosion properties. This section presents the current update on developing nanoclay or silica nanoparticle-reinforced hydrogel systems for biomedical applications.

7.3.1. Laponites. Laponite nanosilicates ($Na_{0.7}Si_8Mg_{5.5}Li_{0.3}O_{20}(OH)_4$) are synthetic clays that have similar compositions of bioactive glasses and have a nanodisk-shape with an average diameter of 25 nm and a thickness of 1 nm.[398−400] One feature that distinguishes Laponites from natural clays is their excellent uniform dispersibility in the aqueous phase.[401] Laponites have surfaces and edges that are negatively and positively charged, respectively. Because of their ionic properties, these clays are preferentially exfoliated at low concentrations (∼1.5 wt %), whereas at high concentrations (∼3 wt %), they form a "house of cards" structure due to interplatelet edge-to-face ionic interactions.[402,403] Over the past decade, a vast number of Laponite-based hybrid materials have been developed, and the role of Laponite in the nanocomposites have been addressed by several excellent review papers.[404,405] In particular, Laponites are employed as a major colloidal filler for tissue-forming scaffolds in the field of regenerative medicine because they not only can reinforce the scaffolds but can also provide bioactivity for osteogenic differentiation of human mesenchymal stem cells (hMSCs).[406−408] With respect to 3D bioprinting, Laponites have played a pivotal role in modulating the rheological and mechanical properties of many classes of polymer hydrogels. They can modulate these properties by acting as cross-linkers that can form 3D networks with the matrix polymer chains.[400,409,410] In this section, we highlight the recent use of Laponites as cross-linking species to control the rheological and mechanical characteristics of Laponite-based nanocomposite hydrogels. Wilson et al. reported on a new class of the nanocomposite bioink consisting of κ-carrageenan (κCA) and 2D Laponite nanosilicates (nSi, Laponite XLS).[330] They focused on the role of nSi in improving the self-healing property and mechanical stiffness of the hydrogels. The nSi used in this work had a negatively charged surface, where the positive charge on its surface was shielded using inorganic phosphate. The κCA/nSi nanocomposite hydrogels are fabricated mainly based on thermal gelation and subsequent ionic gelation, representing the inherent gelling behavior of κCA. The main role of nSi as an additional cross-linker was suggested through the formation of hydrogen bonds between the nSi surface and the OH groups of κCA.[411] The heated mixed solution of κCA/nSi was cooled to induce hydrogel formation, which occurs due to the formation of double helices through hydrogen bonding between galactose units of κCA. The subsequent addition of K^+ ions induces additional interactions with the κCA chains, thereby further stabilizing the thermo-gelling hydrogels. Although the κCA thermoreversible hydrogel is known to exhibit shear-thinning property, it lacks desirable printability for 3D printing due to its poor self-healing properties and low mechanical strength. These weaknesses may result in final 3D constructs with low shape fidelity and self-standing ability. Thus, the main purpose of this work is to overcome these drawbacks by incorporating nSi into the κCA hydrogel matrix. Figure 22A shows a three-step route in which κCA/nSi nanocomposite hydrogels are subjected to 3D printing. The random coils of κCA at 37 °C are converted to the shear-aligned structure, which induces shear thinning behavior and finally is ionically stabilized to form stable hydrogels. Figure 22B shows that both κCA and κCA/nSi exhibit similar shear thinning behavior, as indicated by the power-law flow index (n) numbers of 0.56, 0.57, 0.58, and 0.54 for various amounts of nSi. The flow index (n) is a parameter of the power-law equation ($\eta = K\dot{\gamma}(n-1)$) (where η is viscosity, K is the consistency index, $\dot{\gamma}$ is the shear rate, and n is the flow index (shear thinning index)) and describes the rheological behavior of liquids, such as non-Newtonian (shear thinning and shear thickening) and Newtonian behaviors. A flow index (n) of $n < 1$ is indicative of materials with the shear-thinning property.[412] The almost identical viscosity decrease under shear force indicated a negligible effect of nSi on the shear-thinning ability of κCA, indicating that nSi did not interfere with the ability of κCA polymer junction to undergo for shear-induced alignments. Next, the effect of nSi on the recovery of hydrogel structure after the removal of shear stress was examined by subjecting the hydrogel precursor solutions to alternating low (1%) and high (100%) strain conditions. κCA presented a low percent recovery of G' (69%), while nSi-incorporated hydrogels exhibit a higher percent recovery range of 93−99%, depending on the nSi content (Figure 22C). Importantly, it was found that nSi addition afforded a faster recovery (below approximately 5 s) after cessation of shear stress. This observation indicates that nSi greatly improved the self-healing ability of the hydrogels due to the reversible dynamic interaction between nSi and κCA, which was due to the OH groups of κCA interacting with the surface of nSi. The researchers demonstrated the ability of the κCA/nSi bioink to print diverse complex constructs with high shape fidelity. The printed structure has high shape retention, even under the loading of many successive layers (∼30 layers). This excellent processability may not require additional stabilization steps, such as the postchemical cross-linking process. Overall, the presence of nSi enabled κCA/nSi to form self-supporting anatomical size constructs, which can be achieved by the rapid self-healing property and high stiffness of these nanocomposite hydrogels. Recently, the same research group reported on a nanoengineered ionic−covalent entanglement (NICE) bioink for the fabrication of mechanically stiff and elastomeric 3D structures.[413] The main component of this system was a gelatin methacrylate/κCA (GelMA/κCA) ICE network, which was reinforced by the incorporation of nSi having both of negatively charged faces and positively charged edges. In contrast to the use of nSi with only negative charges, the reversible interaction between doubly charged nSi and the charged polymer backbone allowed controllable shear thinning behavior (Figure 22D). In this work, a Herschel−Bulkley computational model was employed to simulate the behavior of the hydrogel bioinks

https://dx.doi.org/10.1021/acs.chemrev.0c00015
Chem. Rev. 2020, 120, 10834−10886

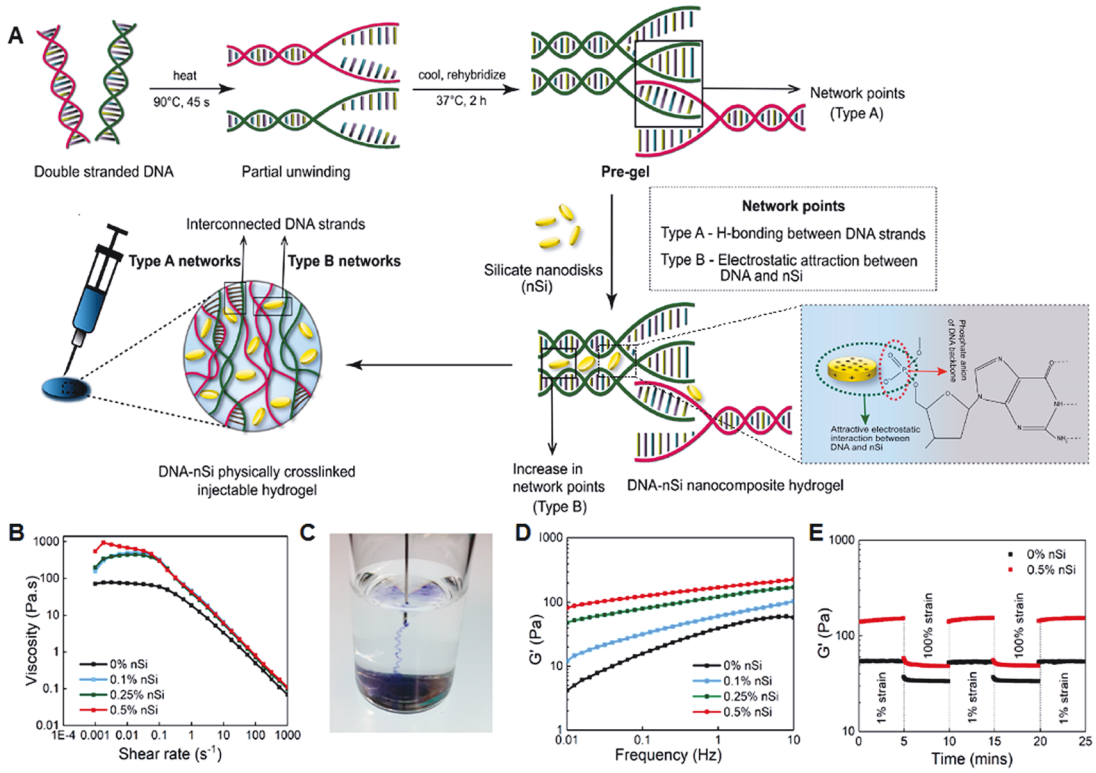

Figure 23. (A) Schematic representation of the design strategy for the development of multifunctional nanocomposite hydrogels. DNA−nSi injectable hydrogels are formed via a two-step gelation method. The first step consists of an intermediate weak gel (pregel) formation by heating and subsequent cooling of double-stranded DNA. The denaturation of double-stranded DNA followed by rehybridization in a random fashion facilitates the development of interconnections between adjacent DNA strands (type A network points) via complementary base pairing. Introduction of nSi in the second step of the gelation process increases the number of network points (type B) via electrostatic interaction with the DNA backbone, resulting in a shear-thinning injectable hydrogel. (B) Viscosity vs shear rate plots illustrate an increase in the viscosity due to the presence of nSi. All of the formulations display the typical shearthinning behavior with a reduction in the viscosity as the shear rate increases. (C) Image showing the injection of the blue-colored hydrogel through a 22 G needle. (D) Frequency sweep experiments performed in the range of 0.01 to10 Hz indicate an increase in storage modulus as the concentration of nSi was increased. (E) Recovery data obtained by monitoring the storage modulus of the nanocomposite hydrogels while subjecting them to alternating high (100%) and low (1%) strain conditions. Both 0% nSi (i.e., DNA gel without nSi) and 0.5% nSi (i.e., DNA gel with 0.5% nSi) exhibited more than 95% recovery. Reproduced with permission from ref 15. Copyright 2018 American Chemical Society.

and predict the cell stress during bioprinting by incorporating rheological data including shear thinning characteristics. The simulation study indicated that nSi and κCA exhibited synergy in increasing the shear thinning and yield stress in the NICE bioinks. The NICE bioink has promising potential due to the combination of superior printability, improved mechanical properties, and excellent bioactivity.

Basu et al. designed silicate nanodisk (nSi, Laponite XLG)-incorporated DNA-based nanocomposite hydrogels that show shear-thinning and rapid self-healing properties.[15] The DNA−nSi nanocomposite hydrogel was prepared following a two-step fabrication process (Figure 23A). First, DNA (4 w/v%) with a double-helix structure was denatured by heating at 90 °C and the sequential cooling to 37 °C resulted in randomly rehybridized DNA networks (type A network) through the formation of multiple hydrogen-bonding interactions between complementary base pairs of neighboring DNA strands. This heating and cooling process produced an intermediate weak pregel. Second, the addition of nSi into the pregel produces another physical network (type B network), which is formed through electrostatic interactions between the positively charged edges of nSi and the negatively charged phosphate groups of DNA. This anisotropically charged, two-dimensional, ultrathin structure with a high surface-to-volume ratio facilitated physically cross-linked networks for type B network points.[414−416] The specific electrostatic interaction between nSi and DNA was thoroughly investigated using X-ray photoelectron spectroscopy (XPS) analysis. The additional type B network formed by the nSi−DNA interaction provided the hydrogel with shear-thinning property and injectability (Figure 23B,C). The rheological property is a crucial requisite for injectable hydrogels, for which the viscosity decreases with increasing shear rate.[417] Noticeably, nSi−DNA interactions modulated the elasticity of the nanocomposite hydrogel, and an increase in storage modulus values was found in the hydrogels containing a larger amount of nSi (Figure 23D). In addition, the yield stress increased from 29.45 ± 3.75 to 73.98 ± 9.42 Pa as the nSi concentration increased from 0 to 0.5%, respectively. Because of this improved reinforcement, the nanocomposite hydrogel could retain its shape in comparison to that of the starting DNA solution. To evaluate whether the nSi−DNA nanocomposite hydrogels could exhibit rapid recovery after the removal of shear stress, oscillatory strain amplitude studies were performed. The result showed that the G' value was completely recovered within seconds, and this behavior was observed for the formulations both with and without nSi (Figure 23E). However, the nanocomposite hydrogels incorporating nSi have a higher value of G'. Taken together, the nSi-reinforced DNA hydrogels show potential as a new type of bioink with desirable printability for 3D bioprinting. The strength of using DNA as the main

https://dx.doi.org/10.1021/acs.chemrev.0c00015
Chem. Rev. 2020, 120, 10834−10886

building block for injectable nanocomposite hydrogel fabrications may lie in the many unique properties of DNA, including high molecular weight, numerous negatively charged phosphate groups, and highly specific base-pair interactions.

Liu et al. developed moldable self-healing nanocomposite hydrogels based on dopamine-modified PEG and Laponite nanosilicates.[418] The multiarm PEG conjugated with dopamine moieties (PEG-D8) could form 3D networks with Laponite (Figure 24A), which were constructed through interfacial

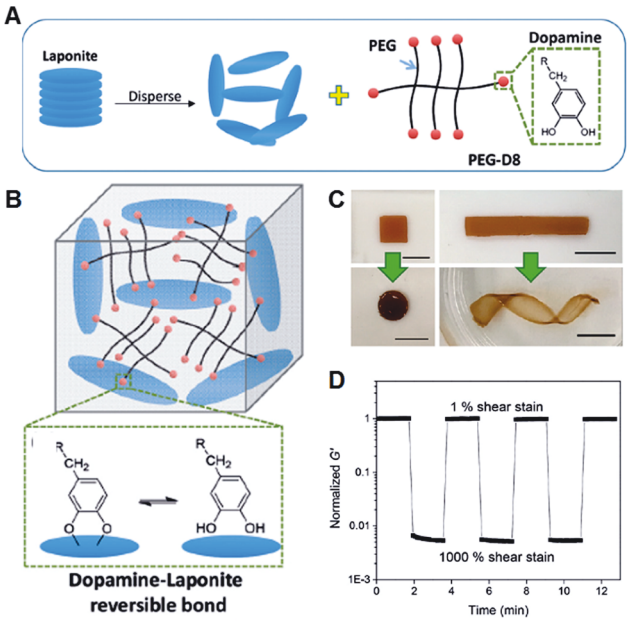

Figure 24. (A) Laponite was combined with PEG-D to prepare the adhesive hydrogel. (B) the hydrogel consists of a reversible interaction formed between dopamine and Laponite. (C) The hydrogel is remolded to different shapes (F; scale bars: 10 mm). (D) Normalized G' values of D8−15/Lapo-5 (incubated for 1 day) subjected to repeated cycles of 1 and 1000% shear strain with 10 s resting time in between. Reproduced with permission from ref 418. Copyright 2017 Wiley-VCH.

interactions between Laponite and catechol units of dopamines in PEG-D8 (Figure 24B). The dopamine−Laponite interaction was known to be reversible and thus has been used for various nanocomposite hydrogels.[419,420] Because of the dynamic property of the cross-linked networks, the hydrogels could be molded into diverse shapes (Figure 24C). When the oscillatory shear strain was applied, the hydrogel exhibited re-establishment of its network through strong catechol−Laponite interactions, indicating good self-healing properties (Figure 24D). The dopamine of the Laponite/PEG-D8 hydrogels underwent the time-dependent auto-oxidation to dopamine quinone and formed permanent covalent cross-links through the dimerization of dopamine units.[421,422] This spontaneous chemical cross-linking resulted in increased stiffness of the hydrogels, as estimated by the increased G' value. The incubation time for saturated chemical cross-linking was approximately four days, indicating that the formation of chemical networks was very slow. If the rate of oxidation-induced chemical cross-linking is controllable, this class of hydrogels may have potential as bioinks due to their injectability, self-healing properties, and mechanical stability after printing.

PEG and PEG derivatives are also used for the formation of hydrogel matrices of which rheological and mechanical properties can be modulated by incorporating Laponite nanosheets. Peak et al. fabricated injectable PEG/Laponite nanocomposite hydrogels.[423] The addition of Laponite as a cross-linker reinforced the PEG network and increased the viscosity and storage modulus of the hydrogels. When Laponite (2−8 w/v%) was added to the PEG solution (10 w/v %), the mixture exhibited shear thinning properties. This viscosity decrease with increasing shear rate was supported by estimating the shear thinning index (n). PEG showed almost Newtonian behavior ($n = 0.96$), whereas the PEG/Laponite nanocomposite hydrogels had n values of 0.22−0.29, indicating that Laponite induced shear thinning behavior. Nojoomi et al. developed Laponite-incorporated PEG-*co*-pyromellitic dianhydride (PEG-*co*-PMDA) copolymer-based injectable nanocomposite hydrogels.[337] The addition of Laponite into the copolymer hydrogel precursor changed the rheological behavior from Newtonian to thixotropic. The physical interaction between the Laponite surface and PEG-*co*-PMDA restricted the mobility of the polymer chains. In addition, matrix-assisted oppositely charged edge-to-face inter-Laponite interactions formed a "house of cards" structure at low shear rates and consequently increase the viscosity of the nanocomposites.[424,425] Under shear force, the Laponite platelets may align with the applied stress increasing the mobility of the polymer chains, and finally decreasing the viscosity with increasing shear rate. The Carreau−Yasuda model predicted the shear-thinning properties of the nanocomposite hydrogel precursor. This precursor could be chemically cross-linked through the reaction of dianhydrides of PMDA with diamine cross-linkers. This posttreatment step could provide the nanocomposite hydrogel with increased mechanical stability.

7.3.2. Silica Nanoparticles. Like Laponite nanoclays, silica nanoparticles are also good candidates that modulate the rheological properties of nanocomposite hydrogels. The silanol groups (−Si-OH) of silica surfaces can be readily modified with alkoxide-containing reactive compounds, such as aminopropyl triethoxysilane (APTES).[426,427] Further modification with diverse polymers is also feasible to provide additional functionality.[428,429] The rheological and mechanical properties of silica nanoparticle-containing hydrogels have been adjusted by physical interactions, including host−guest[430] and electrostatic interactions.[431] Lee et al. incorporated sub-100 nm cationic silica nanoparticles (SiNPs) in an anionic alginate/gellan (Alg/gellan) polymer mixture to produce nanocomposite hydrogels with improved mechanical stiffness, printability, and printing fidelity.[431] The addition of aminated SiNPs (AmNPs) (6 wt %) into the Alg/gellan mixture resulted in significantly enhanced shear thinning with much higher zero shear viscosity (2930 Pa s, 1062% increase) than that of the Alg/gellan inks (252 Pa·s). This behavior was due to the electrostatic interactions between the positively charged surfaces of AmNPs and negatively charged Alg/gellan. The mechanical properties could be modulated by the concentration and surface chemistry of the nanoparticles as well as the length of the anionic polymer chains. The major effect expected from the addition of AmNPs is the suppression of swelling of the printed constructs compared with the inks without AmNPs. This role of AmNPs may result in the high printing fidelity of the final 3D structures. Oscillatory strain amplitude studies showed that Alg/gellan inks, irrespective of the presence of AmNPs, exhibited rapid shear recovery behaviors. The presence of AmNPs increased the storage modulus (G' at 1 rad/s) by 486% compared with that without AmNPs. The increased G' vaue was attributed to AmNP-mediated physical cross-linking. Compared to Alg/

https://dx.doi.org/10.1021/acs.chemrev.0c00015
Chem. Rev. 2020, 120, 10834−10886

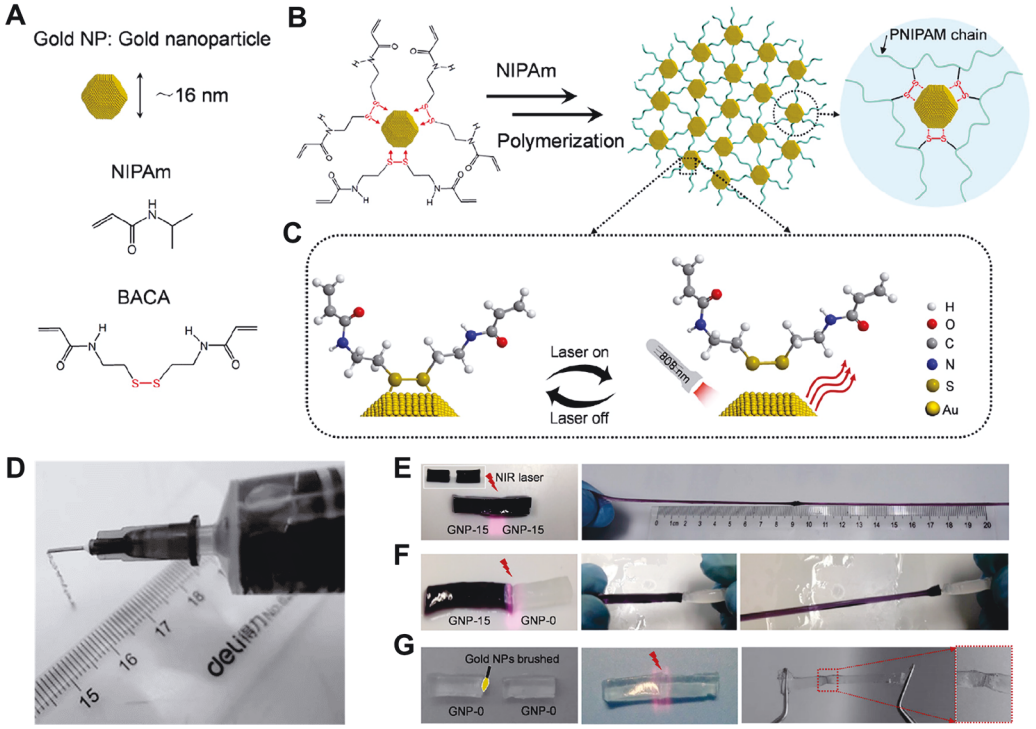

Figure 25. (A) Structure of gold NPs and a list of comonomers used for polymerization of hydrogels (NIPAM, *N*-isopropylacrylamide; and BACA, *N*,*N*-bis(acryloyl)cystamine (BACA)). (B) Formation of GNP hydrogel with modified gold NPs as large cross-linker in the in situ free-radical polymerization. (C) Mechanism for dynamic and reversible RS-Au bonding with NIR laser irradiation (808 nm). (D) Optical image of the hydrogel injected using a syringe with a 20 G needle. (E) Self-healing procedure between two separated GNP-15 hydrogel pieces (with a gold NP concentration of 750 ppm) under an NIR laser. (F) Self-healing process between GNP-15 and GNP-0 hydrogel pieces under an NIR laser. (G) Self-healing process between GNP-0 hydrogel pieces with the aid of gold NPs under an NIR laser. Reproduced with permission from ref 440. Copyright 2017 Cell Press.

gellan inks lacking AmNPs, Alg/gellan containing AmNPs could be printed without any collapse. In addition, AmNPs efficiently suppressed the swelling and shrinking of printed constructs, which was ascribed to the decreased hydrophilicity and highly cross-linked network of the AmNP-incorporated hydrogels. Serres-Gómez et al. reported on nanocomposite hydrogels formed through α-CD threading on PEGylated silica nanoparticles (~50 nm), which was prepared by the reaction of thiolated silica nanoparticles with maleimide-functionalized methoxy PEG (Mw: 750 or 5000 g/mol).[432] The supramolecular hydrogel was formed at relatively high CD (6−10 wt %) and PEG (6−12 wt %) concentrations. The threaded α-CDs on silica surfaces acted as physical cross-links to form dynamic 3D networks, which were formed by the aggregation of CD/PEG inclusion complexes. Rheology studies showed a solid-like behavior of the hydrogels, with a G' value of up to 25 kPa, which was higher by 1 order of magnitude than that of the hydrogel prepared without the silica nanoparticles. This shows a good example of the host−guest complexation approach that can develop diverse dynamic hydrogels. Various surface chemistries may generate useful dynamic hydrogels by allowing CD or CB[n]-based host−guest events on the surface of many classes of nanoparticles, irrespective of their surface elements or dimensions. Although most current studies of silica-based nanocomposite hydrogels have focused on nonporous solid silica nanoparticles, mesoporous silica nanoparticles need to be considered as alternatives for not only modulating the rheological properties of hydrogels but also releasing bioactive molecules.

7.4. Metal-Based Hydrogels

Gold nanoparticles (GNPs) and silver nanoparticles (AgNPs) have been employed as main building materials for the generation of a variety of nanocomposite hydrogels with diverse functionalities. GNPs and AgNPs are incorporated into the hydrogel network not only to simply provide the inherent property of each nanoparticle, such as photothermal activity[433,434] or antibacterial property,[339,435,436] respectively, but also to mainly control the rheological or mechanical properties by participating as cross-linkers in the hydrogel matrix.[338,340,437−439] In this review, we focus on recent studies of the latter cases, which are relevant to the printability of the hydrogels.

7.4.1. Gold Nanoparticles. Qin et al. designed gold nanoparticle (GNP)-incorporated near-infrared (NIR)-responsive self-healing nanocomposite hydrogels.[440] For hydrogel fabrication, the surface of the GNPs was first functionalized with acrylamide groups through the formation of dynamic RS−Au coordination bonds (Figure 25A). Then, the aqueous free radical polymerization of *N*-isopropylacrylamide (NIPAM) in the presence of acrylamide-modified GNPs produced nanocomposite hydrogels (GNP/PNIPAM), in which the GNPs act as large cross-linkers to tightly hold the PNPAM chains in the 3D networks (Figure 25B). Combined with the photothermal activity of GNPs,[441−444] this nanocomposite hydrogel employed the dynamic reversible RS−Au coordination interaction as a self-healing motif.[445−447] The photothermal property of GNPs triggered by NIR irradiation allows the RS−Au coordination bonds to be reversibly switched on and off (Figure 25C). Under NIR irradiation, this coordination interaction was disrupted, whereas it was reformed upon cessation of irradiation. As

https://dx.doi.org/10.1021/acs.chemrev.0c00015
Chem. Rev. 2020, 120, 10834−10886

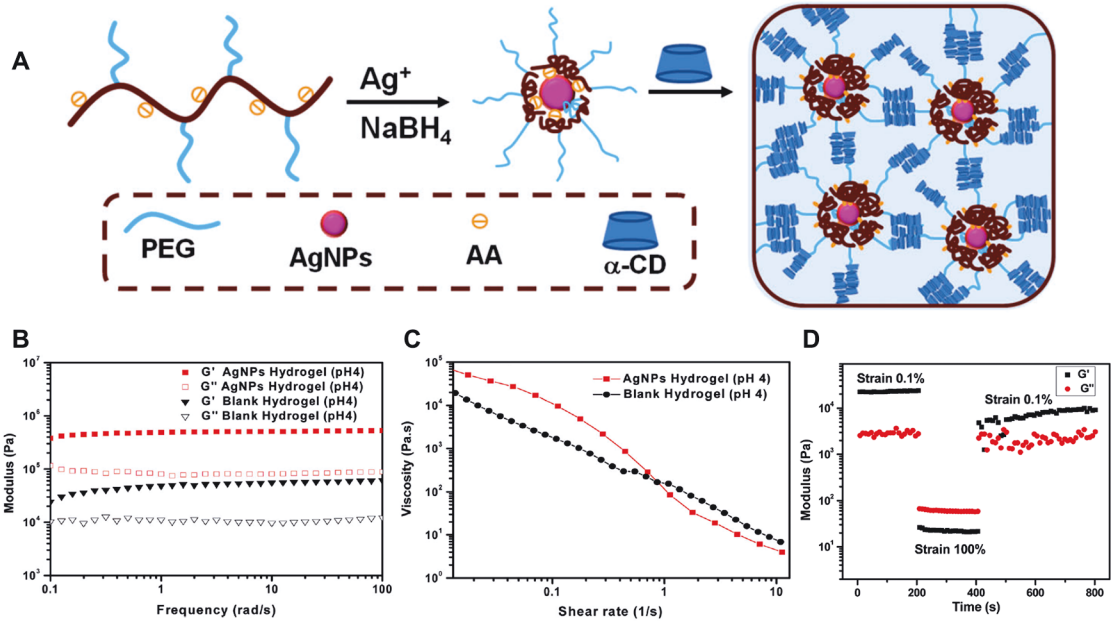

Figure 26. (A) Schematic for the preparation of AgNP hybrid supramolecular hydrogels. (B) Dynamic frequency sweep and (C) shear-thinning behaviors of the Gel-0 (formed at pH 4) and AGel-1 (formed at pH 4). (D) Dynamic step-strain rheological test results of the AgNP hybrid AGel-2 (formed at pH 7). Reproduced with permission from ref 338. Copyright 2018 The Royal Society of Chemistry.

expected, in the "Laser ON" state, the nanocomposite hydrogels may lose the cross-linking interactions between the GNPs and polymer matrix, resulting in soft materials that are moldable or injectable under shear force. More importantly, in the "Laser off" state, the cross-links are rapidly recovered from the hydrogel of the original state. The NIR-treated GNP/PNIPAM hydrogels could be injected using a syringe, indicating that the photothermal effect disrupted the RS-Au coordination interactions (Figure 25D). When the NIR laser irradiated the hydrogels, the temperature of the sample increased rapidly to almost 50 °C in the initial 2 min. This thermal responsiveness disrupted the cross-linked networks, endowing the hydrogel with injectability. The GNP/PNAIPAM-based hydrogel system exhibited the excellent NIR-induced self-healing properties. Under NIR irradiation, the two pieces of GNP-incorporated hydrogels (GNP-15) in close contact became fused into one piece, presenting good stretchability (Figure 25E). This healing ability is well supported by the schematic illustration in Figure 21H, which shows the dynamic reconstruction of RS−Au interactions at the interface of two separate hydrogels. In addition, when two individual pieces of GNP-15 and GNP-0 (without GNP) were brought together, rapid self-healing was observed in a few minutes (Figure 25F). Interestingly, GNPs could act as an adhesive species for two separate pieces of GNP-free hydrogels (Figure 25G). The fractured surface of one piece was first brushed with GNPs to form a thin GNP layer, and this piece was placed in contact with fresh hydrogel (GNP-0). Under NIR irradiation at the interface, each piece of the hydrogel was reconnected in a few minutes to establish the good tensile properties. The healed GNP-15 hydrogels exhibited a stress−strain curve nearly identical to that of the initially prepared sample, indicating the excellent recovered extensibility. Interestingly, the mechanical properties of the healed hydrogels were retained with a healing efficiency of 90%, even after 10 cycles of the healing process. The NIR-triggered dynamic RS−Au interactions are key to the excellent maintenance of these mechanical characteristics. To optimize the printability for bioprinting applications, further detailed studies on NIR-controlled rheological behaviors are needed. Overall, the dynamic coordinated self-healing mechanism described in this work may produce a robust injectable nanocomposite hydrogel with high impact in the field of 3D printing because it is possible to assemble a geometrically complex 3D structure by simply contacting of many pieces of the same and/or different classes of printed hydrogels with diverse shapes and dimensions, various biochemical and biological properties, and different mechanical characteristics.

Niu et al. reported on injectable supramolecular α-CD/PEG polypseudorotaxane-based hydrogels hybridized with GNPs.[340] The cross-linked 3D networks of these hydrogels were based on CD-based host−guest polypseudorotaxane motifs. For GNP-incorporated hydrogels, PEGylated GNPs (mean diameter = 8 nm) were first prepared by reducing anionic $HAuCl_4$ in the aqueous solution of positively charged poly(poly(ethylene glycol) methyl ether acrylate)-grafted poly(2-(dimethylamino)-ethyl methacrylate) copolymers (PPEGMA-*co*-PDMAEMA). GNP hybrid supramolecular hydrogels were then fabricated by simply mixing α-CDs with PPEGMA-*co*-PDMAEMA in water. The α-CDs formed inclusion complexes with PEG on the GNP surfaces, and the PEG/CD threaded complexes formed the physical network. It was reported that polypseudorotaxanes generated by threading α-CDs onto PEG preferentially formed aggregates, which served as physical cross-links to form hydrogels.[334,448] In addition, GNPs act as cross-linkers to physically hold the CD aggregate networks together. Frequency sweep and dynamic step-strain rheological tests showed that the nanocomposite hydrogels exhibited both typical thixotropic behavior and excellent self-healing properties.

7.4.2. Silver Nanoparticles. AgNPs have also been diversely used as cross-linking materials to produce various dynamic hydrogels exhibiting self-healing or shear-thinning characteristics.[52,338,449,450] Niu et al. developed dynamic α-CD/PEG polypseudorotaxane-based hydrogels incorporated with silver nanoparticles.[338] The cross-linking of these hydrogels was

https://dx.doi.org/10.1021/acs.chemrev.0c00015
Chem. Rev. 2020, 120, 10834−10886

based on CD-based host−guest interactions. For injectable AgNP composite hydrogels, PEGylated AgNPs were prepared by ionic complexation of $AgNO_3$ with the random copolymer of PEG methyl ether methacrylate (PEGMA) and PAA via electrostatic interactions, followed by in situ reduction (Figure 26A).

The AgNPs decorated with surface PEG chains had a mean diameter of 4 nm. The AgNP hybrid supramolecular hydrogels were then fabricated through host−guest inclusion interactions between PEG chains on AgNPs and α-CDs in the aqueous solution (Figure 26A). As described for GNP-based supramolecular hydrogels, these AgNP cross-linked hydrogels were physically cross-linked by both polypseudorotaxane structures and AgNPs. In addition, the synergistic effect of polypseudorotaxane and AgNP cross-links induces the formation of nanocomposite hydrogels from pH 4 to 9. For both Gel-0 and AGel-1, the G' value was higher than the corresponding G'' value and the moduli remained constant with increasing frequency in the detected region, indicating the quasi-solid state of these nanocomposite hydrogels (Figure 26B). Furthermore, the G' value of AGel-1 was 500 kPa, 10-fold higher than that of Gel-0, which was ascribed to the additional cross-linking generated by the PEGylated AgNPs. Notably, the hydrogel with AgNPs (AGel-1, 0.14 wt %) showed 4-fold higher viscosity than that of the hydrogel without AgNPs (Gel-0). This result reflects the higher cross-linking density in the presence of AgNPs compared to that of the hydrogel with only polypseudorotaxane cross-links. The viscosity of the Gel-0 and AGel-1 hydrogels decreased with increasing shear rate, indicating that the hydrogels showed shear-thinning behavior and thus can be applied as injectable bioinks (Figure 26C). Furthermore, the hydrogels were self-healed by strain, indicating that they could be injected under extrusion and could be self-restored upon cessation of the shear force (Figure 26D). The CD-based polypseudorotaxane structure in the GNP- and or AgNP-based nanocomposite hydrogels was known to undergo thermoreversible threading/dethreading of α-CD from the polymer chains.[451,452] At 58 °C, α-CDs are dethreaded from the PEG chains, resulting in disruption of the hydrogel structure into the transparent sol. Conversely, upon cooling, the sol gradually turned into a hydrogel at room temperature. This temperature-controlled sol−gel transition behavior may be considered one of the main factors in designing bioinks with favorable printability for the construction of 3D materials. Jiang et al. reported on dynamic hybrid hydrogels formed through coordination between AgNPs and thiol or acetyl thioester-containing polymers.[52] AgNPs acted as cross-linking sites to form self-healing dynamic hydrogel networks. This work suggested an advanced system from the researcher's previous work for thermosensitive dynamic hydrogels based on strong chelation between polythioether dendrons and Ag nanoparticles.[450] The amount of AgNPs affected the mechanical properties of resulting hydrogels. When the feed ratio of Ag/S approached 0.9, the hydrogel exhibited the best mechanical properties. Thiol-containing hydrogels showed better self-recovery performance than the hydrogels with acetyl thioester groups.

Table 3 summarizes the testing status of dynamic cross-linked hydrogel systems that can potentially be used as hydrogel-based extrusion bioinks. Even though several hydrogel systems have not been tested for the 3D bioprinting process, their rheological properties, particularly shear-thinning behavior, and injectability have great potential for developing novel hydrogel-based bioink systems for cell-based microextrusion bioprinting.

8. CONCLUSIONS AND OUTLOOK

The ability for hydrogels to achieve desired printing outcomes, referred to as their printability, continues to be of high interest to the field. Researchers have many tools at their disposal to improve the printability of their bioinks, including modifying the chemistry, hydrogel composition, rheological properties, and printing parameters. One of the most challenging aspects of bioink design is the interrelatedness of each of these factors. Composition and chemistry influence the hydrogel's response to external forces (rheological properties) and the window of operable printing conditions which may be appropriate to use. Even the optimal hydrogel will result in poor printing outcomes if the correct printing conditions are not utilized. Meanwhile, although many studies have looked at how chemical modifications influence the rheological properties of different hydrogels, the translation to printability is not always a direct one. It has been established that shear-thinning, yielding, and quick recovery/self-healing behaviors are desirable from a printability perspective. However, some hydrogels may exhibit these properties and still not be sufficient to achieve desired printing outcomes. Further research is needed to improve the predictability of these relationships and allow for more intentional design during the bioink development process.

The current hydrogels as bioinks employed chemical cross-linking before and/or after printing not only to modulate printability but also to stabilize final printed constructs. However, there are several shortcomings, including the limited rheological properties and diversity of these hydrogels. Therefore, a rapidly growing demand exists for newly designed hydrogels that can modulate rheological and mechanical properties for desired printability. In this review, we have presented evolving design strategies developed to control the rheological and mechanical properties of diverse classes of dynamic hydrogels. These hydrogels were formed through different chemical designs to build reversible, cross-linked networks based on physical bonds or dynamic covalent bonds. The rational choice or combination of these bonds is the most important factor in determining the gelation kinetics, and dynamic and/or mechanical behaviors of the resulting hydrogels. From a comprehensive review of recent dynamic hydrogels that show shear-thinning and self-healing characteristics, we have collected a variety of useful information on chemical designs, which may establish general criteria that should be taken into account for the development of optimized bioinks with desirable printability. Through various design approaches, many ideas have been suggested to identify the major control parameters affecting the printability of hydrogel-based bioinks for microextrusion bioprinting. For physical interaction-based hydrogels, the rheological and mechanical properties could be tuned not only by selecting the appropriate class of complementary pairs for physical interactions, but also by adjusting the concentration and composition ratio of each complementary species for physical interactions. For hydrogels with dynamic covalent cross-links, the hydrogel characteristics could also be modulated by several factors including the reaction class, reaction solution pH, reactant concentrations, and ratio between the reactants. Similarly, nanocomposite-based supramolecular hydrogels could also be controlled in terms of dynamics and mechanics by considering the parameters described for physical and dynamic covalent bond-based

https://dx.doi.org/10.1021/acs.chemrev.0c00015
Chem. Rev. 2020, 120, 10834−10886

Table 3. Dynamic Cross-Linked Hydrogel Systems for Potential and Recent Hydrogel-Based Extrusion Bioinks

cross-linking mechanism		hydrogels	testing status: shear-thinning	testing status: injectability[a]	testing status: printability[b]	ref
		Physical Interaction				
hydrogen bonding	phenolic compound-based interaction	gallol-containing hydrogels	◯	◯ (26 or 25 G)	◯	136,138
		datechol-functionalized ABA triblock copolymer hydrogels	◯	◯ (23 G × 3/4″)	×	140
	ureidopyrimidinone self-complementary dimerization	UPy-containing thermosensitive ABA triblock copolymer hydrogels	◯	◯ (20 G)	×	453
host−guest interaction	cyclodextrin-mediated supramolecular interaction	poly-β-cyclodextrin (Pβ-CD)/poly(3,4-ethylenedioxythiophene) (PEDOT):adamantyl-modified sulfated alginate (S-Alg-Ad) hydrogels	◯	◯ (27 G)	×	157
	cucurbit[n]uril-mediated supramolecular interaction	highly branched CB[n]-threaded polyrotaxane (HBP-CB[n])/naphthyl-functionalized hydroxyethyl cellulose (HECNp) hydrogels	◯	×	×	178
metal−ligand coordination	bisphosphonates	bisphosphonate-modified hyaluronic acid/metal ion hydrogels	◯	◯ (21 G)	O	141,190,199
	carboxylates	folate/Zn^{2+} hydrogels	◯	◯	×	207
		Fe^{3+}-carboxylate in UPy-functionalized gelatin hydrogels	◯	×	×	147
	catechols	DOPA-conjugated chitosan/Fe^{3+} ion hydrogels	×	◯	×	227
	histidine	histidine-bearing acrylamide/acrylate copolymer hydrogels cross-linked with Zn^{2+} ions	×	×	×	242
		Dynamic Covalent Bond				
imine bond		chitosan/dibenzaldehyde-functionalized PEG hydrogels	◯	◯ (22, 26, or 32 G)	×	271,273,274
hydrazone bond		hydrazine-modified elastin-like protein/aldehyde-modified hyaluronic acid hydrogels	◯	◯ (28 G)	×	282
		hydrazide-modified hyaluronic acid/benzaldehyde terminated F127 triblock copolymers hydrogels	◯	◯	×	285
oxime bond		poly(n-hydroxyethyl acrylamide-co-methyl vinyl ketone) hydrogels cross-linked with a bifunctional hydroxylamine	◯	◯ (0.6 mm)	◯ (400 μm, 3.0 bar, and 12 mm/s)	294
disulfide bond		thiol functionalized F127/dithiolane modified PEG hydrogels	×	◯ (23 G × 3/4″)	×	299
boronic ester bond		glycopolymer chain-containing copolymer/benzoxaborole-containing copolymer hydrogels	◯	◯ (21 G)	×	327,328
		Nanocomposite Hydrogels				
nanocarbon-based hydrogels	carbon nanotubes	single-walled carbon nanotube (SWCNT)/DNA supramolecular hydrogels	◯	×	×	346
	graphene-based nanomaterials	aminated-graphene oxide/sodium alginate/polyacrylamide/ nanocomposite hydrogel	◯	×	◯ (1.2 bar and 500 mm/min)	352
		phenyl boronic acid-containing copolymer/polydopamine-coated graphene oxide hydrogels	◯	◯ (19 G)	×	335
metal carbonate-based hydrogels	calcium carbonates	poly(acrylic acid)/amorphous $CaCO_3$ hydrogels	◯	×	×	394

https://dx.doi.org/10.1021/acs.chemrev.0c00015
Chem. Rev. 2020, 120, 10834−10886

Table 3. continued

cross-linking mechanism	hydrogels	testing status: shear-thinning	injectability[a]	printability[b]	ref
	Nanocomposite Hydrogels				
	other alkaline earth metal (except for Ca^{2+} ions) and transition metal carbonates	poly(acrylic acid)/alkaline earth or transition metal carbonate hydrogels	◯	×	×	397
nanoclay and silica-based hydrogels	laponites	κ-carrageenan/laponite nanosilicate-based hydrogels	◯	×	◯ (400 μm or 23 G and 20 or 0.5−8 mm/s)	330,413
		DNA/laponite nanosilicate hydrogels	◯	◯ (22 G)	◯ (feed rate: 39 mm/s and flow rate: 10 mm/s)	15
	silica nanoparticles	anionic alginate/gellan polymer mixture/cationic silica nanoparticle composite hydrogels	◯	×	◯ (400 μm, 40−50 kPa, and 10−20 mm/s)	431
metal-based hydrogels	gold nanoparticles	poly(*N*-isopropylacrylamide)/gold nanoparticle composite hydrogels	◯	◯ (20 G)	×	440
	silver nanoparticles	α-CD/PEG polypseudorotaxane/silver nanoparticle composite hydrogels	◯	×	×	338

[a]Information for the hydrogels subjected to the injection through syringe needles. The sizes of needle gauges are presented in the parentheses; in case the information was provided. [b]The hydrogels were tested by 3D printing are marked with open circles. The printing parameters are presented; in case the information was provided.

hydrogels. In addition, the nanoparticle class is another key parameter that determines the physical properties of the corresponding nanocomposite hydrogels. These various control parameters affect the final characteristics of the resulting hydrogels by tuning the molecular interactions in aqueous phases or on nanoparticle surfaces, the reaction kinetics, and the cross-linking densities in the hydrogel matrix. From the clever combination of these various control parameters, one may develop new dynamic hydrogels with tailored rheological and mechanical properties for use as bioinks optimized for specific 3D constructs.

For future developments in bioinks, chemistry-based approaches may offer important clues because the design strategy has the most important influence on the hydrogel properties over other factors, both in terms of gelation kinetics and rheological and mechanical properties. Although recent chemical approaches have shown promise in developing useful hydrogel bioinks that meet the requirements for 3D bioprinting, persistent efforts from a chemistry standpoint should be made to improve the performance of hydrogels that can be exploited for human use. In addition to new chemical strategies, a system design in which multiple bonds are combined in a single system is crucial to efficiently control or improve the printability of hydrogels. Using this approach, one may expect the synergistic role of multiple interactions to enhance the mechanical strength as well as induce rapid recovery after extrusion, which cannot be achieved using a single class of dynamic bonds. Several combinations of bonds for cross-linked networks can be considered possible between different classes of physical bonds, between physical bonds and dynamic covalent bonds, or between different classes of dynamic covalent bonds. As an example, we have discussed the reinforcing effect of oxime dynamic covalent bond-based hydrogels through the formation of hydrogen bonding-induced cross-linking by the cryogelation process. Currently, diverse combinations of multiple interactions have been reported, and this design approach will also be one of the mainstream strategies to control the printability of the various dynamic hydrogels.

For nanocomposite-based dynamic hydrogels, there are a number of considerations for system designs. The choice of the additives can be extended to other nanoparticles that have never been considered before. Although the classes of nanoparticles presented in this review were included based on their frequent use, various surfaces of diverse polymeric, inorganic (metal and metal oxide), and organic−inorganic nanomaterials can be considered for new chemical approaches to produce dynamic hydrogels. Nanoparticle shapes (spherical, rod-like, cubic, or sheet-like) and structures (nonporous solid, porous, or hollow) and their specific surface areas should also be considered to develop novel dynamic nanocomposite hydrogels. The currently used nanoparticles are nearly all based on nonelastic inorganic hard spheres, irrespective of their atomic composition and structures. However, soft and flexible nanostructures, such as nanoemulsions, nanobubbles, and nanogels, have been of interest. These deformable nanoparticles may provide some unprecedented insights in designing dynamic hydrogels because they may significantly affect the rheological properties of hydrogels during shear stress-involved extrusion processes. Along with basic research from a materials point of view, a systematic simulation study of the effect of nanoparticle deformation on the bulk dynamics of hydrogels should also be conducted. As discussed above, the surface chemistry at nanoparticle surfaces can also involve a diverse combination of

https://dx.doi.org/10.1021/acs.chemrev.0c00015
Chem. Rev. 2020, 120, 10834−10886

physical interactions and dynamic covalent bonds. The rational combination of multiple types of bonds may allow the printability of hydrogels to reach a level desirable for producing specific 3D constructs.

By focusing on the various suggestions presented above, we are sure that continuing efforts will lead to great promise for the next stage of development of bioinks, allowing better and more accurate control of optimized rheological and mechanical properties. Finally, the advanced design criteria established by various chemical strategies will undoubtedly contribute to the future development of bioinks with practical applicability in clinical use.

AUTHOR INFORMATION

Corresponding Author

Sang Jin Lee − *Wake Forest Institute for Regenerative Medicine, Wake Forest School of Medicine, Winston−Salem, North Carolina 27157, United States; School of Biomedical Engineering and Sciences, Wake Forest University−Virginia Tech, Winston-Salem, North Carolina 27157, United States;* orcid.org/0000-0002-3899-1909; Email: sjlee@wakehealth.edu

Authors

Sang Cheon Lee − *Wake Forest Institute for Regenerative Medicine, Wake Forest School of Medicine, Winston−Salem, North Carolina 27157, United States; Department of Maxillofacial Biomedical Engineering and Institute of Oral Biology, School of Dentistry, Kyung Hee University, Seoul 02447, Republic of Korea;* orcid.org/0000-0002-8560-0173

Gregory Gillispie − *Wake Forest Institute for Regenerative Medicine, Wake Forest School of Medicine, Winston−Salem, North Carolina 27157, United States; School of Biomedical Engineering and Sciences, Wake Forest University−Virginia Tech, Winston-Salem, North Carolina 27157, United States*

Peter Prim − *Wake Forest Institute for Regenerative Medicine, Wake Forest School of Medicine, Winston−Salem, North Carolina 27157, United States*

Complete contact information is available at: https://pubs.acs.org/10.1021/acs.chemrev.0c00015

Notes

The authors declare no competing financial interest.

Biographies

Sang Cheon Lee received his B.S. (1995) in Polymer Science and Engineering and M.S. (1997) and Ph.D. (2001) in Polymer Chemistry at Inha University, Incheon, South Korea. During the Ph.D. program, he worked as a research trainee at the Korea Institute of Science and Technology (KIST). He took a postdoctoral fellowship in the School of Pharmacy at Purdue University (2001−2003) and the School of Materials Science at the Japan Advanced Institute of Science and Technology (JAIST) (2004). He was a senior research scientist at the Korea Institute of Ceramic Engineering and Technology (KICET) (2004−2009). He is currently a Professor in the School of Dentistry at Kyung Hee University, Seoul, South Korea. In 2019, he was a Visiting Professor at the Wake Forest Institute for Regenerative Medicine (WFIRM), Wake Forest School of Medicine, Winston−Salem, North Carolina. His research interests are focused on the development of mineralized organic−inorganic nanohybrids for applications in drug delivery, molecular imaging, bone tissue engineering, and bioactive implants.

Gregory Gillispie received his Ph.D. from the joint Virginia Tech−Wake Forest University School of Biomedical Engineering Sciences in 2020. Under the advisement of Dr. Sang Jin Lee at the Wake Forest Institute for Regenerative Medicine (WFIRM), his research focused on the printability of extrusion-based bioinks. This work aimed to improve the methodologies which are used to assess printability and to study the underlying mechanisms which impact printing outcomes. Additionally, he has pursued the development of tissue-specific bioinks targeting the regeneration of orthopedic tissues such as bone, tooth, and cartilage.

Peter Prim received his Ph.D. in Industrial and Systems Engineering at the North Carolina State University (NCSU) in 2016 and took a postdoctoral fellowship under the advisement of Dr. Sang Jin Lee at Wake Forest Institute for Regenerative Medicine (WFIRM).

Sang Jin Lee is a tenured Associate Professor and cross-appointed to the Virginia Tech−Wake Forest University School of Biomedical Engineering Sciences. Dr. Lee received his Ph.D. in Chemical Engineering at Hanyang University, Seoul, South Korea, in 2003 and took a postdoctoral fellowship in the Laboratories for Tissue Engineering and Cellular Therapeutics at Harvard Medical School and Children's Hospital Boston and the Wake Forest Institute for Regenerative Medicine (WFIRM), where he is currently a faculty member. He has authored more than 140 scientific publications and reviews, has edited two textbooks, and has written 35 chapters in several books. His current research works focus on: designing tissue-engineered scaffolding system (skin, bone, cartilage, skeletal muscle, tendon/ligament, blood vessel, heart, and kidney), 3D integrated tissue-organ printing (ITOP) system for bioengineering complex, composite tissues, and solid organs, bioink development and printability, bioadhesion and biointegration between biomaterials and cell/tissue, drug/protein delivery system, bioconjugation and polymer synthesis, bioreactor system for preconditioning, in vitro microphysiological system, and NIR fluorescence-based monitoring system.

ACKNOWLEDGMENTS

This review was supported by the National Institutes of Health (1P41EB023833-346 01), National Science Foundation (award no. 1663128), and Medical Technology Enterprise Consortium (no. W81XWH-15-9-0001).

REFERENCES

(1) Atala, A.; Kasper, F. K.; Mikos, A. G. Engineering Complex Tissues. *Sci. Transl. Med.* **2012**, *4*, 160rv12.

(2) Arenas-Herrera, J. E.; Ko, I. K.; Atala, A.; Yoo, J. J. Decellularization for Whole Organ Bioengineering. *Biomed. Mater.* **2013**, *8*, 014106.

(3) Berebichez-Fridman, R.; Montero-Olvera, P. R. Sources and Clinical Applications of Mesenchymal Stem Cells: State-of-the-Art Review. *Sultan Qaboos Univ. Med. J.* **2018**, *18*, 002.

(4) Sachs, P. C.; Mollica, P. A.; Bruno, R. D. Tissue Specific Microenvironments: A Key Tool for Tissue Engineering and Regenerative Medicine. *J. Biol. Eng.* **2017**, *11*, 34.

(5) Malda, J.; Visser, J.; Melchels, F. P.; Jüngst, T.; Hennink, W. E.; Dhert, W. J. A.; Groll, J.; Hutmacher, D. W. Engineering Hydrogels for Biofabrication. *Adv. Mater.* **2013**, *25*, 5011−5028.

(6) Moroni, L.; Burdick, J. A.; Highley, C.; Lee, S. J.; Morimoto, Y.; Takeuchi, S.; Yoo, J. J. Biofabrication Strategies for 3D In Vitro Models and Regenerative Medicine. *Nat. Rev. Mater.* **2018**, *3*, 21−37.

(7) Gopinathan, J.; Noh, I. Recent Trends in Bioinks for 3D Printing. *Biomater. Res.* **2018**, *22*, 11.

(8) Gao, Q.; Zhao, H. M.; Yang, F. F.; Fu, J. Z.; He, Y. In *3D Bioprinting for Reconstructive Surgery Techniques and Application*; Woodhead Publishing: Cambridge, 2018, 7.

(9) Kang, H. W.; Lee, S. J.; Ko, I. K.; Kengla, C.; Yoo, J. J.; Atala, A. A 3D Bioprinting System to Produce Human-Scale Tissue Constructs with Structural Integrity. *Nat. Biotechnol.* **2016**, *34*, 312−319.
(10) Gillispie, G. J.; Park, J.; Copus, J. S.; Pallickaveedu Rajan Asari, A. K.; Yoo, J. J.; Atala, A.; Lee, S. J. In *Principles of Regenerative Medicine*; Academic Press: Cambridge, 2019, 831.
(11) Panwar, A.; Tan, L. Current Status of Bioinks for Micro-Extrusion-Based 3D Bioprinting. *Molecules* **2016**, *21*, 685.
(12) Kim, J. H.; Yoo, J. J.; Lee, S. J. Three-Dimensional Cell-Based Bioprinting for Soft Tissue Regeneration. *Tissue Eng. Regener. Med.* **2016**, *13*, 647−662.
(13) Groll, J.; Burdick, J. A.; Cho, D. W.; Derby, B.; Gelinsky, M.; Heilshorn, S. C.; Jungst, T.; Malda, J.; Mironov, V. A.; Nakayama, K.; et al. A Definition of Bioinks and Their Distinction from Biomaterial Inks. *Biofabrication* **2019**, *11*, 013001.
(14) Jungst, T.; Smolan, W.; Schacht, K.; Scheibel, T.; Groll, J. Strategies and Molecular Design Criteria for 3d Printable Hydrogels. *Chem. Rev.* **2016**, *116*, 1496−1539.
(15) Basu, S.; Pacelli, S.; Feng, Y.; Lu, Q.; Wang, J.; Paul, A. Harnessing the Noncovalent Interactions of DNA Backbone with 2D Silicate Nanodisks to Fabricate Injectable Therapeutic Hydrogels. *ACS Nano* **2018**, *12*, 9866−9880.
(16) Guvendiren, M.; Molde, J.; Soares, R. M.; Kohn, J. Designing Biomaterials for 3D Printing. *ACS Biomater. Sci. Eng.* **2016**, *2*, 1679−1693.
(17) Chimene, D.; Lennox, K. K.; Kaunas, R. R.; Gaharwar, A. K. Advanced Bioinks for 3D Printing: A Materials Science Perspective. *Ann. Biomed. Eng.* **2016**, *44*, 2090−2102.
(18) Chang, C. C.; Boland, E. D.; Williams, S. K.; Hoying, J. B. Direct-Write Bioprinting Three-Dimensional Biohybrid Systems for Future Regenerative Therapies. *J. Biomed. Mater. Res., Part B* **2011**, *98B*, 160−170.
(19) Ozbolat, I. T.; Hospodiuk, M. Current Advances and Future Perspectives in Extrusion-Based Bioprinting. *Biomaterials* **2016**, *76*, 321−343.
(20) Ali, M.; Pr, A. K.; Yoo, J. J.; Zahran, F.; Atala, A.; Lee, S. J. A Photo-Crosslinkable Kidney Ecm-Derived Bioink Accelerates Renal Tissue Formation. *Adv. Healthcare Mater.* **2019**, *8*, No. 1800992.
(21) Gao, T.; Gillispie, G. J.; Copus, J. S.; Pr, A. K.; Seol, Y. J.; Atala, A.; Yoo, J. J.; Lee, S. J. Optimization of Gelatin-Alginate Composite Bioink Printability using Rheological Parameters: A Systematic Approach. *Biofabrication* **2018**, *10*, 034106.
(22) Holzl, K.; Lin, S.; Tytgat, L.; Van Vlierberghe, S.; Gu, L.; Ovsianikov, A. Bioink Properties before, During and after 3D Bioprinting. *Biofabrication* **2016**, *8*, 032002.
(23) Li, M.; Tian, X.; Zhu, N.; Schreyer, D. J.; Chen, X. Modeling Process-Induced Cell Damage in the Biodispensing Process. *Tissue Eng., Part C* **2010**, *16*, 533−542.
(24) Kirchmajer, D. M.; Gorkin, R., III; in het Panhuis, M. An Overview of the Suitability of Hydrogel-Forming Polymers for Extrusion-Based 3D-Printing. *J. Mater. Chem. B* **2015**, *3*, 4105−4117.
(25) Lee, J. M.; Ng, W. L.; Yeong, W. Y. Resolution and Shape in Bioprinting: Strategizing Towards Complex Tissue and Organ Printing. *Appl. Phys. Rev.* **2019**, *6*, 011307.
(26) Mandrycky, C.; Wang, Z.; Kim, K.; Kim, D.-H. 3D Bioprinting for Engineering Complex Tissues. *Biotechnol. Adv.* **2016**, *34*, 422−434.
(27) Kyle, S.; Jessop, Z. M.; Al-Sabah, A.; Whitaker, I. S. 'Printability' of Candidate Biomaterials for Extrusion Based 3D Printing: State-of-the-Art. *Adv. Healthcare Mater.* **2017**, *6*, 1700264.
(28) Kyle, S.; Jessop, Z. M.; Tarassoli, S. P.; Al-Sabah, A.; Whitaker, I. S. In *3D Bioprinting for Reconstructive Surgery Techniques and Application*; Woodhead Publishing: Cambridge, 2018, 173 .
(29) Hospodiuk, M.; Dey, M.; Sosnoski, D.; Ozbolat, I. T. The Bioink: A Comprehensive Review on Bioprintable Materials. *Biotechnol. Adv.* **2017**, *35*, 217−239.
(30) Gillispie, G.; Prim, P.; Copus, J.; Fisher, J.; Mikos, A. G.; Yoo, J. J.; Atala, A.; Lee, S. J. Assessment Methodologies for Extrusion-Based Bioink Printability. *Biofabrication* **2020**, *12*, 022003.
(31) Roehm, K. D.; Madihally, S. V. Bioprinted Chitosan-Gelatin Thermosensitive Hydrogels Using an Inexpensive 3D Printer. *Biofabrication* **2018**, *10*, 015002.
(32) Zhu, F.; Cheng, L.; Yin, J.; Wu, Z. L.; Qian, J.; Fu, J.; Zheng, Q. 3D Printing of Ultratough Polyion Complex Hydrogels. *ACS Appl. Mater. Interfaces* **2016**, *8*, 31304−31310.
(33) Wilson, S. A.; Cross, L. M.; Peak, C. W.; Gaharwar, A. K. Shear-Thinning and Thermo-Reversible Nanoengineered Inks for 3D Bioprinting. *ACS Appl. Mater. Interfaces* **2017**, *9*, 43449−43458.
(34) Chung, J. H. Y.; Naficy, S.; Yue, Z.; Kapsa, R.; Quigley, A.; Moulton, S. E.; Wallace, G. G. Bio-Ink Properties and Printability for Extrusion Printing Living Cells. *Biomater. Sci.* **2013**, *1*, 763−773.
(35) Paxton, N.; Smolan, W.; Bock, T.; Melchels, F.; Groll, J.; Jungst, T. Proposal to Assess Printability of Bioinks for Extrusion-Based Bioprinting and Evaluation of Rheological Properties Governing Bioprintability. *Biofabrication* **2017**, *9*, 044107.
(36) Giuseppe, M. D.; Law, N.; Webb, B.; Macrae, R. A.; Liew, L. J.; Sercombe, T. B.; Dilley, R. J.; Doyle, B. J. Mechanical Behaviour of Alginate-Gelatin Hydrogels for 3D Bioprinting. *J. Mech. Behav. Biomed. Mater.* **2018**, *79*, 150−157.
(37) Webb, B.; Doyle, B. J. Parameter Optimization for 3D Bioprinting of Hydrogels. *Bioprinting* **2017**, *8*, 8−12.
(38) Jin, Y.; Chai, W.; Huang, Y. Printability Study of Hydrogel Solution Extrusion in Nanoclay Yield-Stress Bath During Printing-Then-Gelation Biofabrication. *Mater. Sci. Eng., C* **2017**, *80*, 313−325.
(39) Schuurman, W.; Levett, P. A.; Pot, M. W.; van Weeren, P. R.; Dhert, W. J.; Hutmacher, D. W.; Melchels, F. P.; Klein, T. J.; Malda, J. Gelatin-Methacrylamide Hydrogels as Potential Biomaterials for Fabrication of Tissue-Engineered Cartilage Constructs. *Macromol. Biosci.* **2013**, *13*, 551−561.
(40) Ouyang, L.; Yao, R.; Zhao, Y.; Sun, W. Effect of Bioink Properties on Printability and Cell Viability for 3D Bioplotting of Embryonic Stem Cells. *Biofabrication* **2016**, *8*, 035020.
(41) Habib, A.; Sathish, V.; Mallik, S.; Khoda, B. 3D Printability of Alginate-Carboxymethyl Cellulose Hydrogel. *Materials* **2018**, *11*, 454.
(42) Gohl, J.; Markstedt, K.; Mark, A.; Hakansson, K.; Gatenholm, P.; Edelvik, F. Simulations of 3D Bioprinting: Predicting Bioprintability of Nanofibrillar Inks. *Biofabrication* **2018**, *10*, 034105.
(43) Blaeser, A.; Duarte Campos, D. F.; Weber, M.; Neuss, S.; Theek, B.; Fischer, H.; Jahnen-Dechent, W. Biofabrication under Fluorocarbon: A Novel Freeform Fabrication Technique to Generate High Aspect Ratio Tissue-Engineered Constructs. Biores. *BioRes. Open Access* **2013**, *2*, 374−384.
(44) Zhao, Y.; Li, Y.; Mao, S.; Sun, W.; Yao, R. The Influence of Printing Parameters on Cell Survival Rate and Printability in Microextrusion-Based 3D Cell Printing Technology. *Biofabrication* **2015**, *7*, 045002.
(45) Li, Z.; Huang, S.; Liu, Y.; Yao, B.; Hu, T.; Shi, H.; Xie, J.; Fu, X. Tuning Alginate-Gelatin Bioink Properties by Varying Solvent and Their Impact on Stem Cell Behavior. *Sci. Rep.* **2018**, *8*, 8020.
(46) Lee, J. S.; Kim, B. S.; Seo, D.; Park, J. H.; Cho, D. W. Three-Dimensional Cell Printing of Large-Volume Tissues: Application to Ear Regeneration. *Tissue Eng., Part C* **2017**, *23*, 136−145.
(47) Mouser, V. H.; Melchels, F. P.; Visser, J.; Dhert, W. J.; Gawlitta, D.; Malda, J. Yield Stress Determines Bioprintability of Hydrogels Based on Gelatin-Methacryloyl and Gellan Gum for Cartilage Bioprinting. *Biofabrication* **2016**, *8*, 035003.
(48) Schacht, K.; Jungst, T.; Schweinlin, M.; Ewald, A.; Groll, J.; Scheibel, T. Biofabrication of Cell-Loaded 3D Spider Silk Constructs. *Angew. Chem., Int. Ed.* **2015**, *54*, 2816−2820.
(49) Muller, M.; Becher, J.; Schnabelrauch, M.; Zenobi-Wong, M. Nanostructured Pluronic Hydrogels as Bioinks for 3D Bioprinting. *Biofabrication* **2015**, *7*, 035006.
(50) Muller, M.; Ozturk, E.; Arlov, O.; Gatenholm, P.; Zenobi-Wong, M. Alginate Sulfate-Nanocellulose Bioinks for Cartilage Bioprinting Applications. *Ann. Biomed. Eng.* **2017**, *45*, 210−223.
(51) Abbadessa, A.; Mouser, V. H. M.; Blokzijl, M. M.; Gawlitta, D.; Dhert, W. J. A.; Hennink, W. E.; Malda, J.; Vermonden, T. A Synthetic Thermosensitive Hydrogel for Cartilage Bioprinting and Its Bio-

https://dx.doi.org/10.1021/acs.chemrev.0c00015
Chem. Rev. 2020, 120, 10834−10886

functionalization with Polysaccharides. *Biomacromolecules* **2016**, *17*, 2137−2147.
(52) Jiang, D.; Xue, Q.; Liu, Z.; Han, J.; Wu, X. Novel Anti-Algal Nanocomposite Hydrogels Based on Thiol/Acetyl Thioester Groups Chelating with Silver Nanoparticles. *New J. Chem.* **2017**, *41*, 271−277.
(53) Markstedt, K.; Escalante, A.; Toriz, G.; Gatenholm, P. Biomimetic Inks Based on Cellulose Nanofibrils and Cross-Linkable Xylans for 3D Printing. *ACS Appl. Mater. Interfaces* **2017**, *9*, 40878−40886.
(54) Ahlfeld, T.; Cidonio, G.; Kilian, D.; Duin, S.; Akkineni, A. R.; Dawson, J. I.; Yang, S.; Lode, A.; Oreffo, R. O. C.; Gelinsky, M. Development of a Clay Based Bioink for 3D Cell Printing for Skeletal Application. *Biofabrication* **2017**, *9*, 034103.
(55) Bendtsen, S. T.; Quinnell, S. P.; Wei, M. Development of a Novel Alginate-Polyvinyl Alcohol-Hydroxyapatite Hydrogel for 3D Bioprinting Bone Tissue Engineered Scaffolds. *J. Biomed. Mater. Res., Part A* **2017**, *105*, 1457−1468.
(56) Wang, X.; He, K.; Zhang, W. Optimizing the Fabrication Processes for Manufacturing a Hybrid Hierarchical Polyurethane−Cell/Hydrogel Construct. *J. Bioact. Compat. Polym.* **2013**, *28*, 303−319.
(57) Laronda, M. M.; Rutz, A. L.; Xiao, S.; Whelan, K. A.; Duncan, F. E.; Roth, E. W.; Woodruff, T. K.; Shah, R. N. A Bioprosthetic Ovary Created Using 3D Printed Microporous Scaffolds Restores Ovarian Function in Sterilized Mice. *Nat. Commun.* **2017**, *8*, 15261.
(58) Cohen, D. L.; Lo, W.; Tsavaris, A.; Peng, D.; Lipson, H.; Bonassar, L. J. Increased Mixing Improves Hydrogel Homogeneity and Quality of Three-Dimensional Printed Constructs. *Tissue Eng., Part C* **2011**, *17*, 239−248.
(59) Tabriz, A. G.; Hermida, M. A.; Leslie, N. R.; Shu, W. Three-Dimensional Bioprinting of Complex Cell Laden Alginate Hydrogel Structures. *Biofabrication* **2015**, *7*, 045012.
(60) Suntornnond, R.; Tan, E. Y. S.; An, J.; Chua, C. K. A Highly Printable and Biocompatible Hydrogel Composite for Direct Printing of Soft and Perfusable Vasculature-Like Structures. *Sci. Rep.* **2017**, *7*, 16902.
(61) Ahn, G.; Min, K.-H.; Kim, C.; Lee, J.-S.; Kang, D.; Won, J.-Y.; Cho, D.-W.; Kim, J.-Y.; Jin, S.; Yun, W.-S.; Shim, J.-H. Precise Stacking of Decellularized Extracellular Matrix Based 3D Cell-Laden Constructs by a 3D Cell Printing System Equipped with Heating Modules. *Sci. Rep.* **2017**, *7*, 8624.
(62) He, Y.; Yang, F.; Zhao, H.; Gao, Q.; Xia, B.; Fu, J. Research on the Printability of Hydrogels in 3D Bioprinting. *Sci. Rep.* **2016**, *6*, 29977.
(63) Wu, Y.; Lin, Z. Y.; Wenger, A. C.; Tam, K. C.; Tang, X. 3D Bioprinting of Liver-Mimetic Construct with Alginate/Cellulose Nanocrystal Hybrid Bioink. *Bioprinting* **2018**, *9*, 1−6.
(64) Tirella, A.; Orsini, A.; Vozzi, G.; Ahluwalia, A. A Phase Diagram for Microfabrication of Geometrically Controlled Hydrogel Scaffolds. *Biofabrication* **2009**, *1*, 045002.
(65) Ng, W. L.; Yeong, W. Y.; Naing, M. W. Polyelectrolyte Gelatin-Chitosan Hydrogel Optimized for 3D Bioprinting in Skin Tissue Engineering. *Int. J. Bioprinting* **2016**, *2*, 53−62.
(66) Lee, B. H.; Lum, N.; Seow, L. Y.; Lim, P. Q.; Tan, L. P. Synthesis and Characterization of Types a and B Gelatin Methacryloyl for Bioink Applications. *Materials* **2016**, *9*, 797.
(67) Daly, A. C.; Critchley, S. E.; Rencsok, E. M.; Kelly, D. J. A Comparison of Different Bioinks for 3D Bioprinting of Fibrocartilage and Hyaline Cartilage. *Biofabrication* **2016**, *8*, 045002.
(68) Markstedt, K.; Mantas, A.; Tournier, I.; Martinez Avila, H.; Hagg, D.; Gatenholm, P. 3D Bioprinting Human Chondrocytes with Nanocellulose-Alginate Bioink for Cartilage Tissue Engineering Applications. *Biomacromolecules* **2015**, *16*, 1489−1496.
(69) Kang, K. H.; Hockaday, L. A.; Butcher, J. T. Quantitative Optimization of Solid Freeform Deposition of Aqueous Hydrogels. *Biofabrication* **2013**, *5*, 035001.
(70) Diamantides, N.; Wang, L.; Pruiksma, T.; Siemiatkoski, J.; Dugopolski, C.; Shortkroff, S.; Kennedy, S.; Bonassar, L. J. Correlating Rheological Properties and Printability of Collagen Bioinks: The Effects of Riboflavin Photocrosslinking and Ph. *Biofabrication* **2017**, *9*, 034102.
(71) Rutz, A. L.; Hyland, K. E.; Jakus, A. E.; Burghardt, W. R.; Shah, R. N. A Multimaterial Bioink Method for 3D Printing Tunable, Cell-Compatible Hydrogels. *Adv. Mater.* **2015**, *27*, 1607−1614.
(72) Duarte Campos, D. F.; Blaeser, A.; Korsten, A.; Neuss, S.; Jakel, J.; Vogt, M.; Fischer, H. The Stiffness and Structure of Three-Dimensional Printed Hydrogels Direct the Differentiation of Mesenchymal Stromal Cells toward Adipogenic and Osteogenic Lineages. *Tissue Eng., Part A* **2015**, *21*, 740−756.
(73) Ribeiro, A.; Blokzijl, M. M.; Levato, R.; Visser, C. W.; Castilho, M.; Hennink, W. E.; Vermonden, T.; Malda, J. Assessing Bioink Shape Fidelity to Aid Material Development in 3D Bioprinting. *Biofabrication* **2018**, *10*, 014102.
(74) Melchels, F. P. W.; Dhert, W. J. A.; Hutmacher, D. W.; Malda, J. Development and Characterisation of a New Bioink for Additive Tissue Manufacturing. *J. Mater. Chem. B* **2014**, *2*, 2282−2289.
(75) Athirasala, A.; Tahayeri, A.; Thrivikraman, G.; Franca, C. M.; Monteiro, N.; Tran, V.; Ferracane, J.; Bertassoni, L. E. A Dentin-Derived Hydrogel Bioink for 3D Bioprinting of Cell Laden Scaffolds for Regenerative Dentistry. *Biofabrication* **2018**, *10*, 024101.
(76) Dahal, E.; Badal, A.; Zidan, A.; Alayoubi, A.; Hagio, T.; Glick, S.; Badano, A.; Ghammraoui, B. Stable Gelatin-Based Phantom Materials with Tunable X-Ray Attenuation Properties and 3D Printability for X-Ray Imaging. *Phys. Med. Biol.* **2018**, *63*, 09NT01.
(77) Klar, V.; Pere, J.; Turpeinen, T.; Karki, P.; Orelma, H.; Kuosmanen, P. Shape Fidelity and Structure of 3D Printed High Consistency Nanocellulose. *Sci. Rep.* **2019**, *9*, 3822.
(78) Duan, B.; Hockaday, L. A.; Kang, K. H.; Butcher, J. T. 3D Bioprinting of Heterogeneous Aortic Valve Conduits with Alginate/Gelatin Hydrogels. *J. Biomed. Mater. Res., Part A* **2013**, *101A*, 1255−1264.
(79) Lee, D. Y.; Lee, H.; Kim, Y.; Yoo, S. Y.; Chung, W. J.; Kim, G. Phage as Versatile Nanoink for Printing 3-D Cell-Laden Scaffolds. *Acta Biomater.* **2016**, *29*, 112−124.
(80) Kopf, M.; Campos, D. F.; Blaeser, A.; Sen, K. S.; Fischer, H. A Tailored Three-Dimensionally Printable Agarose-Collagen Blend Allows Encapsulation, Spreading, and Attachment of Human Umbilical Artery Smooth Muscle Cells. *Biofabrication* **2016**, *8*, 025011.
(81) Murphy, S. V.; Skardal, A.; Atala, A. Evaluation of Hydrogels for Bio-Printing Applications. *J. Biomed. Mater. Res., Part A* **2013**, *101A*, 272−284.
(82) Law, N.; Doney, B.; Glover, H.; Qin, Y.; Aman, Z. M.; Sercombe, T. B.; Liew, L. J.; Dilley, R. J.; Doyle, B. J. Characterisation of Hyaluronic Acid Methylcellulose Hydrogels for 3D Bioprinting. *J. Mech. Behav. Biomed. Mater.* **2018**, *77*, 389−399.
(83) Duan, B.; Kapetanovic, E.; Hockaday, L. A.; Butcher, J. T. Three-Dimensional Printed Trileaflet Valve Conduits Using Biological Hydrogels and Human Valve Interstitial Cells. *Acta Biomater.* **2014**, *10*, 1836−1846.
(84) Wust, S.; Godla, M. E.; Muller, R.; Hofmann, S. Tunable Hydrogel Composite with Two-Step Processing in Combination with Innovative Hardware Upgrade for Cell-Based Three-Dimensional Bioprinting. *Acta Biomater.* **2014**, *10*, 630−640.
(85) Yan, K. C.; Nair, K.; Sun, W. Three Dimensional Multi-Scale Modelling and Analysis of Cell Damage in Cell-Encapsulated Alginate Constructs. *J. Biomech.* **2010**, *43*, 1031−1038.
(86) Lee, J. M.; Yeong, W. Y. A Preliminary Model of Time-Pressure Dispensing System for Bioprinting Based on Printing and Material Parameters. *Virtual Phys. Prototyp.* **2015**, *10*, 3−8.
(87) Cheng, J.; Lin, F.; Liu, H.; Yan, Y.; Wang, X.; Zhang, R.; Xiong, Z. Rheological Properties of Cell-Hydrogel Composites Extruding through Small-Diameter Tips. *J. Manuf. Sci. Eng.* **2008**, *130*, 021014 DOI: 10.1115/1.2896215.
(88) Aguado, B. A.; Mulyasasmita, W.; Su, J.; Lampe, K. J.; Heilshorn, S. C. Improving Viability of Stem Cells During Syringe Needle Flow through the Design of Hydrogel Cell Carriers. Tissue Eng. *Tissue Eng., Part A* **2012**, *18*, 806−815.
(89) Li, H.; Liu, S.; Lin, L. Rheological Study on 3D Printability of Alginate Hydrogel and Effect of Graphene Oxide. *Int. J. Bioprinting* **2016**, *2*, 163.

(90) Li, Z.; Huang, S.; Liu, Y.; Yao, B.; Hu, T.; Shi, H.; Xie, J.; Fu, X. Tuning Alginate-Gelatin Bioink Properties by Varying Solvent and Their Impact on Stem Cell Behavior. *Sci. Rep.* **2018**, *8*, 8020.
(91) Sweeney, M.; Campbell, L. L.; Hanson, J.; Pantoya, M. L.; Christopher, G. F. Characterizing the Feasibility of Processing Wet Granular Materials to Improve Rheology for 3D Printing. *J. Mater. Sci.* **2017**, *52*, 13040−13053.
(92) Zhu, F.; Cheng, L.; Yin, J.; Wu, Z. L.; Qian, J.; Fu, J.; Zheng, Q. 3D Printing of Ultratough Polyion Complex Hydrogels. *ACS Appl. Mater. Interfaces* **2016**, *8*, 31304−31310.
(93) Smith, P. T.; Basu, A.; Saha, A.; Nelson, A. Chemical Modification and Printability of Shear-Thinning Hydrogel Inks for Direct-Write 3D Printing. *Polymer* **2018**, *152*, 42−50.
(94) Jungst, T.; Smolan, W.; Schacht, K.; Scheibel, T.; Groll, J. Strategies and Molecular Design Criteria for 3D Printable Hydrogels. *Chem. Rev.* **2016**, *116*, 1496−1539.
(95) Oyen, M. L. Mechanical Characterisation of Hydrogel Materials. *Int. Mater. Rev.* **2014**, *59*, 44−59.
(96) Picout, D. R.; Ross-Murphy, S. B. Rheology of Biopolymer Solutions and Gels. *Sci. World J.* **2003**, *3*, 105−121.
(97) Nadgorny, M.; Xiao, Z.; Connal, L. A. 2d and 3D-Printing of Self-Healing Gels: Design and Extrusion of Self-Rolling Objects. *Mol. Syst. Des. Eng.* **2017**, *2*, 283−292.
(98) Kiyotake, E. A.; Douglas, A. W.; Thomas, E. E.; Nimmo, S. L.; Detamore, M. S. Development and Quantitative Characterization of the Precursor Rheology of Hyaluronic Acid Hydrogels for Bioprinting. *Acta Biomater.* **2019**, *95*, 176−187.
(99) Peak, C. W.; Stein, J.; Gold, K. A.; Gaharwar, A. K. Nanoengineered Colloidal Inks for 3D Bioprinting. *Langmuir* **2018**, *34*, 917−925.
(100) Shin, S.; Park, S.; Park, M.; Jeong, E.; Na, K.; Youn, H. J.; Hyun, J. Cellulose Nanofibers for the Enhancement of Printability of Low Viscosity Gelatin Derivatives. *BioResources* **2017**, *12*, 2941−2954.
(101) Coussot, P. Yield Stress Fluid Flows: A Review of Experimental Data. *J. Non-Newtonian Fluid Mech.* **2014**, *211*, 31−49.
(102) M?ller, P. C. F.; Fall, A.; Bonn, D. Origin of Apparent Viscosity in Yield Stress Fluids Below Yielding. *Epl-Europhys. Lett.* **2009**, *87*, 38004.
(103) Dávila, J. L.; d'Ávila, M. A. Rheological Evaluation of Laponite/Alginate Inks for 3D Extrusion-Based Printing. *Int. J. Adv. Manuf. Technol.* **2019**, *101*, 675−686.
(104) Li, Z.; Huang, S.; Liu, Y. F.; Yao, B.; Hu, T.; Shi, H. G.; Xie, J. F.; Fu, X. B. Tuning Alginate-Gelatin Bioink Properties by Varying Solvent and Their Impact on Stem Cell Behavior. *Sci. Rep.* **2018**, *8*, 8020.
(105) Sarker, M.; Chen, X. B. Modeling the Flow Behavior and Flow Rate of Medium Viscosity Alginate for Scaffold Fabrication with a Three-Dimensional Bioplotter. *J. Manuf. Sci. E-T. ASME* **2017**, *139*, 081002.
(106) Kraut, G.; Yenchesky, L.; Prieto, F.; Tovar, G. E. M.; Southan, A. Influence of Shear Thinning and Material Flow on Robotic Dispensing of Poly(Ethylene Glycol) Diacrylate/Poloxamer 407 Hydrogels. *J. Appl. Polym. Sci.* **2017**, *134*, 45083.
(107) Khalil, S.; Sun, W. Biopolymer Deposition for Freeform Fabrication of Hydrogel Tissue Constructs. *Mater. Sci. Eng., C* **2007**, *27*, 469−478.
(108) Duty, C.; Ajinjeru, C.; Kishore, V.; Compton, B.; Hmeidat, N.; Chen, X.; Liu, P.; Hassen, A. A.; Lindahl, J.; Kunc, V. What Makes a Material Printable? A Viscoelastic Model for Extrusion-Based 3D Printing of Polymers. *J. Manuf. Process* **2018**, *35*, 526−537.
(109) Jessop, Z. M.; Al-Sabah, A.; Gao, N.; Kyle, S.; Thomas, B.; Badiei, N.; Hawkins, K.; Whitaker, I. S. Printability of Pulp Derived Crystal, Fibril and Blend Nanocellulose-Alginate Bioinks for Extrusion 3D Bioprinting. *Biofabrication* **2019**, *11*, 045006.
(110) Jia, J.; Richards, D. J.; Pollard, S.; Tan, Y.; Rodriguez, J.; Visconti, R. P.; Trusk, T. C.; Yost, M. J.; Yao, H.; Markwald, R. R.; Mei, Y. Engineering Alginate as Bioink for Bioprinting. *Acta Biomater.* **2014**, *10*, 4323−4331.
(111) Suntornnond, R.; Tan, E.; An, J.; Chua, C. A Mathematical Model on the Resolution of Extrusion Bioprinting for the Development of New Bioinks. *Materials* **2016**, *9*, 756.
(112) He, Y.; Yang, F.; Zhao, H.; Gao, Q.; Xia, B.; Fu, J. Research on the Printability of Hydrogels in 3D Bioprinting. *Sci. Rep.* **2016**, *6*, 29977.
(113) Vijayavenkataraman, S.; Vialli, N.; Fuh, J. Y. H.; Feng Lu, W. Conductive Collagen/Ppy-B-Pcl Hydrogel for Bioprinting of Neural Tissue Constructs. *Int. J. Bioprinting* **2019**, *5*, 229.
(114) Habib, M. A.; Khoda, B. Development of Clay Based Novel Bio-Ink for 3D Bio-Printing Process. *Procedia Manuf.* **2018**, *26*, 846−856.
(115) Therriault, D.; White, S. R.; Lewis, J. A. Rheological Behavior of Fugitive Organic Inks for Direct-Write Assembly. *Appl. Rheol.* **2007**, *17*, 10112.
(116) Zhang, Y. S.; Khademhosseini, A. Advances in Engineering Hydrogels. *Science* **2017**, *356*, No. eaaf3627.
(117) Hu, W.; Wang, Z.; Xiao, Y.; Zhang, S.; Wang, J. Advances in Crosslinking Strategies of Biomedical Hydrogels. *Biomater. Sci.* **2019**, *7*, 843−855.
(118) Yesilyurt, V.; Ayoob, A. M.; Appel, E. A.; Borenstein, J. T.; Langer, R.; Anderson, D. G. Mixed Reversible Covalent Crosslink Kinetics Enable Precise, Hierarchical Mechanical Tuning of Hydrogel Networks. *Adv. Mater.* **2017**, *29*, 1605947.
(119) Saunders, L.; Ma, P. X. Self-Healing Supramolecular Hydrogels for Tissue Engineering Applications. *Macromol. Biosci.* **2019**, *19*, 1800313.
(120) Tu, Y.; Chen, N.; Li, C.; Liu, H.; Zhu, R.; Chen, S.; Xiao, Q.; Liu, J.; Ramakrishna, S.; He, L. Advances in Injectable Self-Healing Biomedical Hydrogels. *Acta Biomater.* **2019**, *90*, 1−20.
(121) Talebian, S.; Mehrali, M.; Taebnia, N.; Pennisi, C. P.; Kadumudi, F. B.; Foroughi, J.; Hasany, M.; Nikkhah, M.; Akbari, M.; Orive, G.; Dolatshahi-Pirouz, A. Self-Healing Hydrogels: The Next Paradigm Shift in Tissue Engineering? *Adv. Sci.* **2019**, *6*, 1801664.
(122) Tu, Y.; Chen, N.; Li, C.; Liu, H.; Zhu, R.; Chen, S.; Xiao, Q.; Liu, J.; Ramakrishna, S.; He, L. Advances in Injectable Self-Healing Biomedical Hydrogels. *Acta Biomater.* **2019**, *90*, 1−20.
(123) Ding, X.; Wang, Y. Weak Bond-Based Injectable and Stimuli Responsive Hydrogels for Biomedical Applications. *J. Mater. Chem. B* **2017**, *5*, 887−906.
(124) Wang, H.; Heilshorn, S. C. Adaptable Hydrogel Networks with Reversible Linkages for Tissue Engineering. *Adv. Mater.* **2015**, *27*, 3717−3736.
(125) Jungst, T.; Smolan, W.; Schacht, K.; Scheibel, T.; Groll, J. r. Strategies and Molecular Design Criteria for 3D Printable Hydrogels. *Chem. Rev.* **2016**, *116*, 1496−1539.
(126) Desiraju, G. R. Hydrogen Bridges in Crystal Engineering: Interactions without Borders. *Acc. Chem. Res.* **2002**, *35*, 565−573.
(127) Keten, S.; Xu, Z.; Ihle, B.; Buehler, M. J. Nanoconfinement Controls Stiffness, Strength and Mechanical Toughness of B-Sheet Crystals in Silk. *Nat. Mater.* **2010**, *9*, 359−367.
(128) Appel, E. A.; del Barrio, J.; Loh, X. J.; Scherman, O. A. Supramolecular Polymeric Hydrogels. *Chem. Soc. Rev.* **2012**, *41*, 6195−6214.
(129) Tan, H.; Xiao, C.; Sun, J.; Xiong, D.; Hu, X. Biological Self-Assembly of Injectable Hydrogel as Cell Scaffold Via Specific Nucleobase Pairing. *Chem. Commun.* **2012**, *48*, 10289−10291.
(130) Dankers, P. Y.; van Luyn, M. J.; Huizinga-van der Vlag, A.; van Gemert, G. M.; Petersen, A. H.; Meijer, E.; Janssen, H. M.; Bosman, A. W.; Popa, E. R. Development and in-Vivo Characterization of Supramolecular Hydrogels for Intrarenal Drug Delivery. *Biomaterials* **2012**, *33*, 5144−5155.
(131) Guo, M.; Pitet, L. M.; Wyss, H. M.; Vos, M.; Dankers, P. Y.; Meijer, E. Tough Stimuli-Responsive Supramolecular Hydrogels with Hydrogen-Bonding Network Junctions. *J. Am. Chem. Soc.* **2014**, *136*, 6969−6977.
(132) Phadke, A.; Zhang, C.; Arman, B.; Hsu, C.-C.; Mashelkar, R. A.; Lele, A. K.; Tauber, M. J.; Arya, G.; Varghese, S. Rapid Self-Healing Hydrogels. *Proc. Natl. Acad. Sci. U. S. A.* **2012**, *109*, 4383−4388.

https://dx.doi.org/10.1021/acs.chemrev.0c00015
Chem. Rev. 2020, 120, 10834−10886

(133) Wang, P.; Zhang, J.; Li, Y.; Wang, N.; Liu, W. A Nucleoside Responsive Diaminotriazine-Based Hydrogen Bonding Strengthened Hydrogel. *Mater. Lett.* **2015**, *142*, 71−74.
(134) Zheng, L. Y.; Shi, J. M.; Chi, Y. H. Tannic Acid Physically Cross-Linked Responsive Hydrogel. *Macromol. Chem. Phys.* **2018**, *219*, 1800234.
(135) Duan, L.; Yuan, Q.; Xiang, H.; Yang, X.; Liu, L.; Li, J. Fabrication and Characterization of a Novel Collagen-Catechol Hydrogel. *J. Biomater. Appl.* **2018**, *32*, 862−870.
(136) Shin, M.; Lee, H. Gallol-Rich Hyaluronic Acid Hydrogels: Shear-Thinning, Protein Accumulation against Concentration Gradients, and Degradation-Resistant Properties. *Chem. Mater.* **2017**, *29*, 8211−8220.
(137) Fan, H.; Wang, L.; Feng, X.; Bu, Y.; Wu, D.; Jin, Z. Supramolecular Hydrogel Formation Based on Tannic Acid. *Macromolecules* **2017**, *50*, 666−676.
(138) Shin, M.; Galarraga, J. H.; Kwon, M. Y.; Lee, H.; Burdick, J. A. Gallol-Derived Ecm-Mimetic Adhesive Bioinks Exhibiting Temporal Shear-Thinning and Stabilization Behavior. *Acta Biomater.* **2019**, *95*, 165−175.
(139) Abrash, H. I.; Shih, D.; Elias, W.; Malekmehr, F. A Kinetic Study of the Air Oxidation of Pyrogallol and Purpurogallin. *Int. J. Chem. Kinet.* **1989**, *21*, 465−476.
(140) Li, L.; Yan, B.; Yang, J.; Huang, W.; Chen, L.; Zeng, H. Injectable Self-Healing Hydrogel with Antimicrobial and Antifouling Properties. *ACS Appl. Mater. Interfaces* **2017**, *9*, 9221−9225.
(141) Zhang, K.; Feng, Q.; Xu, J.; Xu, X.; Tian, F.; Yeung, K. W.; Bian, L. Self-Assembled Injectable Nanocomposite Hydrogels Stabilized by Bisphosphonate-Magnesium (Mg2+) Coordination Regulates the Differentiation of Encapsulated Stem Cells Via Dual Crosslinking. *Adv. Funct. Mater.* **2017**, *27*, 1701642.
(142) Street, D. P.; Ledford, W. K.; Allison, A. A.; Patterson, S.; Pickel, D. L.; Lokitz, B. S.; Messman, J. M.; Kilbey, S. M. Self-Complementary Multiple Hydrogen-Bonding Additives Enhance Thermomechanical Properties of 3D-Printed Pmma Structures. *Macromolecules* **2019**, *52*, 5574−5582.
(143) Pekkanen, A. M.; Mondschein, R. J.; Williams, C. B.; Long, T. E. 3D Printing Polymers with Supramolecular Functionality for Biological Applications. *Biomacromolecules* **2017**, *18*, 2669−2687.
(144) Bastings, M. M. C.; Koudstaal, S.; Kieltyka, R. E.; Nakano, Y.; Pape, A. C. H.; Feyen, D. A. M.; van Slochteren, F. J.; Doevendans, P. A.; Sluijter, J. P. G.; Meijer, E. W.; Chamuleau, S. A. J.; Dankers, P. Y. W. A Fast Ph-Switchable and Self-Healing Supramolecular Hydrogel Carrier for Guided, Local Catheter Injection in the Infarcted Myocardium. *Adv. Healthcare Mater.* **2014**, *3*, 70−78.
(145) Jeon, I.; Cui, J.; Illeperuma, W. R.; Aizenberg, J.; Vlassak, J. J. Extremely Stretchable and Fast Self-Healing Hydrogels. *Adv. Mater.* **2016**, *28*, 4678−4683.
(146) Qin, Z.; Yu, X.; Wu, H.; Li, J.; Lv, H.; Yang, X. Nonswellable and Tough Supramolecular Hydrogel Based on Strong Micelle Cross-Linkings. *Biomacromolecules* **2019**, *20*, 3399−3407.
(147) Zhang, G.; Lv, L.; Deng, Y.; Wang, C. Self-Healing Gelatin Hydrogels Cross-Linked by Combining Multiple Hydrogen Bonding and Ionic Coordination. *Macromol. Rapid Commun.* **2017**, *38*, 1700018.
(148) Wenz, G.; Han, B.-H.; Müller, A. Cyclodextrin Rotaxanes and Polyrotaxanes. *Chem. Rev.* **2006**, *106*, 782−817.
(149) Liu, S.; Ruspic, C.; Mukhopadhyay, P.; Chakrabarti, S.; Zavalij, P. Y.; Isaacs, L. The Cucurbit [N] Uril Family: Prime Components for Self-Sorting Systems. *J. Am. Chem. Soc.* **2005**, *127*, 15959−15967.
(150) Mantooth, S. M.; Munoz-Robles, B. G.; Webber, M. J. Dynamic Hydrogels from Host−Guest Supramolecular Interactions. *Macromol. Biosci.* **2019**, *19*, 1800281.
(151) Al-Burtomani, S. K.; Suliman, F. O. Inclusion Complexes of Norepinephrine with B-Cyclodextrin, 18-Crown-6 and Cucurbit [7] Uril: Experimental and Molecular Dynamics Study. *RSC Adv.* **2017**, *7*, 9888−9901.
(152) Loebel, C.; Rodell, C. B.; Chen, M. H.; Burdick, J. A. Shear-Thinning and Self-Healing Hydrogels as Injectable Therapeutics and for 3D-Printing. *Nat. Protoc.* **2017**, *12*, 1521.
(153) Rodell, C. B.; Kaminski, A. L.; Burdick, J. A. Rational Design of Network Properties in Guest−Host Assembled and Shear-Thinning Hyaluronic Acid Hydrogels. *Biomacromolecules* **2013**, *14*, 4125−4134.
(154) Rodell, C. B.; Wade, R. J.; Purcell, B. P.; Dusaj, N. N.; Burdick, J. A. Selective Proteolytic Degradation of Guest−Host Assembled, Injectable Hyaluronic Acid Hydrogels. *ACS Biomater. Sci. Eng.* **2015**, *1*, 277−286.
(155) Jia, Y.-G.; Zhu, X. Self-Healing Supramolecular Hydrogel Made of Polymers Bearing Cholic Acid and B-Cyclodextrin Pendants. *Chem. Mater.* **2015**, *27*, 387−393.
(156) Miyamae, K.; Nakahata, M.; Takashima, Y.; Harada, A. Self-Healing, Expansion−Contraction, and Shape-Memory Properties of a Preorganized Supramolecular Hydrogel through Host−Guest Interactions. *Angew. Chem., Int. Ed.* **2015**, *54*, 8984−8987.
(157) Xu, Y.; Cui, M.; Patsis, P. A.; Gunther, M.; Yang, X.; Eckert, K.; Zhang, Y. Reversibly Assembled Electroconductive Hydrogel Via a Host−Guest Interaction for 3D Cell Culture. *ACS Appl. Mater. Interfaces* **2019**, *11*, 7715−7724.
(158) Zhang, S.; Cicoira, F. Water-Enabled Healing of Conducting Polymer Films. *Adv. Mater.* **2017**, *29*, 1703098.
(159) Shi, Z.; Gao, X.; Ullah, M. W.; Li, S.; Wang, Q.; Yang, G. Electroconductive Natural Polymer-Based Hydrogels. *Biomaterials* **2016**, *111*, 40−54.
(160) Xu, Y.; Yang, X.; Thomas, A. K.; Patsis, P. A.; Kurth, T.; Kräter, M.; Eckert, K.; Bornhäuser, M.; Zhang, Y. Noncovalently Assembled Electroconductive Hydrogel. *ACS Appl. Mater. Interfaces* **2018**, *10*, 14418−14425.
(161) Roshanbinfar, K.; Vogt, L.; Greber, B.; Diecke, S.; Boccaccini, A. R.; Scheibel, T.; Engel, F. B. Electroconductive Biohybrid Hydrogel for Enhanced Maturation and Beating Properties of Engineered Cardiac Tissues. *Adv. Funct. Mater.* **2018**, *28*, 1803951.
(162) Liu, X.; Miller, A. L.; Park, S.; Waletzki, B. E.; Zhou, Z.; Terzic, A.; Lu, L. Functionalized Carbon Nanotube and Graphene Oxide Embedded Electrically Conductive Hydrogel Synergistically Stimulates Nerve Cell Differentiation. *ACS Appl. Mater. Interfaces* **2017**, *9*, 14677−14690.
(163) Huang, G.; Li, F.; Zhao, X.; Ma, Y.; Li, Y.; Lin, M.; Jin, G.; Lu, T. J.; Genin, G. M.; Xu, F. Functional and Biomimetic Materials for Engineering of the Three-Dimensional Cell Microenvironment. *Chem. Rev.* **2017**, *117*, 12764−12850.
(164) Pappas, C. G.; Shafi, R.; Sasselli, I. R.; Siccardi, H.; Wang, T.; Narang, V.; Abzalimov, R.; Wijerathne, N.; Ulijn, R. V. Dynamic Peptide Libraries for the Discovery of Supramolecular Nanomaterials. *Nat. Nanotechnol.* **2016**, *11*, 960.
(165) Clarke, D. E.; Parmenter, C. D.; Scherman, O. A. Tunable Pentapeptide Self-Assembled B-Sheet Hydrogels. *Angew. Chem., Int. Ed.* **2018**, *57*, 7709−7713.
(166) Silva, G. A.; Czeisler, C.; Niece, K. L.; Beniash, E.; Harrington, D. A.; Kessler, J. A.; Stupp, S. I. Selective Differentiation of Neural Progenitor Cells by High-Epitope Density Nanofibers. *Science* **2004**, *303*, 1352−1355.
(167) Hauser, C. A. E.; Deng, R.; Mishra, A.; Loo, Y.; Khoe, U.; Zhuang, F.; Cheong, D. W.; Accardo, A.; Sullivan, M. B.; Riekel, C.; Ying, J. Y.; Hauser, U. A. Natural Tri-to Hexapeptides Self-Assemble in Water to Amyloid B-Type Fiber Aggregates by Unexpected A-Helical Intermediate Structures. *Proc. Natl. Acad. Sci. U. S. A.* **2011**, *108*, 1361−1366.
(168) Redondo-Gomez, C.; Abdouni, Y.; Becer, C. R.; Mata, A. Self-Assembling Hydrogels Based on a Complementary Host-Guest Peptide Amphiphile Pair. *Biomacromolecules* **2019**, *20*, 2276−2285.
(169) Wang, L. L.; Sloand, J. N.; Gaffey, A. C.; Venkataraman, C. M.; Wang, Z.; Trubelja, A.; Hammer, D. A.; Atluri, P.; Burdick, J. A. Injectable, Guest−Host Assembled Polyethylenimine Hydrogel for Sirna Delivery. *Biomacromolecules* **2017**, *18*, 77−86.
(170) Kim, Y.-M.; Park, M.-R.; Song, S.-C. Injectable Polyplex Hydrogel for Localized and Long-Term Delivery of Sirna. *ACS Nano* **2012**, *6*, 5757−5766.

https://dx.doi.org/10.1021/acs.chemrev.0c00015
Chem. Rev. 2020, 120, 10834−10886

(171) Kim, Y.-M.; Park, M.-R.; Song, S.-C. An Injectable Cell Penetrable Nano-Polyplex Hydrogel for Localized Sirna Delivery. *Biomaterials* **2013**, *34*, 4493−4500.
(172) Kim, J.; Jung, I.-S.; Kim, S.-Y.; Lee, E.; Kang, J.-K.; Sakamoto, S.; Yamaguchi, K.; Kim, K. New Cucurbituril Homologues: Syntheses, Isolation, Characterization, and X-Ray Crystal Structures of Cucurbit [N] Uril (N= 5, 7, and 8). *J. Am. Chem. Soc.* **2000**, *122*, 540−541.
(173) Assaf, K. I.; Nau, W. M. Cucurbiturils: From Synthesis to High-Affinity Binding and Catalysis. *Chem. Soc. Rev.* **2015**, *44*, 394−418.
(174) Liu, J.; Tan, C. S. Y.; Yu, Z.; Lan, Y.; Abell, C.; Scherman, O. A. Biomimetic Supramolecular Polymer Networks Exhibiting Both Toughness and Self-Recovery. *Adv. Mater.* **2017**, *29*, 1604951.
(175) Liu, J.; Tan, C. S. Y.; Yu, Z.; Li, N.; Abell, C.; Scherman, O. A. Tough Supramolecular Polymer Networks with Extreme Stretchability and Fast Room-Temperature Self-Healing. *Adv. Mater.* **2017**, *29*, 1605325.
(176) Li, C.; Rowland, M. J.; Shao, Y.; Cao, T.; Chen, C.; Jia, H.; Zhou, X.; Yang, Z.; Scherman, O. A.; Liu, D. Responsive Double Network Hydrogels of Interpenetrating DNA and Cb [8] Host−Guest Supramolecular Systems. *Adv. Mater.* **2015**, *27*, 3298−3304.
(177) Zou, L.; Braegelman, A. S.; Webber, M. J. Dynamic Supramolecular Hydrogels Spanning an Unprecedented Range of Host−Guest Affinity. *ACS Appl. Mater. Interfaces* **2019**, *11*, 5695−5700.
(178) Tan, C. S. Y.; Liu, J.; Groombridge, A. S.; Barrow, S. J.; Dreiss, C. A.; Scherman, O. A. Controlling Spatiotemporal Mechanics of Supramolecular Hydrogel Networks with Highly Branched Cucurbit [8] Uril Polyrotaxanes. *Adv. Funct. Mater.* **2018**, *28*, 1702994.
(179) Correia, H. D.; Chowdhury, S.; Ramos, A. P.; Guy, L.; Demets, G. J. F.; Bucher, C. Dynamic Supramolecular Polymers Built from Cucurbit [N] Urils and Viologens. *Polym. Int.* **2019**, *68*, 572−588.
(180) Yu, Z.; Liu, J.; Tan, C. S. Y.; Scherman, O. A.; Abell, C. Supramolecular Nested Microbeads as Building Blocks for Macroscopic Self-Healing Scaffolds. *Angew. Chem., Int. Ed.* **2018**, *57*, 3079−3083.
(181) Kang, Y.; Tang, X.; Yu, H.; Cai, Z.; Huang, Z.; Wang, D.; Xu, J.-F.; Zhang, X. Supramolecular Catalyst Functions in Catalytic Amount: Cucurbit [8] Uril Accelerates the Photodimerization of Brooker's Merocyanine. *Chem. Sci.* **2017**, *8*, 8357−8361.
(182) Tang, X.; Huang, Z.; Chen, H.; Kang, Y.; Xu, J. F.; Zhang, X. Supramolecularly Catalyzed Polymerization: From Consecutive Dimerization to Polymerization. *Angew. Chem., Int. Ed.* **2018**, *57*, 8545−8549.
(183) Kang, Y.; Cai, Z.; Huang, Z.; Tang, X.; Xu, J.-F.; Zhang, X. Controllable Supramolecular Polymerization Promoted by Host-Enhanced Photodimerization. *ACS Macro Lett.* **2016**, *5*, 1397−1401.
(184) Truong, V. X.; Li, F.; Ercole, F.; Forsythe, J. S. Wavelength-Selective Coupling and Decoupling of Polymer Chains Via Reversible [2+ 2] Photocycloaddition of Styrylpyrene for Construction of Cytocompatible Photodynamic Hydrogels. *ACS Macro Lett.* **2018**, *7*, 464−469.
(185) Marschner, D. E.; Frisch, H.; Offenloch, J. T.; Tuten, B. T.; Becer, C. R.; Walther, A.; Goldmann, A. S.; Tzvetkova, P.; Barner-Kowollik, C. Visible Light [2+ 2] Cycloadditions for Reversible Polymer Ligation. *Macromolecules* **2018**, *51*, 3802−3807.
(186) Tabet, A.; Forster, R. A.; Parkins, C. C.; Wu, G.; Scherman, O. A. Modulating Stiffness with Photo-Switchable Supramolecular Hydrogels. *Polym. Chem.* **2019**, *10*, 467−472.
(187) Zou, L.; Webber, M. J. Reversible Hydrogel Dynamics by Physical−Chemical Crosslink Photoswitching Using a Supramolecular Macrocycle Template. *Chem. Commun.* **2019**, *55*, 9931−9934.
(188) Kuang, L.; Ma, X.; Ma, Y.; Yao, Y.; Tariq, M.; Yuan, Y.; Liu, C. Self-Assembled Injectable Nanocomposite Hydrogels Coordinated by in Situ Generated Cap Nanoparticles for Bone Regeneration. *ACS Appl. Mater. Interfaces* **2019**, *11*, 17234−17246.
(189) Shi, L.; Ding, P.; Wang, Y.; Zhang, Y.; Ossipov, D.; Hilborn, J. Self-Healing Polymeric Hydrogel Formed by Metal−Ligand Coordination Assembly: Design, Fabrication, and Biomedical Applications. *Macromol. Rapid Commun.* **2019**, *40*, 1800837.
(190) Zhang, K.; Yuan, W.; Wei, K.; Yang, B.; Chen, X.; Li, Z.; Zhang, Z.; Bian, L. Highly Dynamic Nanocomposite Hydrogels Self-Assembled by Metal Ion-Ligand Coordination. *Small* **2019**, *15*, 1900242.
(191) Cole, L. E.; Vargo-Gogola, T.; Roeder, R. K. Targeted Delivery to Bone and Mineral Deposits Using Bisphosphonate Ligands. *Adv. Drug Delivery Rev.* **2016**, *99*, 12−27.
(192) Shi, L.; Zhao, Y.; Xie, Q.; Fan, C.; Hilborn, J.; Dai, J.; Ossipov, D. A. Moldable Hyaluronan Hydrogel Enabled by Dynamic Metal−Bisphosphonate Coordination Chemistry for Wound Healing. *Adv. Healthcare Mater.* **2018**, *7*, 1700973.
(193) Shi, L.; Wang, F.; Zhu, W.; Xu, Z.; Fuchs, S.; Hilborn, J.; Zhu, L.; Ma, Q.; Wang, Y.; Weng, X.; Ossipov, D. A. Self-Healing Silk Fibroin-Based Hydrogel for Bone Regeneration: Dynamic Metal-Ligand Self-Assembly Approach. *Adv. Funct. Mater.* **2017**, *27*, 1700591.
(194) Yang, X.; Akhtar, S.; Rubino, S.; Leifer, K.; Hilborn, J. n.; Ossipov, D. Direct ″Click ″Synthesis of Hybrid Bisphosphonate−Hyaluronic Acid Hydrogel in Aqueous Solution for Biomineralization. *Chem. Mater.* **2012**, *24*, 1690−1697.
(195) Liu, D.; He, C.; Poon, C.; Lin, W. Theranostic Nanoscale Coordination Polymers for Magnetic Resonance Imaging and Bisphosphonate Delivery. *J. Mater. Chem. B* **2014**, *2*, 8249−8255.
(196) Nejadnik, M. R.; Yang, X.; Bongio, M.; Alghamdi, H. S.; Van den Beucken, J. J.; Huysmans, M. C.; Jansen, J. A.; Hilborn, J.; Ossipov, D.; Leeuwenburgh, S. C. Self-Healing Hybrid Nanocomposites Consisting of Bisphosphonated Hyaluronan and Calcium Phosphate Nanoparticles. *Biomaterials* **2014**, *35*, 6918−6929.
(197) Shi, L.; Han, Y.; Hilborn, J.; Ossipov, D. Smart" Drug Loaded Nanoparticle Delivery from a Self-Healing Hydrogel Enabled by Dynamic Magnesium−BioPolym. Chem. *Chem. Commun.* **2016**, *52*, 11151−11154.
(198) Lopez-Perez, P. M.; da Silva, R. M.; Strehin, I.; Kouwer, P. H.; Leeuwenburgh, S. C.; Messersmith, P. B. Self-Healing Hydrogels Formed by Complexation between Calcium Ions and Bisphosphonate-Functionalized Star-Shaped Polymers. *Macromolecules* **2017**, *50*, 8698−8706.
(199) Shi, L.; Carstensen, H.; Hölzl, K.; Lunzer, M.; Li, H.; Hilborn, J.; Ovsianikov, A.; Ossipov, D. A. Dynamic Coordination Chemistry Enables Free Directional Printing of Biopolymer Hydrogel. *Chem. Mater.* **2017**, *29*, 5816−5823.
(200) Kootala, S.; Ossipov, D.; van den Beucken, J. J.; Leeuwenburgh, S.; Hilborn, J. Bisphosphonate-Functionalized Hyaluronic Acid Showing Selective Affinity for Osteoclasts as a Potential Treatment for Osteoporosis. *Biomater. Sci.* **2015**, *3*, 1197−1207.
(201) Peng, F.; Li, G.; Liu, X.; Wu, S.; Tong, Z. Redox-Responsive Gel− Sol/Sol− Gel Transition in Poly (Acrylic Acid) Aqueous Solution Containing Fe (Iii) Ions Switched by Light. *J. Am. Chem. Soc.* **2008**, *130*, 16166−16167.
(202) Wei, Z.; He, J.; Liang, T.; Oh, H.; Athas, J.; Tong, Z.; Wang, C.; Nie, Z. Autonomous Self-Healing of Poly (Acrylic Acid) Hydrogels Induced by the Migration of Ferric Ions. *Polym. Chem.* **2013**, *4*, 4601−4605.
(203) Zhou, H.; Xu, G.; Li, J.; Zeng, S.; Zhang, X.; Zheng, Z.; Ding, X.; Chen, W.; Wang, Q.; Zhang, W. Preparation and Self-Healing Behaviors of Poly (Acrylic Acid)/Cerium Ions Double Network Hydrogels. *Macromol. Res.* **2015**, *23*, 1098−1102.
(204) Tao, Z.; Peng, K.; Fan, Y.; Liu, Y.; Yang, H. Multi-Stimuli Responsive Supramolecular Hydrogels Based on Fe 3+ and Diblock Copolymer Micelle Complexation. *Polym. Chem.* **2016**, *7*, 1405−1412.
(205) Chen, Y. M.; Sun, L.; Yang, S. A.; Shi, L.; Zheng, W. J.; Wei, Z.; Hu, C. Self-Healing and Photoluminescent Carboxymethyl Cellulose-Based Hydrogels. *Eur. Polym. J.* **2017**, *94*, 501−510.
(206) Shao, C.; Chang, H.; Wang, M.; Xu, F.; Yang, J. High-Strength, Tough, and Self-Healing Nanocomposite Physical Hydrogels Based on the Synergistic Effects of Dynamic Hydrogen Bond and Dual Coordination Bonds. *ACS Appl. Mater. Interfaces* **2017**, *9*, 28305−28318.
(207) Liu, K.; Zang, S.; Xue, R.; Yang, J.; Wang, L.; Huang, J.; Yan, Y. Coordination-Triggered Hierarchical Folate/Zinc Supramolecular

https://dx.doi.org/10.1021/acs.chemrev.0c00015
Chem. Rev. 2020, 120, 10834−10886

Hydrogels Leading to Printable Biomaterials. *ACS Appl. Mater. Interfaces* **2018**, *10*, 4530−4539.
(208) Bonazzi, S.; DeMorais, M. M.; Gottarelli, G.; Mariani, P.; Spada, G. P. Self-Assembly and Liquid Crystal Formation of Folic Acid Salts. *Angew. Chem., Int. Ed. Engl.* **1993**, *32*, 248−250.
(209) Ciuchi, F.; Di Nicola, G.; Franz, H.; Gottarelli, G.; Mariani, P.; Ponzi Bossi, M. G.; Spada, G. P. Self-Recognition and Self-Assembly of Folic Acid Salts: Columnar Liquid Crystalline Polymorphism and the Column Growth Process. *J. Am. Chem. Soc.* **1994**, *116*, 7064−7071.
(210) Kato, T.; Matsuoka, T.; Nishii, M.; Kamikawa, Y.; Kanie, K.; Nishimura, T.; Yashima, E.; Ujiie, S. Supramolecular Chirality of Thermotropic Liquid-Crystalline Folic Acid Derivatives. *Angew. Chem., Int. Ed.* **2004**, *43*, 1969−1972.
(211) Holten-Andersen, N.; Harrington, M. J.; Birkedal, H.; Lee, B. P.; Messersmith, P. B.; Lee, K. Y. C.; Waite, J. H. Ph-Induced Metal-Ligand Cross-Links Inspired by Mussel Yield Self-Healing Polymer Networks with near-Covalent Elastic Moduli. *Proc. Natl. Acad. Sci. U. S. A.* **2011**, *108*, 2651−2655.
(212) Wang, W.; Xu, Y.; Li, A.; Li, T.; Liu, M.; von Klitzing, R.; Ober, C. K.; Kayitmazer, A. B.; Li, L.; Guo, X. Zinc Induced Polyelectrolyte Coacervate Bioadhesive and Its Transition to a Self-Healing Hydrogel. *RSC Adv.* **2015**, *5*, 66871−66878.
(213) Liu, Y.; Meng, H.; Konst, S.; Sarmiento, R.; Rajachar, R.; Lee, B. P. Injectable Dopamine-Modified Poly (Ethylene Glycol) Nanocomposite Hydrogel with Enhanced Adhesive Property and Bioactivity. *ACS Appl. Mater. Interfaces* **2014**, *6*, 16982−16992.
(214) Vatankhah-Varnoosfaderani, M.; Hashmi, S.; GhavamiNejad, A.; Stadler, F. J. Rapid Self-Healing and Triple Stimuli Responsiveness of a Supramolecular Polymer Gel Based on Boron−Catechol Interactions in a Novel Water-Soluble Mussel-Inspired Copolymer. *Polym. Chem.* **2014**, *5*, 512−523.
(215) Rahim, M. A.; Kristufek, S. L.; Pan, S.; Richardson, J. J.; Caruso, F. Phenolic Building Blocks for the Assembly of Functional Materials. *Angew. Chem., Int. Ed.* **2019**, *58*, 1904−1927.
(216) Harrington, M. J.; Masic, A.; Holten-Andersen, N.; Waite, J. H.; Fratzl, P. Iron-Clad Fibers: A Metal-Based Biological Strategy for Hard Flexible Coatings. *Science* **2010**, *328*, 216−220.
(217) Zeng, H.; Hwang, D. S.; Israelachvili, J. N.; Waite, J. H. Strong Reversible Fe3+-Mediated Bridging between Dopa-Containing Protein Films in Water. *Proc. Natl. Acad. Sci. U. S. A.* **2010**, *107*, 12850−12853.
(218) Holten-Andersen, N.; Mates, T. E.; Toprak, M. S.; Stucky, G. D.; Zok, F. W.; Waite, J. H. Metals and the Integrity of a Biological Coating: The Cuticle of Mussel Byssus. *Langmuir* **2009**, *25*, 3323−3326.
(219) Taylor, S. W.; Chase, D. B.; Emptage, M. H.; Nelson, M. J.; Waite, J. H. Ferric Ion Complexes of a Dopa-Containing Adhesive Protein from Mytilus Edulis. *Inorg. Chem.* **1996**, *35*, 7572−7577.
(220) Sever, M. J.; Weisser, J. T.; Monahan, J.; Srinivasan, S.; Wilker, J. J. Metal-Mediated Cross-Linking in the Generation of a Marine-Mussel Adhesive. *Angew. Chem., Int. Ed.* **2004**, *43*, 448−450.
(221) Avdeef, A.; Sofen, S. R.; Bregante, T. L.; Raymond, K. N. Coordination Chemistry of Microbial Iron Transport Compounds. 9. Stability Constants for Catechol Models of Enterobactin. *J. Am. Chem. Soc.* **1978**, *100*, 5362−5370.
(222) Hwang, G. H.; Min, K. H.; Lee, H. J.; Nam, H. Y.; Choi, G. H.; Kim, B. J.; Jeong, S. Y.; Lee, S. C. Ph-Responsive Robust Polymer Micelles with Metal−Ligand Coordinated Core Cross-Links. *Chem. Commun.* **2014**, *50*, 4351−4353.
(223) Menyo, M. S.; Hawker, C. J.; Waite, J. H. Versatile Tuning of Supramolecular Hydrogels through Metal Complexation of Oxidation-Resistant Catechol-Inspired Ligands. *Soft Matter* **2013**, *9*, 10314−10323.
(224) Guo, Z.; Ni, K.; Wei, D.; Ren, Y. Fe 3+-Induced Oxidation and Coordination Cross-Linking in Catechol−Chitosan Hydrogels under Acidic Ph Conditions. *RSC Adv.* **2015**, *5*, 37377−37384.
(225) Hou, S.; Ma, P. X. Stimuli-Responsive Supramolecular Hydrogels with High Extensibility and Fast Self-Healing Via Precoordinated Mussel-Inspired Chemistry. *Chem. Mater.* **2015**, *27*, 7627−7635.
(226) Li, Q.; Barrett, D. G.; Messersmith, P. B.; Holten-Andersen, N. Controlling Hydrogel Mechanics Via Bio-Inspired Polymer−Nanoparticle Bond Dynamics. *ACS Nano* **2016**, *10*, 1317−1324.
(227) Azevedo, S.; Costa, A. M.; Andersen, A.; Choi, I. S.; Birkedal, H.; Mano, J. F. Bioinspired Ultratough Hydrogel with Fast Recovery, Self-Healing, Injectability and Cytocompatibility. *Adv. Mater.* **2017**, *29*, 1700759.
(228) Fan, C.; Fu, J.; Zhu, W.; Wang, D.-A. A Mussel-Inspired Double-Crosslinked Tissue Adhesive Intended for Internal Medical Use. *Acta Biomater.* **2016**, *33*, 51−63.
(229) Quan, W.-Y.; Hu, Z.; Liu, H.-Z.; Ouyang, Q.-Q.; Zhang, D.-Y.; Li, S.-D.; Li, P.-W.; Yang, Z.-M. Mussel-Inspired Catechol-Functionalized Hydrogels and Their Medical Applications. *Molecules* **2019**, *24*, 2586.
(230) Liu, C.; McClements, D. J.; Li, M.; Xiong, L.; Sun, Q. Development of Self-Healing Double-Network Hydrogels: Enhancement of the Strength of Wheat Gluten Hydrogels by in Situ Metal-Catechol Coordination. *J. Agric. Food Chem.* **2019**, *67*, 6508−6516.
(231) Gadkari, P. V.; Balaraman, M. Catechins: Sources, Extraction and Encapsulation: A Review. *Food Bioprod. Process.* **2015**, *93*, 122−138.
(232) Degtyar, E.; Harrington, M. J.; Politi, Y.; Fratzl, P. The Mechanical Role of Metal Ions in Biogenic Protein-Based Materials. *Angew. Chem., Int. Ed.* **2014**, *53*, 12026−12044.
(233) Broomell, C. C.; Mattoni, M. A.; Zok, F. W.; Waite, J. H. Critical Role of Zinc in Hardening of Nereis Jaws. *J. Exp. Biol.* **2006**, *209*, 3219−3225.
(234) Schmitt, C. N.; Politi, Y.; Reinecke, A.; Harrington, M. J. Role of Sacrificial Protein−Metal Bond Exchange in Mussel Byssal Thread Self-Healing. *Biomacromolecules* **2015**, *16*, 2852−2861.
(235) Zechel, S.; Hager, M. D.; Priemel, T.; Harrington, M. J. Healing through Histidine: Bioinspired Pathways to Self-Healing Polymers Via Imidazole−Metal Coordination. *Biomimetics* **2019**, *4*, 20.
(236) Fullenkamp, D. E.; He, L.; Barrett, D. G.; Burghardt, W. R.; Messersmith, P. B. Mussel-Inspired Histidine-Based Transient Network Metal Coordination Hydrogels. *Macromolecules* **2013**, *46*, 1167−1174.
(237) Grindy, S. C.; Learsch, R.; Mozhdehi, D.; Cheng, J.; Barrett, D. G.; Guan, Z.; Messersmith, P. B.; Holten-Andersen, N. Control of Hierarchical Polymer Mechanics with Bioinspired Metal-Coordination Dynamics. *Nat. Mater.* **2015**, *14*, 1210.
(238) Enke, M.; Bode, S.; Vitz, J.; Schacher, F. H.; Harrington, M. J.; Hager, M. D.; Schubert, U. S. Self-Healing Response in Supramolecular Polymers Based on Reversible Zinc−Histidine Interactions. *Polymer* **2015**, *69*, 274−282.
(239) Kou, S.; Yang, X.; Yang, Z.; Liu, X.; Wegner, S. V.; Sun, F. Cobalt-Cross-Linked, Redox-Responsive Spy Network Protein Hydrogels. *ACS Macro Lett.* **2019**, *8*, 773−778.
(240) Wegner, S. V.; Schenk, F. C.; Witzel, S.; Bialas, F.; Spatz, J. P. Cobalt Cross-Linked Redox-Responsive Peg Hydrogels: From Viscoelastic Liquids to Elastic Solids. *Macromolecules* **2016**, *49*, 4229−4235.
(241) Grindy, S. C.; Holten-Andersen, N. Bio-Inspired Metal-Coordinate Hydrogels with Programmable Viscoelastic Material Functions Controlled by Longwave Uv Light. *Soft Matter* **2017**, *13*, 4057−4065.
(242) Enke, M.; Jehle, F.; Bode, S.; Vitz, J.; Harrington, M. J.; Hager, M. D.; Schubert, U. S. Histidine−Zinc Interactions Investigated by Isothermal Titration Calorimetry (Itc) and Their Application in Self-Healing Polymers. *Macromol. Chem. Phys.* **2017**, *218*, 1600458.
(243) Sun, F.; Zhang, W.-B.; Mahdavi, A.; Arnold, F. H.; Tirrell, D. A. Synthesis of Bioactive Protein Hydrogels by Genetically Encoded Spytag-Spycatcher Chemistry. *Proc. Natl. Acad. Sci. U. S. A.* **2014**, *111*, 11269−11274.
(244) Schuurman, W.; Levett, P. A.; Pot, M. W.; van Weeren, P. R.; Dhert, W. J.; Hutmacher, D. W.; Melchels, F. P.; Klein, T. J.; Malda, J. Gelatin-Methacrylamide Hydrogels as Potential Biomaterials for Fabrication of Tissue-Engineered Cartilage Constructs. *Macromol. Biosci.* **2013**, *13*, 551−561.

https://dx.doi.org/10.1021/acs.chemrev.0c00015
Chem. Rev. 2020, 120, 10834−10886

(245) Censi, R.; Schuurman, W.; Malda, J.; Di Dato, G.; Burgisser, P. E.; Dhert, W. J.; Van Nostrum, C. F.; Di Martino, P.; Vermonden, T.; Hennink, W. E. A Printable Photopolymerizable Thermosensitive P (Hpmam-Lactate)-Peg Hydrogel for Tissue Engineering. *Adv. Funct. Mater.* **2011**, *21*, 1833−1842.
(246) Kim, S. H.; Yeon, Y. K.; Lee, J. M.; Chao, J. R.; Lee, Y. J.; Seo, Y. B.; Sultan, M. T.; Lee, O. J.; Lee, J. S.; Yoon, S.-i. Precisely Printable and Biocompatible Silk Fibroin Bioink for Digital Light Processing 3D Printing. *Nat. Commun.* **2018**, *9*, 1620.
(247) Yin, J.; Yan, M.; Wang, Y.; Fu, J.; Suo, H. 3D Bioprinting of Low-Concentration Cell-Laden Gelatin Methacrylate (Gelma) Bioinks with a Two-Step Cross-Linking Strategy. *ACS Appl. Mater. Interfaces* **2018**, *10*, 6849−6857.
(248) Parkatzidis, K.; Chatzinikolaidou, M.; Kaliva, M.; Bakopoulou, A.; Farsari, M.; Vamvakaki, M. Multi-Photon 3D Printing of Biopolymer-Based Hydrogels. *ACS Biomater. Sci. Eng.* **2019**, *5*, 6161−6170.
(249) Jang, T.-S.; Jung, H.-D.; Pan, M. H.; Han, W. T.; Chen, S.; Song, J. 3D Printing of Hydrogel Composite Systems: Recent Advances in Technology for Tissue Engineering. *Int. J. Bioprint.* **2018**, *4*, 126.
(250) Yang, J.-A.; Yeom, J.; Hwang, B. W.; Hoffman, A. S.; Hahn, S. K. Situ-Forming Injectable Hydrogels for Regenerative Medicine. *Prog. Polym. Sci.* **2014**, *39*, 1973−1986.
(251) Picchioni, F.; Muljana, H. Hydrogels Based on Dynamic Covalent and Non Covalent Bonds: A Chemistry Perspective. *Gels* **2018**, *4*, 21.
(252) Liu, Y.; Hsu, S.-h. Synthesis and Biomedical Applications of Self-Healing Hydrogels. *Front. Chem.* **2018**, *6*, 449.
(253) De France, K. J.; Yager, K. G.; Chan, K. J.; Corbett, B.; Cranston, E. D.; Hoare, T. Injectable Anisotropic Nanocomposite Hydrogels Direct in Situ Growth and Alignment of Myotubes. *Nano Lett.* **2017**, *17*, 6487−6495.
(254) Chakma, P.; Konkolewicz, D. Dynamic Covalent Bonds in Polymeric Materials. *Angew. Chem., Int. Ed.* **2019**, *58*, 9682−9695.
(255) Xu, C.; Dai, G.; Hong, Y. Recent Advances in High-Strength and Elastic Hydrogels for 3D Printing in Biomedical Applications. *Acta Biomater.* **2019**, *95*, 50−59.
(256) Piantanida, E.; Alonci, G.; Bertucci, A.; De Cola, L. Design of Nanocomposite Injectable Hydrogels for Minimally Invasive Surgery. *Acc. Chem. Res.* **2019**, *52*, 2101−2112.
(257) Roberts, M. C.; Hanson, M. C.; Massey, A. P.; Karren, E. A.; Kiser, P. F. Dynamically Restructuring Hydrogel Networks Formed with Reversible Covalent Crosslinks. *Adv. Mater.* **2007**, *19*, 2503−2507.
(258) He, L.; Fullenkamp, D. E.; Rivera, J. G.; Messersmith, P. B. Ph Responsive Self-Healing Hydrogels Formed by Boronate−Catechol Complexation. *Chem. Commun.* **2011**, *47*, 7497−7499.
(259) Amamoto, Y.; Kamada, J.; Otsuka, H.; Takahara, A.; Matyjaszewski, K. Repeatable Photoinduced Self-Healing of Covalently Cross-Linked Polymers through Reshuffling of Trithiocarbonate Units. *Angew. Chem., Int. Ed.* **2011**, *50*, 1660−1663.
(260) Belowich, M. E.; Stoddart, J. F. Dynamic Imine Chemistry. *Chem. Soc. Rev.* **2012**, *41*, 2003−2024.
(261) Chao, A.; Negulescu, I.; Zhang, D. Dynamic Covalent Polymer Networks Based on Degenerative Imine Bond Exchange: Tuning the Malleability and Self-Healing Properties by Solvent. *Macromolecules* **2016**, *49*, 6277−6284.
(262) Ma, X.; Xu, T.; Chen, W.; Qin, H.; Chi, B.; Ye, Z. Injectable Hydrogels Based on the Hyaluronic Acid and Poly (Γ-Glutamic Acid) for Controlled Protein Delivery. *Carbohydr. Polym.* **2018**, *179*, 100−109.
(263) Ding, F.; Wu, S.; Wang, S.; Xiong, Y.; Li, Y.; Li, B.; Deng, H.; Du, Y.; Xiao, L.; Shi, X. A Dynamic and Self-Crosslinked Polysaccharide Hydrogel with Autonomous Self-Healing Ability. *Soft Matter* **2015**, *11*, 3971−3976.
(264) Zhang, Y.; Tao, L.; Li, S.; Wei, Y. Synthesis of Multiresponsive and Dynamic Chitosan-Based Hydrogels for Controlled Release of Bioactive Molecules. *Biomacromolecules* **2011**, *12*, 2894−2901.
(265) Xu, Y.; Li, Y.; Chen, Q.; Fu, L.; Tao, L.; Wei, Y. Injectable and Self-Healing Chitosan Hydrogel Based on Imine Bonds: Design and Therapeutic Applications. *Int. J. Mol. Sci.* **2018**, *19*, 2198.
(266) Zhang, Y.; Yang, B.; Zhang, X.; Xu, L.; Tao, L.; Li, S.; Wei, Y. A Magnetic Self-Healing Hydrogel. *Chem. Commun.* **2012**, *48*, 9305−9307.
(267) Li, Y.; Zhang, Y.; Shi, F.; Tao, L.; Wei, Y.; Wang, X. Modulus-Regulated 3D-Cell Proliferation in an Injectable Self-Healing Hydrogel. *Colloids Surf., B* **2017**, *149*, 168−173.
(268) Jia, Y.; Li, J. Molecular Assembly of Schiff Base Interactions: Construction and Application. *Chem. Rev.* **2015**, *115*, 1597−1621.
(269) Lehn, J.-M. From Supramolecular Chemistry Towards Constitutional Dynamic Chemistry and Adaptive Chemistry. *Chem. Soc. Rev.* **2007**, *36*, 151−160.
(270) Rowan, S. J.; Cantrill, S. J.; Cousins, G. R.; Sanders, J. K.; Stoddart, J. F. Dynamic Covalent Chemistry. *Angew. Chem., Int. Ed.* **2002**, *41*, 898−952.
(271) Wang, J.; Wang, D.; Yan, H.; Tao, L.; Wei, Y.; Li, Y.; Wang, X.; Zhao, W.; Zhang, Y.; Zhao, L.; Sun, X. An Injectable Ionic Hydrogel Inducing High Temperature Hyperthermia for Microwave Tumor Ablation. *J. Mater. Chem. B* **2017**, *5*, 4110−4120.
(272) Yang, L.; Li, Y.; Gou, Y.; Wang, X.; Zhao, X.; Tao, L. Improving Tumor Chemotherapy Effect Using an Injectable Self-Healing Hydrogel as Drug Carrier. *Polym. Chem.* **2017**, *8*, 5071−5076.
(273) Xie, W.; Gao, Q.; Guo, Z.; Wang, D.; Gao, F.; Wang, X.; Wei, Y.; Zhao, L. Injectable and Self-Healing Thermosensitive Magnetic Hydrogel for Asynchronous Control Release of Doxorubicin and Docetaxel to Treat Triple-Negative Breast Cancer. *ACS Appl. Mater. Interfaces* **2017**, *9*, 33660−33673.
(274) Qu, J.; Zhao, X.; Ma, P. X.; Guo, B. Ph-Responsive Self-Healing Injectable Hydrogel Based on N-Carboxyethyl Chitosan for Hepatocellular Carcinoma Therapy. *Acta Biomater.* **2017**, *58*, 168−180.
(275) Zhao, X.; Wu, H.; Guo, B.; Dong, R.; Qiu, Y.; Ma, P. X. Antibacterial Anti-Oxidant Electroactive Injectable Hydrogel as Self-Healing Wound Dressing with Hemostasis and Adhesiveness for Cutaneous Wound Healing. *Biomaterials* **2017**, *122*, 34−47.
(276) Xi, W.; Scott, T. F.; Kloxin, C. J.; Bowman, C. N. Click Chemistry in Materials Science. *Adv. Funct. Mater.* **2014**, *24*, 2572−2590.
(277) Roy, N.; Buhler, E.; Lehn, J. M. Double Dynamic Self-Healing Polymers: Supramolecular and Covalent Dynamic Polymers Based on the Bis-Iminocarbohydrazide Motif. *Polym. Int.* **2014**, *63*, 1400−1405.
(278) Deng, G.; Tang, C.; Li, F.; Jiang, H.; Chen, Y. Covalent Cross-Linked Polymer Gels with Reversible Sol− Gel Transition and Self-Healing Properties. *Macromolecules* **2010**, *43*, 1191−1194.
(279) Zhang, D.-D.; Ruan, Y.-B.; Zhang, B.-Q.; Qiao, X.; Deng, G.; Chen, Y.; Liu, C.-Y. A Self-Healing Pdms Elastomer Based on Acylhydrazone Groups and the Role of Hydrogen Bonds. *Polymer* **2017**, *120*, 189−196.
(280) McKinnon, D. D.; Domaille, D. W.; Cha, J. N.; Anseth, K. S. Biophysically Defined and Cytocompatible Covalently Adaptable Networks as Viscoelastic 3D Cell Culture Systems. *Adv. Mater.* **2014**, *26*, 865−872.
(281) Zhang, X.; Waymouth, R. M. 1, 2-Dithiolane-Derived Dynamic, Covalent Materials: Cooperative Self-Assembly and Reversible Cross-Linking. *J. Am. Chem. Soc.* **2017**, *139*, 3822−3833.
(282) Wang, H.; Zhu, D.; Paul, A.; Cai, L.; Enejder, A.; Yang, F.; Heilshorn, S. C. Covalently Adaptable Elastin-Like Protein−Hyaluronic Acid (Elp−Ha) Hybrid Hydrogels with Secondary Thermoresponsive Crosslinking for Injectable Stem Cell Delivery. *Adv. Funct. Mater.* **2017**, *27*, 1605609.
(283) Wang, L. L.; Highley, C. B.; Yeh, Y. C.; Galarraga, J. H.; Uman, S.; Burdick, J. A. Three-Dimensional Extrusion Bioprinting of Single- and Double-Network Hydrogels Containing Dynamic Covalent Crosslinks. *J. Biomed. Mater. Res., Part A* **2018**, *106*, 865−875.
(284) Ouyang, L.; Highley, C. B.; Rodell, C. B.; Sun, W.; Burdick, J. A. 3D Printing of Shear-Thinning Hyaluronic Acid Hydrogels with Secondary Cross-Linking. *ACS Biomater. Sci. Eng.* **2016**, *2*, 1743−1751.

https://dx.doi.org/10.1021/acs.chemrev.0c00015
Chem. Rev. 2020, 120, 10834−10886

(285) Li, Z.; Zhou, F.; Li, Z.; Lin, S.; Chen, L.; Liu, L.; Chen, Y. Hydrogel Cross-Linked with Dynamic Covalent Bonding and Micellization for Promoting Burn Wound Healing. *ACS Appl. Mater. Interfaces* **2018**, *10*, 25194−25202.
(286) Farahani, P. E.; Adelmund, S. M.; Shadish, J. A.; DeForest, C. A. Photomediated Oxime Ligation as a Bioorthogonal Tool for Spatiotemporally-Controlled Hydrogel Formation and Modification. *J. Mater. Chem. B* **2017**, *5*, 4435−4442.
(287) Dilla, R.; Motta, C.; Xu, Y.; Zander, Z.; Bernard, N.; Wiener, C.; Vogt, B.; Becker, M. Mechanically Tunable, Human Mesenchymal Stem Cell Viable Poly (Ethylene Glycol)−Oxime Hydrogels with Invariant Precursor Composition, Concentration, and Stoichiometry. *Mater. Today Chem.* **2019**, *11*, 244−252.
(288) Grover, G. N.; Lam, J.; Nguyen, T. H.; Segura, T.; Maynard, H. D. Biocompatible Hydrogels by Oxime Click Chemistry. *Biomacromolecules* **2012**, *13*, 3013−3017.
(289) Lin, F.; Yu, J.; Tang, W.; Zheng, J.; Defante, A.; Guo, K.; Wesdemiotis, C.; Becker, M. L. Peptide-Functionalized Oxime Hydrogels with Tunable Mechanical Properties and Gelation Behavior. *Biomacromolecules* **2013**, *14*, 3749−3758.
(290) Hafeez, S.; Ooi, H.; Morgan, F.; Mota, C.; Dettin, M.; Van Blitterswijk, C.; Moroni, L.; Baker, M. Viscoelastic Oxidized Alginates with Reversible Imine Type Crosslinks: Self-Healing, Injectable, and Bioprintable Hydrogels. *Gels* **2018**, *4*, 85.
(291) Grover, G. N.; Braden, R. L.; Christman, K. L. Oxime Cross-Linked Injectable Hydrogels for Catheter Delivery. *Adv. Mater.* **2013**, *25*, 2937−2942.
(292) Baker, A. E.; Tam, R. Y.; Shoichet, M. S. Independently Tuning the Biochemical and Mechanical Properties of 3D Hyaluronan-Based Hydrogels with Oxime and Diels−Alder Chemistry to Culture Breast Cancer Spheroids. *Biomacromolecules* **2017**, *18*, 4373−4384.
(293) Wang, S.; Nawale, G. N.; Oommen, O. P.; Hilborn, J.; Varghese, O. P. Influence of Ions to Modulate Hydrazone and Oxime Reaction Kinetics to Obtain Dynamically Cross-Linked Hyaluronic Acid Hydrogels. *Polym. Chem.* **2019**, *10*, 4322−4327.
(294) Nadgorny, M.; Collins, J.; Xiao, Z.; Scales, P. J.; Connal, L. A. 3D-Printing of Dynamic Self-Healing Cryogels with Tuneable Properties. *Polym. Chem.* **2018**, *9*, 1684−1692.
(295) Ghosh, S.; Cabral, J. D.; Hanton, L. R.; Moratti, S. C. Strong Poly (Ethylene Oxide) Based Gel Adhesives Via Oxime Cross-Linking. *Acta Biomater.* **2016**, *29*, 206−214.
(296) Diba, M.; Spaans, S.; Ning, K.; Ippel, B. D.; Yang, F.; Loomans, B.; Dankers, P. Y.; Leeuwenburgh, S. C. Self-Healing Biomaterials: From Molecular Concepts to Clinical Applications. *Adv. Mater. Interfaces* **2018**, *5*, 1800118.
(297) Choh, S.-Y.; Cross, D.; Wang, C. Facile Synthesis and Characterization of Disulfide-Cross-Linked Hyaluronic Acid Hydrogels for Protein Delivery and Cell Encapsulation. *Biomacromolecules* **2011**, *12*, 1126−1136.
(298) Wu, D.-C.; Loh, X. J.; Wu, Y.-L.; Lay, C. L.; Liu, Y. 'Living'controlled in Situ Gelling Systems: Thiol− Disulfide Exchange Method toward Tailor-Made Biodegradable Hydrogels. *J. Am. Chem. Soc.* **2010**, *132*, 15140−15143.
(299) Yu, H.; Wang, Y.; Yang, H.; Peng, K.; Zhang, X. Injectable Self-Healing Hydrogels Formed Via Thiol/Disulfide Exchange of Thiol Functionalized F127 and Dithiolane Modified Peg. *J. Mater. Chem. B* **2017**, *5*, 4121−4127.
(300) Gantar, A.; Drnovšek, N.; Casuso, P.; Pérez-San Vicente, A.; Rodriguez, J.; Dupin, D.; Novak, S.; Loinaz, I. Injectable and Self-Healing Dynamic Hydrogel Containing Bioactive Glass Nanoparticles as a Potential Biomaterial for Bone Regeneration. *RSC Adv.* **2016**, *6*, 69156−69166.
(301) Casuso, P.; Odriozola, I.; Pérez-San Vicente, A. n.; Loinaz, I.; Cabañero, G. n.; Grande, H.-J. r.; Dupin, D. Injectable and Self-Healing Dynamic Hydrogels Based on Metal (I)-Thiolate/Disulfide Exchange as Biomaterials with Tunable Mechanical Properties. *Biomacromolecules* **2015**, *16*, 3552−3561.
(302) Casuso, P.; Pérez-San Vicente, A.; Iribar, H.; Gutiérrez-Rivera, A.; Izeta, A.; Loinaz, I.; Cabañero, G.; Grande, H.-J.; Odriozola, I.; Dupin, D. Aurophilically Cross-Linked "Dynamic" Hydrogels Mimicking Healthy Synovial Fluid Properties. *Chem. Commun.* **2014**, *50*, 15199−15201.
(303) Pérez-San Vicente, A. n.; Peroglio, M.; Ernst, M.; Casuso, P.; Loinaz, I.; Grande, H.-J. r.; Alini, M.; Eglin, D.; Dupin, D. Self-Healing Dynamic Hydrogel as Injectable Shock-Absorbing Artificial Nucleus Pulposus. *Biomacromolecules* **2017**, *18*, 2360−2370.
(304) Peng, H.-H.; Chen, Y.-M.; Lee, C.-I.; Lee, M.-W. Synthesis of a Disulfide Cross-Linked Polygalacturonic Acid Hydrogel for Biomedical Applications. *J. Mater. Sci.: Mater. Med.* **2013**, *24*, 1375−1382.
(305) Chauvin, J. P. R.; Pratt, D. A. On the Reactions of Thiols, Sulfenic Acids, and Sulfinic Acids with Hydrogen Peroxide. *Angew. Chem., Int. Ed.* **2017**, *56*, 6255−6259.
(306) Kirihara, M.; Asai, Y.; Ogawa, S.; Noguchi, T.; Hatano, A.; Hirai, Y. A Mild and Environmentally Benign Oxidation of Thiols to Disulfides. *Synthesis* **2007**, *2007*, 3286−3289.
(307) Bermejo-Velasco, D.; Azémar, A.; Oommen, O. P.; Hilborn, J. n.; Varghese, O. P. Modulating Thiol P K a Promotes Disulfide Formation at Physiological Ph: An Elegant Strategy to Design Disulfide Cross-Linked Hyaluronic Acid Hydrogels. *Biomacromolecules* **2019**, *20*, 1412−1420.
(308) Yesilyurt, V.; Webber, M. J.; Appel, E. A.; Godwin, C.; Langer, R.; Anderson, D. G. Injectable Self-Healing Glucose-Responsive Hydrogels with Ph-Regulated Mechanical Properties. *Adv. Mater.* **2016**, *28*, 86−91.
(309) Deng, C. C.; Brooks, W. L.; Abboud, K. A.; Sumerlin, B. S. Boronic Acid-Based Hydrogels Undergo Self-Healing at Neutral and Acidic Ph. *ACS Macro Lett.* **2015**, *4*, 220−224.
(310) Cash, J. J.; Kubo, T.; Bapat, A. P.; Sumerlin, B. S. Room-Temperature Self-Healing Polymers Based on Dynamic-Covalent Boronic Esters. *Macromolecules* **2015**, *48*, 2098−2106.
(311) Marco-Dufort, B.; Tibbitt, M.W. Design of Moldable Hydrogels for Biomedical Applications Using Dynamic Covalent Boronic Esters. *Mater. Today Chem.* **2019**, *12*, 16−33.
(312) Brooks, W. L.; Sumerlin, B. S. Synthesis and Applications of Boronic Acid-Containing Polymers: From Materials to Medicine. *Chem. Rev.* **2016**, *116*, 1375−1397.
(313) Guan, Y.; Zhang, Y. Boronic Acid-Containing Hydrogels: Synthesis and Their Applications. *Chem. Soc. Rev.* **2013**, *42*, 8106−8121.
(314) Pettignano, A.; Grijalvo, S.; Haering, M.; Eritja, R.; Tanchoux, N.; Quignard, F.; Díaz Díaz, D. Boronic Acid-Modified Alginate Enables Direct Formation of Injectable, Self-Healing and Multistimuli-Responsive Hydrogels. *Chem. Commun.* **2017**, *53*, 3350−3353.
(315) Tang, S.; Ma, H.; Tu, H. C.; Wang, H. R.; Lin, P. C.; Anseth, K. S. Adaptable Fast Relaxing Boronate-Based Hydrogels for Probing Cell−Matrix Interactions. *Adv. Sci.* **2018**, *5*, 1800638.
(316) Guo, R.; Su, Q.; Zhang, J.; Dong, A.; Lin, C.; Zhang, J. Facile Access to Multisensitive and Self-Healing Hydrogels with Reversible and Dynamic Boronic Ester and Disulfide Linkages. *Biomacromolecules* **2017**, *18*, 1356−1364.
(317) Kataoka, K.; Miyazaki, H.; Okano, T.; Sakurai, Y. Sensitive Glucose-Induced Change of the Lower Critical Solution Temperature of Poly [N, N-(Dimethylacrylamide)-Co-3-(Acrylamido)-Phenylboronic Acid] in Physiological Saline. *Macromolecules* **1994**, *27*, 1061−1062.
(318) Liu, H.; Li, Y.; Sun, K.; Fan, J.; Zhang, P.; Meng, J.; Wang, S.; Jiang, L. Dual-Responsive Surfaces Modified with Phenylboronic Acid-Containing Polymer Brush to Reversibly Capture and Release Cancer Cells. *J. Am. Chem. Soc.* **2013**, *135*, 7603−7609.
(319) Hong, S. H.; Kim, S.; Park, J. P.; Shin, M.; Kim, K.; Ryu, J. H.; Lee, H. Dynamic Bonds between Boronic Acid and Alginate: Hydrogels with Stretchable, Self-Healing, Stimuli-Responsive, Remoldable, and Adhesive Properties. *Biomacromolecules* **2018**, *19*, 2053−2061.
(320) Li, Y.; Yang, L.; Zeng, Y.; Wu, Y.; Wei, Y.; Tao, L. Self-Healing Hydrogel with a Double Dynamic Network Comprising Imine and Borate Ester Linkages. *Chem. Mater.* **2019**, *31*, 5576−5583.
(321) Yoshinaga, N.; Ishii, T.; Naito, M.; Endo, T.; Uchida, S.; Cabral, H.; Osada, K.; Kataoka, K. Polyplex Micelles with Phenylboronate/

https://dx.doi.org/10.1021/acs.chemrev.0c00015
Chem. Rev. 2020, 120, 10834−10886

Gluconamide Cross-Linking in the Core Exerting Promoted Gene Transfection through Spatiotemporal Responsivity to Intracellular Ph and Atp Concentration. *J. Am. Chem. Soc.* **2017**, *139*, 18567−18575.
(322) Bérubé, M.; Dowlut, M.; Hall, D. G. Benzoboroxoles as Efficient Glycopyranoside-Binding Agents in Physiological Conditions: Structure and Selectivity of Complex Formation. *J. Org. Chem.* **2008**, *73*, 6471−6479.
(323) Mereddy, G. R.; Chakradhar, A.; Rutkoski, R. M.; Jonnalagadda, S. C. Benzoboroxoles: Synthesis and Applications in Medicinal Chemistry. *J. Organomet. Chem.* **2018**, *865*, 12−22.
(324) Wang, Y.; Li, L.; Kotsuchibashi, Y.; Vshyvenko, S.; Liu, Y.; Hall, D.; Zeng, H.; Narain, R. Self-Healing and Injectable Shear Thinning Hydrogels Based on Dynamic Oxaborole-Diol Covalent Cross-Linking. *ACS Biomater. Sci. Eng.* **2016**, *2*, 2315−2323.
(325) Wu, D.; Wang, W.; Diaz-Dussan, D.; Peng, Y.-Y.; Chen, Y.; Narain, R.; Hall, D. G. Situ Forming and Dual-Crosslink Network Self-Healing Hydrogel Enabled by a Bioorthogonal Nopoldiol-Benzoxaborolate Click Reaction with a Wide Ph Range. *Chem. Mater.* **2019**, *31*, 4092−4102.
(326) Chen, Y.; Diaz-Dussan, D.; Wu, D.; Wang, W.; Peng, Y.-Y.; Asha, A. B.; Hall, D. G.; Ishihara, K.; Narain, R. Bioinspired Self-Healing Hydrogel Based on Benzoxaborole-Catechol Dynamic Covalent Chemistry for 3D Cell Encapsulation. *ACS Macro Lett.* **2018**, *7*, 904−908.
(327) Chen, Y.; Tan, Z.; Wang, W.; Peng, Y. Y.; Narain, R. Injectable, Self-Healing, and Multi-Responsive Hydrogels Via Dynamic Covalent Bond Formation between Benzoxaborole and Hydroxyl Groups. *Biomacromolecules* **2019**, *20*, 1028−1035.
(328) Chen, Y.; Wang, W.; Wu, D.; Nagao, M.; Hall, D. G.; Thundat, T.; Narain, R. Injectable Self-Healing Zwitterionic Hydrogels Based on Dynamic Benzoxaborole−Sugar Interactions with Tunable Mechanical Properties. *Biomacromolecules* **2018**, *19*, 596−605.
(329) Appel, E. A.; Tibbitt, M. W.; Webber, M. J.; Mattix, B. A.; Veiseh, O.; Langer, R. Self-Assembled Hydrogels Utilizing Polymer−Nanoparticle Interactions. *Nat. Commun.* **2015**, *6*, 6295.
(330) Wilson, S. A.; Cross, L. M.; Peak, C. W.; Gaharwar, A. K. Shear-Thinning and Thermo-Reversible Nanoengineered Inks for 3D Bioprinting. *ACS Appl. Mater. Interfaces* **2017**, *9*, 43449−43458.
(331) Du, R.; Wu, J.; Chen, L.; Huang, H.; Zhang, X.; Zhang, J. Hierarchical Hydrogen Bonds Directed Multi-Functional Carbon Nanotube-Based Supramolecular Hydrogels. *Small* **2014**, *10*, 1387−1393.
(332) Gangrade, A.; Mandal, B. B. Injectable Carbon Nanotube Impregnated Silk Based Multifunctional Hydrogel for Localized Targeted and on-Demand Anticancer Drug Delivery. *ACS Biomater. Sci. Eng.* **2019**, *5*, 2365−2381.
(333) Mihajlovic, M.; Mihajlovic, M.; Dankers, P. Y.; Masereeuw, R.; Sijbesma, R. P. Carbon Nanotube Reinforced Supramolecular Hydrogels for Bioapplications. *Macromol. Biosci.* **2019**, *19*, 1800173.
(334) Zhang, Q.; Deng, H.; Li, H.; Song, K.; Zeng, C.; Rong, L. Preparation of Graphene Oxide-Based Supramolecular Hybrid Nanohydrogel through Host-Guest Interaction and Its Application in Drug Delivery. *J. Biomed. Nanotechnol.* **2018**, *14*, 2056−2065.
(335) Huang, W.; Qi, C.; Gao, Y. Injectable Self-Healable Nanocomposite Hydrogels with Mussel-Inspired Adhesive Properties for 3D Printing Ink. *ACS Applied Nano Materials* **2019**, *2*, 5000−5008.
(336) Ohsedo, Y.; Oono, M.; Saruhashi, K.; Watanabe, H.; Miyamoto, N. New Composite Thixotropic Hydrogel Composed of a Polymer Hydrogelator and a Nanosheet. *R. Soc. Open Sci.* **2017**, *4*, 171117.
(337) Nojoomi, A.; Tamjid, E.; Simchi, A.; Bonakdar, S.; Stroeve, P. Injectable Polyethylene Glycol-Laponite Composite Hydrogels as Articular Cartilage Scaffolds with Superior Mechanical and Rheological Properties. *Int. J. Polym. Mater.* **2017**, *66*, 105−114.
(338) Niu, Y.; Guo, T.; Yuan, X.; Zhao, Y.; Ren, L. An Injectable Supramolecular Hydrogel Hybridized with Silver Nanoparticles for Antibacterial Application. *Soft Matter* **2018**, *14*, 1227−1234.
(339) Dai, T.; Wang, C.; Wang, Y.; Xu, W.; Hu, J.; Cheng, Y. A Nanocomposite Hydrogel with Potent and Broad-Spectrum Antibacterial Activity. *ACS Appl. Mater. Interfaces* **2018**, *10*, 15163−15173.
(340) Niu, Y.; Yuan, X.; Zhao, Y.; Zhang, W.; Ren, L. Temperature and Ph Dual-Responsive Supramolecular Polymer Hydrogels Hybridized with Functional Inorganic Nanoparticles. *Macromol. Chem. Phys.* **2017**, *218*, 1600540.
(341) Shao, C.; Meng, L.; Wang, M.; Cui, C.; Wang, B.; Han, C.-R.; Xu, F.; Yang, J. Mimicking Dynamic Adhesiveness and Strain-Stiffening Behavior of Biological Tissues in Tough and Self-Healable Cellulose Nanocomposite Hydrogels. *ACS Appl. Mater. Interfaces* **2019**, *11*, 5885−5895.
(342) Hynninen, V.; Hietala, S.; McKee, J. R.; Murtomaki, L.; Rojas, O. J.; Ikkala, O.; Nonappa. Nonappa. Inverse Thermoreversible Mechanical Stiffening and Birefringence in a Methylcellulose/Cellulose Nanocrystal Hydrogel. *Biomacromolecules* **2018**, *19*, 2795−2804.
(343) Wu, L.; Ohtani, M.; Takata, M.; Saeki, A.; Seki, S.; Ishida, Y.; Aida, T. Magnetically Induced Anisotropic Orientation of Graphene Oxide Locked by in Situ Hydrogelation. *ACS Nano* **2014**, *8*, 4640−4649.
(344) Tan, Z.; Ohara, S.; Naito, M.; Abe, H. Supramolecular Hydrogel of Bile Salts Triggered by Single-Walled Carbon Nanotubes. *Adv. Mater.* **2011**, *23*, 4053−4057.
(345) Bhattacharya, S.; Samanta, S. K. Soft-Nanocomposites of Nanoparticles and Nanocarbons with Supramolecular and Polymer Gels and Their Applications. *Chem. Rev.* **2016**, *116*, 11967−12028.
(346) Mansukhani, N. D.; Guiney, L. M.; Wei, Z.; Roth, E. W.; Putz, K. W.; Luijten, E.; Hersam, M. C. Optothermally Reversible Carbon Nanotube−DNA Supramolecular Hybrid Hydrogels. *Macromol. Rapid Commun.* **2018**, *39*, 1700587.
(347) Lytton-Jean, A. K.; Mirkin, C. A. A Thermodynamic Investigation into the Binding Properties of DNA Functionalized Gold Nanoparticle Probes and Molecular Fluorophore Probes. *J. Am. Chem. Soc.* **2005**, *127*, 12754−12755.
(348) Guilbaud-Chéreau, C.; Dinesh, B.; Schurhammer, R.; Collin, D.; Bianco, A.; Ménard-Moyon, C. Protected Amino Acid−Based Hydrogels Incorporating Carbon Nanomaterials for near-Infrared Irradiation-Triggered Drug Release. *ACS Appl. Mater. Interfaces* **2019**, *11*, 13147−13157.
(349) Lu, G.-H.; Shang, W.-T.; Deng, H.; Han, Z.-Y.; Hu, M.; Liang, X.-Y.; Fang, C.-H.; Zhu, X.-H.; Fan, Y.-F.; Tian, J. Targeting Carbon Nanotubes Based on Igf-1r for Photothermal Therapy of Orthotopic Pancreatic Cancer Guided by Optical Imaging. *Biomaterials* **2019**, *195*, 13−22.
(350) Rehman, H. U.; Chen, Y.; Guo, Y.; Du, Q.; Zhou, J.; Guo, Y.; Duan, H.; Li, H.; Liu, H. Stretchable, Strong and Self-Healing Hydrogel by Oxidized Cnt-Polymer Composite. *Composites, Part A* **2016**, *90*, 250−260.
(351) Liao, M.; Wan, P.; Wen, J.; Gong, M.; Wu, X.; Wang, Y.; Shi, R.; Zhang, L. Wearable, Healable, and Adhesive Epidermal Sensors Assembled from Mussel-Inspired Conductive Hybrid Hydrogel Framework. *Adv. Funct. Mater.* **2017**, *27*, 1703852.
(352) Liu, S.; Bastola, A. K.; Li, L. A 3D Printable and Mechanically Robust Hydrogel Based on Alginate and Graphene Oxide. *ACS Appl. Mater. Interfaces* **2017**, *9*, 41473−41481.
(353) Navaee, A.; Salimi, A. Efficient Amine Functionalization of Graphene Oxide through the Bucherer Reaction: An Extraordinary Metal-Free Electrocatalyst for the Oxygen Reduction Reaction. *RSC Adv.* **2015**, *5*, 59874−59880.
(354) Froidevaux, V.; Negrell, C.; Caillol, S.; Pascault, J.-P.; Boutevin, B. Biobased Amines: From Synthesis to Polymers; Present and Future. *Chem. Rev.* **2016**, *116*, 14181−14224.
(355) Khabibullin, A.; Alizadehgiashi, M.; Khuu, N.; Prince, E.; Tebbe, M.; Kumacheva, E. Injectable Shear-Thinning Fluorescent Hydrogel Formed by Cellulose Nanocrystals and Graphene Quantum Dots. *Langmuir* **2017**, *33*, 12344−12350.
(356) Kalashnikova, I.; Bizot, H.; Cathala, B.; Capron, I. Modulation of Cellulose Nanocrystals Amphiphilic Properties to Stabilize Oil/Water Interface. *Biomacromolecules* **2012**, *13*, 267−275.
(357) Mazeau, K. On the External Morphology of Native Cellulose Microfibrils. *Carbohydr. Polym.* **2011**, *84*, 524−532.

https://dx.doi.org/10.1021/acs.chemrev.0c00015
Chem. Rev. 2020, 120, 10834−10886

(358) Sekiya, R.; Uemura, Y.; Murakami, H.; Haino, T. White-Light-Emitting Edge-Functionalized Graphene Quantum Dots. *Angew. Chem., Int. Ed.* **2014**, *53*, 5619−5623.
(359) Li, Y.; Khuu, N.; Gevorkian, A.; Sarjinsky, S.; Therien-Aubin, H.; Wang, Y.; Cho, S.; Kumacheva, E. Supramolecular Nanofibrillar Thermoreversible Hydrogel for Growth and Release of Cancer Spheroids. *Angew. Chem., Int. Ed.* **2017**, *56*, 6083−6087.
(360) Cheng, J.; Amin, D.; Latona, J.; Heber-Katz, E.; Messersmith, P. B. Supramolecular Polymer Hydrogels for Drug-Induced Tissue Regeneration. *ACS Nano* **2019**, *13*, 5493−5501.
(361) Lee, H. J.; Le, P. T.; Kwon, H. J.; Park, K. D. Supramolecular Assembly of Tetronic−Adamantane and Poly (B-Cyclodextrin) as Injectable Shear-Thinning Hydrogels. *J. Mater. Chem. B* **2019**, *7*, 3374−3382.
(362) Chen, M. H.; Chung, J. J.; Mealy, J. E.; Zaman, S.; Li, E. C.; Arisi, M. F.; Atluri, P.; Burdick, J. A. Injectable Supramolecular Hydrogel/Microgel Composites for Therapeutic Delivery. *Macromol. Biosci.* **2019**, *19*, 1800248.
(363) Park, J.; Brust, T. F.; Lee, H. J.; Lee, S. C.; Watts, V. J.; Yeo, Y. Polydopamine-Based Simple and Versatile Surface Modification of Polymeric Nano Drug Carriers. *ACS Nano* **2014**, *8*, 3347−3356.
(364) Fan, Y.; Zhang, Y.; Zhao, Q.; Xie, Y.; Luo, R.; Yang, P.; Weng, Y. Immobilization of Nano Cu-Mofs with Polydopamine Coating for Adaptable Gasotransmitter Generation and Copper Ion Delivery on Cardiovascular Stents. *Biomaterials* **2019**, *204*, 36−45.
(365) Ho, L. W. C.; Liu, Y.; Han, R.; Bai, Q.; Choi, C. H. J. Nano−Cell Interactions of Non-Cationic Bionanomaterials. *Acc. Chem. Res.* **2019**, *52*, 1519−1530.
(366) Zhang, L.; Su, H.; Wang, H.; Li, Q.; Li, X.; Zhou, C.; Xu, J.; Chai, Y.; Liang, X.; Xiong, L.; Zhang, C. Tumor Chemo-Radiotherapy with Rod-Shaped and Spherical Gold Nano Probes: Shape and Active Targeting Both Matter. *Theranostics* **2019**, *9*, 1893.
(367) Qian, B.; Zheng, Z.; Michailids, M.; Fleck, N.; Bilton, M.; Song, Y.; Li, G.; Shchukin, D. Mussel-Inspired Self-Healing Coatings Based on Polydopamine-Coated Nanocontainers for Corrosion Protection. *ACS Appl. Mater. Interfaces* **2019**, *11*, 10283−10291.
(368) Sy, K. H. S.; Ho, L. W. C.; Lau, W. C. Y.; Ko, H.; Choi, C. H. J. Morphological Diversity, Protein Adsorption, and Cellular Uptake of Polydopamine-Coated Gold Nanoparticles. *Langmuir* **2018**, *34*, 14033−14045.
(369) Ryu, J. H.; Messersmith, P. B.; Lee, H. Polydopamine Surface Chemistry: A Decade of Discovery. *ACS Appl. Mater. Interfaces* **2018**, *10*, 7523−7540.
(370) Lee, H.; Dellatore, S. M.; Miller, W. M.; Messersmith, P. B. Mussel-Inspired Surface Chemistry for Multifunctional Coatings. *Science* **2007**, *318*, 426−430.
(371) Mandal, K.; Jana, N. R. Galactose-Functionalized, Colloidal-Fluorescent Nanoparticle from Aggregation-Induced Emission Active Molecule Via Polydopamine Coating for Cancer Cell Targeting. *ACS Applied Nano Materials* **2018**, *1*, 3531−3540.
(372) Tang, Z.; Jiang, F.; Zhang, Y.; Zhang, Y.; Yuan, Y.; Huang, X.; Wang, Y.; Zhang, D.; Ni, N.; Liu, F.; Luo, M.; Fan, X.; Zhang, W.; Gu, P. Mussel-Inspired Injectable Hydrogel and Its Counterpart for Actuating Proliferation and Neuronal Differentiation of Retinal Progenitor Cells. *Biomaterials* **2019**, *194*, 57−72.
(373) Lyu, Q.; Hsueh, N.; Chai, C. L. The Chemistry of Bioinspired Catechol (Amine)-Based Coatings. *ACS Biomater. Sci. Eng.* **2019**, *5*, 2708−2724.
(374) Hong, S.; Kim, J.; Na, Y. S.; Park, J.; Kim, S.; Singha, K.; Im, G. I.; Han, D. K.; Kim, W. J.; Lee, H. Poly (Norepinephrine): Ultrasmooth Material-Independent Surface Chemistry and Nanodepot for Nitric Oxide. *Angew. Chem., Int. Ed.* **2013**, *52*, 9187−9191.
(375) Kang, S. M.; Rho, J.; Choi, I. S.; Messersmith, P. B.; Lee, H. Norepinephrine: Material-Independent, Multifunctional Surface Modification Reagent. *J. Am. Chem. Soc.* **2009**, *131*, 13224−13225.
(376) Xiao, X.; Zhang, Y.; Wu, J.; Jia, L. Poly (Norepinephrine)-Coated Open Tubular Column for the Separation of Proteins and Recombination Human Erythropoietin by Capillary Electrochromatography. *J. Sep. Sci.* **2017**, *40*, 4636−4644.
(377) Lee, H. A.; Ma, Y.; Zhou, F.; Hong, S.; Lee, H. Material-Independent Surface Chemistry Beyond Polydopamine Coating. *Acc. Chem. Res.* **2019**, *52*, 704−713.
(378) Iwasaki, T.; Tamai, Y.; Yamamoto, M.; Taniguchi, T.; Kishikawa, K.; Kohri, M. Melanin Precursor Influence on Structural Colors from Artificial Melanin Particles: Polydopa, Polydopamine, and Polynorepinephrine. *Langmuir* **2018**, *34*, 11814−11821.
(379) He, Z.; Su, H.; Shen, Y.; Shi, W.; Liu, X.; Liu, Y.; Zhang, F.; Zhang, Y.; Sun, Y.; Ge, D. Poly (Norepinephrine)-Coated Feooh Nanoparticles as Carriers of Artemisinin for Cancer Photothermal-Chemical Combination Therapy. *RSC Adv.* **2019**, *9*, 9968−9982.
(380) Liu, Y.; Zhou, G.; Liu, Z.; Guo, M.; Jiang, X.; Taskin, M. B.; Zhang, Z.; Liu, J.; Tang, J.; Bai, R.; Besenbacher, F.; Chen, M.; Chen, C. Mussel Inspired Polynorepinephrine Functionalized Electrospun Polycaprolactone Microfibers for Muscle Regeneration. *Sci. Rep.* **2017**, *7*, 8197.
(381) Min, K. H.; Min, H. S.; Lee, H. J.; Park, D. J.; Yhee, J. Y.; Kim, K.; Kwon, I. C.; Jeong, S. Y.; Silvestre, O. F.; Chen, X.; Hwang, Y.-S.; Kim, E.-C.; Lee, S. C. Ph-Controlled Gas-Generating Mineralized Nanoparticles: A Theranostic Agent for Ultrasound Imaging and Therapy of Cancers. *ACS Nano* **2015**, *9*, 134−145.
(382) Rim, H. P.; Min, K. H.; Lee, H. J.; Jeong, S. Y.; Lee, S. C. Ph-Tunable Calcium Phosphate Covered Mesoporous Silica Nanocontainers for Intracellular Controlled Release of Guest Drugs. *Angew. Chem., Int. Ed.* **2011**, *50*, 8853−8857.
(383) Ingavle, G. C.; Gionet-Gonzales, M.; Vorwald, C. E.; Bohannon, L. K.; Clark, K.; Galuppo, L. D.; Leach, J. K. Injectable Mineralized Microsphere-Loaded Composite Hydrogels for Bone Repair in a Sheep Bone Defect Model. *Biomaterials* **2019**, *197*, 119−128.
(384) Wang, X.; Deng, Y.; Li, S.; Wang, G.; Qin, E.; Xu, X.; Tang, R.; Qin, C. Biomineralization-Based Virus Shell-Engineering: Towards Neutralization Escape and Tropism Expansion. *Adv. Healthcare Mater.* **2012**, *1*, 443−449.
(385) Xu, B.; Zheng, P.; Gao, F.; Wang, W.; Zhang, H.; Zhang, X.; Feng, X.; Liu, W. A Mineralized High Strength and Tough Hydrogel for Skull Bone Regeneration. *Adv. Funct. Mater.* **2017**, *27*, 1604327.
(386) Rauner, N.; Meuris, M.; Zoric, M.; Tiller, J. C. Enzymatic Mineralization Generates Ultrastiff and Tough Hydrogels with Tunable Mechanics. *Nature* **2017**, *543*, 407.
(387) Lopez-Heredia, M. A.; Łapa, A.; Mendes, A. C.; Balcaen, L.; Samal, S. K.; Chai, F.; Van der Voort, P.; Stevens, C. V.; Parakhonskiy, B. V.; Chronakis, I. S.; et al. Bioinspired, Biomimetic, Double-Enzymatic Mineralization of Hydrogels for Bone Regeneration with Calcium Carbonate. *Mater. Lett.* **2017**, *190*, 13−16.
(388) Wada, N.; Horiuchi, N.; Nakamura, M.; Nozaki, K.; Nagai, A.; Yamashita, K. Controlled Crystallization of Calcium Carbonate Via Cooperation of Polyaspartic Acid and Polylysine under Double-Diffusion Conditions in Agar Hydrogels. *ACS Omega* **2018**, *3*, 16681−16692.
(389) Jeong, S.-H.; Koh, Y.-H.; Kim, S.-W.; Park, J.-U.; Kim, H.-E.; Song, J. Strong and Biostable Hyaluronic Acid−Calcium Phosphate Nanocomposite Hydrogel Via in Situ Precipitation Process. *Biomacromolecules* **2016**, *17*, 841−851.
(390) Simeonov, M.; Apostolov, A.; Vassileva, E. Situ Calcium Phosphate Deposition in Hydrogels of Poly (Acrylic Acid)−Polyacrylamide Interpenetrating Polymer Networks. *RSC Adv.* **2016**, *6*, 16274−16284.
(391) Huang, J.; Liang, Y.; Jia, Z.; Chen, J.; Duan, L.; Liu, W.; Zhu, F.; Liang, Q.; Zhu, W.; You, W.; Xiong, J.; Wang, D. Development of Magnetic Nanocomposite Hydrogel with Potential Cartilage Tissue Engineering. *ACS Omega* **2018**, *3*, 6182−6189.
(392) Ghosh, M.; Halperin-Sternfeld, M.; Grigoriants, I.; Lee, J.; Nam, K. T.; Adler-Abramovich, L. Arginine-Presenting Peptide Hydrogels Decorated with Hydroxyapatite as Biomimetic Scaffolds for Bone Regeneration. *Biomacromolecules* **2017**, *18*, 3541−3550.
(393) Ren, B.; Chen, X.; Du, S.; Ma, Y.; Chen, H.; Yuan, G.; Li, J.; Xiong, D.; Tan, H.; Ling, Z.; Chen, Y.; Hu, X.; Niu, X. Injectable Polysaccharide Hydrogel Embedded with Hydroxyapatite and Calcium

https://dx.doi.org/10.1021/acs.chemrev.0c00015
Chem. Rev. 2020, 120, 10834−10886

Carbonate for Drug Delivery and Bone Tissue Engineering. *Int. J. Biol. Macromol.* **2018**, *118*, 1257−1266.
(394) Sun, S.; Mao, L. B.; Lei, Z.; Yu, S. H.; Cölfen, H. Hydrogels from Amorphous Calcium Carbonate and Polyacrylic Acid: Bio-Inspired Materials for "Mineral Plastics. *Angew. Chem., Int. Ed.* **2016**, *55*, 11765−11769.
(395) Li, A.; Jia, Y.; Sun, S.; Xu, Y.; Minsky, B. B.; Stuart, M. C.; Cölfen, H.; von Klitzing, R.; Guo, X. Mineral-Enhanced Polyacrylic Acid Hydrogel as an Oyster-Inspired Organic−Inorganic Hybrid Adhesive. *ACS Appl. Mater. Interfaces* **2018**, *10*, 10471−10479.
(396) Lee, S. C.; Choi, H. W.; Lee, H. J.; Kim, K. J.; Chang, J. H.; Kim, S. Y.; Choi, J.; Oh, K.-S.; Jeong, Y.-K. In-Situ Synthesis of Reactive Hydroxyapatite Nano-Crystals for a Novel Approach of Surface Grafting Polymerization. *J. Mater. Chem.* **2007**, *17*, 174−180.
(397) Schupp, D. J.; Zhang, X.; Sun, S.; Cölfen, H. Mineral Plastic Hydrogels from the Cross-Linking of Polyacrylic Acid and Alkaline Earth or Transition Metal Ions. *Chem. Commun.* **2019**, *55*, 4913−4916.
(398) Topuz, F.; Bartneck, M.; Pan, Y.; Tacke, F. One-Step Fabrication of Biocompatible Multifaceted Nanocomposite Gels and Nanolayers. *Biomacromolecules* **2017**, *18*, 386−397.
(399) Karpovich, A. L.; Vlasova, M. F.; Sapronova, N. I.; Sukharev, V. S.; Ivanov, V. V. Determination of Dimensions of Exfoliating Materials in Aqueous Suspensions. *MethodsX* **2016**, *3*, 19−24.
(400) Jin, Y.; Shen, Y.; Yin, J.; Qian, J.; Huang, Y. Nanoclay-Based Self-Supporting Responsive Nanocomposite Hydrogels for Printing Applications. *ACS Appl. Mater. Interfaces* **2018**, *10*, 10461−10470.
(401) Negrete-Herrera, N.; Putaux, J.-L.; Bourgeat-Lami, E. Synthesis of Polymer/Laponite Nanocomposite Latex Particles Via Emulsion Polymerization Using Silylated and Cation-Exchanged Laponite Clay Platelets. *Prog. Solid State Chem.* **2006**, *34*, 121−137.
(402) Nelson, A.; Cosgrove, T. A Small-Angle Neutron Scattering Study of Adsorbed Poly (Ethylene Oxide) on Laponite. *Langmuir* **2004**, *20*, 2298−2304.
(403) Huang, X.; Shen, H.; Sun, J.; Lv, K.; Liu, J.; Dong, X.; Luo, S. Nanoscale Laponite as a Potential Shale Inhibitor in Water-Based Drilling Fluid for Stabilization of Wellbore Stability and Mechanism Study. *ACS Appl. Mater. Interfaces* **2018**, *10*, 33252−33259.
(404) Gaharwar, A. K.; Cross, L. M.; Peak, C. W.; Gold, K.; Carrow, J. K.; Brokesh, A.; Singh, K. A. 2d Nanoclay for Biomedical Applications: Regenerative Medicine, Therapeutic Delivery, and Additive Manufacturing. *Adv. Mater.* **2019**, *31*, 1900332.
(405) Zhao, L. Z.; Zhou, C. H.; Wang, J.; Tong, D. S.; Yu, W. H.; Wang, H. Recent Advances in Clay Mineral-Containing Nanocomposite Hydrogels. *Soft Matter* **2015**, *11*, 9229−9246.
(406) Mousa, M.; Evans, N. D.; Oreffo, R. O.; Dawson, J. I. Clay Nanoparticles for Regenerative Medicine and Biomaterial Design: A Review of Clay Bioactivity. *Biomaterials* **2018**, *159*, 204−214.
(407) Afewerki, S.; Magalhães, L. S.; Silva, A. D.; Stocco, T. D.; Silva Filho, E. C.; Marciano, F. R.; Lobo, A. O. Bioprinting Laponite for Orthopedic Applications. *Adv. Healthcare Mater.* **2019**, *8*, 1900158.
(408) Zhai, X.; Ma, Y.; Hou, C.; Gao, F.; Zhang, Y.; Ruan, C.; Pan, H.; Lu, W. W.; Liu, W. 3D-Printed High Strength Bioactive Supramolecular Polymer/Clay Nanocomposite Hydrogel Scaffold for Bone Regeneration. *ACS Biomater. Sci. Eng.* **2017**, *3*, 1109−1118.
(409) Deng, Z.; Hu, T.; Lei, Q.; He, J.; Ma, P. X.; Guo, B. Stimuli-Responsive Conductive Nanocomposite Hydrogels with High Stretchability, Self-Healing, Adhesiveness, and 3D Printability for Human Motion Sensing. *ACS Appl. Mater. Interfaces* **2019**, *11*, 6796−6808.
(410) Yao, C.; Liu, Z.; Yang, C.; Wang, W.; Ju, X. J.; Xie, R.; Chu, L. Y. Poly (N-Isopropylacrylamide)-Clay Nanocomposite Hydrogels with Responsive Bending Property as Temperature-Controlled Manipulators. *Adv. Funct. Mater.* **2015**, *25*, 2980−2991.
(411) El Adraa, K.; Timon, V.; Lambert, J.-F. o.; Al-Rabaa, A.-R.; Jaber, F.; Jaber, M.; Tielens, F. Adsorption of L-Dopa Intercalated in Hydrated Na-Saponite Clay: A Combined Experimental and Theoretical Study. *J. Phys. Chem. C* **2012**, *116*, 26414−26421.
(412) Rezende, R. A.; Bártolo, P. J.; Mendes, A.; Filho, R. M. Rheological Behavior of Alginate Solutions for Biomanufacturing. *J. Appl. Polym. Sci.* **2009**, *113*, 3866−3871.
(413) Chimene, D.; Peak, C. W.; Gentry, J. L.; Carrow, J. K.; Cross, L. M.; Mondragon, E.; Cardoso, G. B.; Kaunas, R.; Gaharwar, A. K. Nanoengineered Ionic−Covalent Entanglement (Nice) Bioinks for 3D Bioprinting. *ACS Appl. Mater. Interfaces* **2018**, *10*, 9957−9968.
(414) Carrow, J. K.; Cross, L. M.; Reese, R. W.; Jaiswal, M. K.; Gregory, C. A.; Kaunas, R.; Singh, I.; Gaharwar, A. K. Widespread Changes in Transcriptome Profile of Human Mesenchymal Stem Cells Induced by Two-Dimensional Nanosilicates. *Proc. Natl. Acad. Sci. U. S. A.* **2018**, *115*, E3905−E3913.
(415) Unterman, S.; Charles, L. F.; Strecker, S. E.; Kramarenko, D.; Pivovarchik, D.; Edelman, E. R.; Artzi, N. Hydrogel Nanocomposites with Independently Tunable Rheology and Mechanics. *ACS Nano* **2017**, *11*, 2598−2610.
(416) Joshi, Y. M.; Reddy, G. R. K.; Kulkarni, A. L.; Kumar, N.; Chhabra, R. P. Rheological Behaviour of Aqueous Suspensions of Laponite: New Insights into the Ageing Phenomena. *Proc. R. Soc. London, Ser. A* **2008**, *464*, 469−489.
(417) Guvendiren, M.; Lu, H. D.; Burdick, J. A. Shear-Thinning Hydrogels for Biomedical Applications. *Soft Matter* **2012**, *8*, 260−272.
(418) Liu, Y.; Meng, H.; Qian, Z.; Fan, N.; Choi, W.; Zhao, F.; Lee, B. P. A Moldable Nanocomposite Hydrogel Composed of a Mussel-Inspired Polymer and a Nanosilicate as a Fit-to-Shape Tissue Sealant. *Angew. Chem., Int. Ed.* **2017**, *56*, 4224−4228.
(419) Liu, Y.; Lee, B. P. Recovery Property of Double-Network Hydrogel Containing a Mussel-Inspired Adhesive Moiety and Nano-Silicate. *J. Mater. Chem. B* **2016**, *4*, 6534−6540.
(420) Skelton, S.; Bostwick, M.; O'Connor, K.; Konst, S.; Casey, S.; Lee, B. P. Biomimetic Adhesive Containing Nanocomposite Hydrogel with Enhanced Materials Properties. *Soft Matter* **2013**, *9*, 3825−3833.
(421) Hong, S. H.; Shin, M.; Lee, J.; Ryu, J. H.; Lee, S.; Yang, J. W.; Kim, W. D.; Lee, H. Staple: Stable Alginate Gel Prepared by Linkage Exchange from Ionic to Covalent Bonds. *Adv. Healthcare Mater.* **2016**, *5*, 75−79.
(422) Fullenkamp, D. E.; Barrett, D. G.; Miller, D. R.; Kurutz, J. W.; Messersmith, P. B. Ph-Dependent Cross-Linking of Catechols through Oxidation Via Fe 3+ and Potential Implications for Mussel Adhesion. *RSC Adv.* **2014**, *4*, 25127−25134.
(423) Peak, C. W.; Stein, J.; Gold, K. A.; Gaharwar, A. K. Nanoengineered Colloidal Inks for 3D Bioprinting. *Langmuir* **2018**, *34*, 917−925.
(424) Ruzicka, B.; Zaccarelli, E.; Zulian, L.; Angelini, R.; Sztucki, M.; Moussaïd, A.; Narayanan, T.; Sciortino, F. Observation of Empty Liquids and Equilibrium Gels in a Colloidal Clay. *Nat. Mater.* **2011**, *10*, 56.
(425) Mourchid, A.; Delville, A.; Lambard, J.; Lecolier, E.; Levitz, P. Phase Diagram of Colloidal Dispersions of Anisotropic Charged Particles: Equilibrium Properties, Structure, and Rheology of Laponite Suspensions. *Langmuir* **1995**, *11*, 1942−1950.
(426) Hsiao, I.-L.; Fritsch-Decker, S.; Leidner, A.; Al-Rawi, M.; Hug, V.; Diabate, S.; Grage, S. L; Meffert, M.; Stoeger, T.; Gerthsen, D.; Ulrich, A. S.; Niemeyer, C. M.; Weiss, C. Biocompatibility of Amine-Functionalized Silica Nanoparticles: The Role of Surface Coverage. *Small* **2019**, *15*, 1805400.
(427) Tian, J.; Tan, Y.; Wang, X.; Gao, L.; Zhang, Z.; Tang, B. Investigation on Mechanical Properties and Reinforced Mechanisms of Hyperbranched Polyesters Functionalized Nano-Silica Modified Epoxy Composites. *Mater. Res. Express* **2019**, *6*, 085347.
(428) Nasiri, S.-S.; Salami-Kalajahi, M.; Roghani-Mamaqani, H.; Dehghani, E. Stimuli-Responsive Behavior of Smart Copolymers-Grafted Magnetic Nanoparticles: Effect of Sequence of Copolymer Blocks. *Inorg. Chim. Acta* **2018**, *476*, 83−92.
(429) Paris, J. L.; Cabañas, M. V.; Manzano, M.; Vallet-Regí, M. Polymer-Grafted Mesoporous Silica Nanoparticles as Ultrasound-Responsive Drug Carriers. *ACS Nano* **2015**, *9*, 11023−11033.
(430) Guo, M.; Jiang, M.; Pispas, S.; Yu, W.; Zhou, C. Supramolecular Hydrogels Made of End-Functionalized Low-Molecular-Weight Peg

https://dx.doi.org/10.1021/acs.chemrev.0c00015
Chem. Rev. 2020, 120, 10834−10886

and A-Cyclodextrin and Their Hybridization with Sio2 Nanoparticles through Host− Guest Interaction. *Macromolecules* **2008**, *41*, 9744−9749.
(431) Lee, M.; Bae, K.; Guillon, P.; Chang, J.; Arlov, Ø.; Zenobi-Wong, M. Exploitation of Cationic Silica Nanoparticles for Bioprinting of Large-Scale Constructs with High Printing Fidelity. *ACS Appl. Mater. Interfaces* **2018**, *10*, 37820−37828.
(432) Serres-Gómez, M.; González-Gaitano, G.; Kaldybekov, D. B.; Mansfield, E. D.; Khutoryanskiy, V. V.; Isasi, J. R. n.; Dreiss, C. c. A. Supramolecular Hybrid Structures and Gels from Host−Guest Interactions between A-Cyclodextrin and Pegylated Organosilica Nanoparticles. *Langmuir* **2018**, *34*, 10591−10602.
(433) Xing, R.; Liu, K.; Jiao, T.; Zhang, N.; Ma, K.; Zhang, R.; Zou, Q.; Ma, G.; Yan, X. An Injectable Self-Assembling Collagen−Gold Hybrid Hydrogel for Combinatorial Antitumor Photothermal/Photodynamic Therapy. *Adv. Mater.* **2016**, *28*, 3669−3676.
(434) Wu, Y.; Wang, H.; Gao, F.; Xu, Z.; Dai, F.; Liu, W. An Injectable Supramolecular Polymer Nanocomposite Hydrogel for Prevention of Breast Cancer Recurrence with Theranostic and Mammoplastic Functions. *Adv. Funct. Mater.* **2018**, *28*, 1801000.
(435) Li, S.; Dong, S.; Xu, W.; Tu, S.; Yan, L.; Zhao, C.; Ding, J.; Chen, X. Antibacterial Hydrogels. *Adv. Sci.* **2018**, *5*, 1700527.
(436) Wahid, F.; Zhong, C.; Wang, H.-S.; Hu, X.-H.; Chu, L.-Q. Recent Advances in Antimicrobial Hydrogels Containing Metal Ions and Metals/Metal Oxide Nanoparticles. *Polymers* **2017**, *9*, 636.
(437) Jing, B.; Chen, X.; Wang, X.; Zhao, Y.; Qiu, H. Sol-Gel-Sol Transition of Gold Nanoparticle-Based Supramolecular Hydrogels Induced by Cyclodextrin Inclusion. *ChemPhysChem* **2008**, *9*, 249−252.
(438) Yu, J.; Ha, W.; Sun, J.-n.; Shi, Y.-p. Supramolecular Hybrid Hydrogel Based on Host−Guest Interaction and Its Application in Drug Delivery. *ACS Appl. Mater. Interfaces* **2014**, *6*, 19544−19551.
(439) Shen, J.-S.; Chen, Y.-L.; Huang, J.-L.; Chen, J.-D.; Zhao, C.; Zheng, Y.-Q.; Yu, T.; Yang, Y.; Zhang, H.-W. Supramolecular Hydrogels for Creating Gold and Silver Nanoparticles in Situ. *Soft Matter* **2013**, *9*, 2017−2023.
(440) Qin, H.; Zhang, T.; Li, H.-N.; Cong, H.-P.; Antonietti, M.; Yu, S.-H. Dynamic Au-Thiolate Interaction Induced Rapid Self-Healing Nanocomposite Hydrogels with Remarkable Mechanical Behaviors. *Chem.* **2017**, *3*, 691−705.
(441) Daniel, M.-C.; Astruc, D. Gold Nanoparticles: Assembly, Supramolecular Chemistry, Quantum-Size-Related Properties, and Applications toward Biology, Catalysis, and Nanotechnology. *Chem. Rev.* **2004**, *104*, 293−346.
(442) Hu, Y.; Liu, X.; Cai, Z.; Zhang, H.; Gao, H.; He, W.; Wu, P.; Cai, C.; Zhu, J.-J.; Yan, Z. Enhancing the Plasmon Resonance Absorption of Multibranched Gold Nanoparticles in the near-Infrared Region for Photothermal Cancer Therapy: Theoretical Predictions and Experimental Verification. *Chem. Mater.* **2019**, *31*, 471−482.
(443) Wang, J.; Zhang, Y.; Jin, N.; Mao, C.; Yang, M. Protein-Induced Gold Nanoparticle Assembly for Improving the Photothermal Effect in Cancer Therapy. *ACS Appl. Mater. Interfaces* **2019**, *11*, 11136−11143.
(444) Jain, P. K.; Huang, X.; El-Sayed, I. H.; El-Sayed, M. A. Noble Metals on the Nanoscale: Optical and Photothermal Properties and Some Applications in Imaging, Sensing, Biology, and Medicine. *Acc. Chem. Res.* **2008**, *41*, 1578−1586.
(445) Motesharei, K.; Myles, D. C. Molecular Recognition on Functionalized Self-Assembled Monolayers of Alkanethiols on Gold. *J. Am. Chem. Soc.* **1998**, *120*, 7328−7336.
(446) Xue, Y.; Li, X.; Li, H.; Zhang, W. Quantifying Thiol−Gold Interactions Towards the Efficient Strength Control. *Nat. Commun.* **2014**, *5*, 4348.
(447) Vericat, C.; Vela, M.; Benitez, G.; Carro, P.; Salvarezza, R. Self-Assembled Monolayers of Thiols and Dithiols on Gold: New Challenges for a Well-Known System. *Chem. Soc. Rev.* **2010**, *39*, 1805−1834.
(448) Liu, K. L.; Zhang, Z.; Li, J. Supramolecular Hydrogels Based on Cyclodextrin−Polymer Polypseudorotaxanes: Materials Design and Hydrogel Properties. *Soft Matter* **2011**, *7*, 11290−11297.
(449) Martín, R.; Rekondo, A.; Echeberria, J.; Cabañero, G.; Grande, H. J.; Odriozola, I. Room Temperature Self-Healing Power of Silicone Elastomers Having Silver Nanoparticles as Crosslinkers. *Chem. Commun.* **2012**, *48*, 8255−8257.
(450) Jiang, D.; Wang, G.; Zheng, F.; Han, J.; Wu, X. Novel Thermo-Sensitive Hydrogels Containing Polythioether Dendrons: Facile Tuning of Lcsts, Strong Absorption of Ag Ions, and Embedment of Smaller Ag Nanocrystals. *Polym. Chem.* **2015**, *6*, 625−632.
(451) Tian, Z.; Chen, C.; Allcock, H. R. Injectable and Biodegradable Supramolecular Hydrogels by Inclusion Complexation between Poly (Organophosphazenes) and A-Cyclodextrin. *Macromolecules* **2013**, *46*, 2715−2724.
(452) Ren, L.; He, L.; Sun, T.; Dong, X.; Chen, Y.; Huang, J.; Wang, C. Dual-Responsive Supramolecular Hydrogels from Water-Soluble Peg-Grafted Copolymers and Cyclodextrin. *Macromol. Biosci.* **2009**, *9*, 902−910.
(453) Zhang, G.; Chen, Y.; Deng, Y.; Ngai, T.; Wang, C. Dynamic Supramolecular Hydrogels: Regulating Hydrogel Properties through Self-Complementary Quadruple Hydrogen Bonds and Thermo-Switch. *ACS Macro Lett.* **2017**, *6*, 641−646.

https://dx.doi.org/10.1021/acs.chemrev.0c00015
Chem. Rev. 2020, 120, 10834−10886